



Full-field characterisation of epicardial deformation using three dimensional digital image correlation (3D-DIC)

by

Paolo Ferraiuoli

Department of Infection, Immunity & Cardiovascular Disease

Faculty of Medicine, Dentistry & Health

The University of Sheffield

Sheffield, UK

in partial fulfilment of the requirements

for the degree of

Doctor of Philosophy

October 2019

Abstract

Imaging of the heart provides valuable insight into its functionality and the progression of diseases affecting the cardiac muscle. Currently, ultrasound 2D speckle tracking echocardiography (US-2D-STE) is the most frequently used clinical technique to detect and monitor the progression of cardiovascular disease through changes in strain of the cardiac muscle. However, this imaging modality has several limitations, which reduce the accuracy and reproducibility of the measurement. As a result, the complex behaviour of heart deformation including contraction and twisting cannot be accurately detected by this technique.

This thesis describes the development of an optical method based on 3D digital image correlation (3D-DIC) to enable full-field deformation analysis in the heart. The hypothesis of this project is that 3D measurement of local strain in experimental *in vitro* and *ex vivo* models of the heart will provide a detailed characterisation of the behaviour of the heart and provide reference measurements for comparison with clinical imaging modalities.

The experimental method requires a robust stereo optical system ensuring high-quality and synchronised imaging during heart deformation. The developed methodology was validated through multiple experimental and numerical tests in a zero-strain configuration, which provided an estimate of the error in the reconstruction of strain on the cardiac surface ($\approx 1\%$).

Applications in experimental *in vitro* and *ex vivo* models of the heart are described. Moreover, a comparison of the performance of 3D-DIC and US-2D-STE under the same conditions of the heart is investigated, demonstrating the superiority of 3D-DIC for dynamic, high-resolution strain measurements (≈ 1.5 mm).

However, being an optical technique, 3D-DIC is limited to only surface measurements on the epicardium and requires an effective speckle pattern to be applied on

the heart surface, which may pose biocompatible problems and important challenges in its application *in vivo*.

This experimental work has led to the development of a robust tool for localised and detailed measurement of strain at a high temporal and spatial resolution, with the latter one order of magnitude improved with respect to existing optical techniques.

Interpretation of the full-field results can be used to show the non-uniform and inhomogeneous strain distribution on the epicardial surface and identify changes in strain within *ex vivo* models of cardiac disease.

Acknowledgements

Firstly, I would like to express my sincere gratitude to my supervisor Dr. Andrew Narracott for the continuous support and expertise, for his confidence in me, patience and encouragement. His guidance and valuable advice have empowered me to overcome the professional problems I have encountered during this period. I feel I haven't had a mere supervisor but a truthful mentor. I'm very grateful.

I would like to thank my second supervisor Dr. John Fenner for his insightful comments and example of being a very committed researcher. Thanks for the patience and presence.

I thank all my colleagues and friends on the O floor at RHH for the chats and beers we had together. I'll be missing all of you very much.

Finally, I would like to thank my Family and Anna Maria for the relentless support throughout all these years.

Contents

| | |
|---|-----------|
| Abstract | i |
| List of Figures | vi |
| List of Tables | xv |
| Introduction | 1 |
| 1 Cardiovascular system and strain imaging techniques | 9 |
| 1.1 Introduction | 9 |
| 1.2 Cardiovascular system | 10 |
| 1.2.1 Structure of the heart | 10 |
| 1.2.2 Perfusion of the heart | 12 |
| 1.2.3 Cardiac pumping mechanism | 13 |
| 1.3 Cardiovascular diseases | 15 |
| 1.3.1 Overview of medical imaging techniques for cardiac strain . . . | 17 |
| 1.3.1.1 Strain definition | 17 |
| 1.3.1.2 Echocardiography methods | 20 |
| 1.3.1.3 Challenges and limitations of US-2D-STE | 22 |
| 1.4 Optical techniques for strain measurements | 24 |
| 1.4.1 Digital Image Correlation | 24 |

| | | |
|----------|---|-----------|
| 1.4.1.1 | Basic operating principle | 26 |
| 1.4.1.2 | Applications of DIC in cardiovascular tissues | 31 |
| 1.5 | Summary | 34 |
| 2 | Design of a 3D-DIC system for cardiac strain assessment | 35 |
| 2.1 | Introduction | 35 |
| 2.2 | Stereo cameras calibration | 37 |
| 2.3 | Stereo imaging system | 39 |
| 2.3.1 | Cameras specification and synchronisation | 39 |
| 2.3.2 | Characterisation of the optical parameters | 40 |
| 2.4 | 3D-DIC methodology | 42 |
| 2.4.1 | Image matching and 3D reconstruction | 42 |
| 2.4.2 | Strain calculation | 46 |
| 2.5 | Validation of the developed 3D-DIC methodology | 49 |
| 2.5.1 | Speckle pattern application | 50 |
| 2.5.1.1 | Materials and methods | 50 |
| 2.5.1.2 | Results | 52 |
| 2.5.1.3 | Discussion | 53 |
| 2.5.2 | Optimisation of DIC parameters using experimental and numerical tests | 53 |
| 2.5.2.1 | Materials and methods | 55 |
| 2.5.2.2 | Results | 56 |
| 2.5.2.3 | Discussion | 58 |
| 2.6 | Summary | 60 |
| 3 | Application of 3D-DIC to <i>in vitro</i> assessment of passive cardiac deformation | 61 |
| 3.1 | Introduction | 62 |
| 3.2 | Materials and methods | 62 |

| | | |
|----------|---|-----------|
| 3.2.1 | Heart harvesting and mounting within the biosimulator platform | 62 |
| 3.2.2 | Speckle pattern application and stereo-imaging | 63 |
| 3.2.3 | Digital image correlation and full-field strain calculation . . . | 66 |
| 3.2.4 | Evaluation of strain variation in the unloaded configuration . . | 66 |
| 3.2.5 | 3D-DIC repeatability and strain variation assessment | 68 |
| 3.3 | Results | 68 |
| 3.4 | Discussion | 73 |
| 3.5 | Summary | 76 |
| 4 | Measurement of <i>in vitro</i> cardiac deformation using both 3D-DIC and US-2D-STE | 77 |
| 4.1 | Introduction | 78 |
| 4.2 | Materials and methods | 78 |
| 4.2.1 | Platform preparation | 78 |
| 4.2.2 | 3D-DIC analysis | 80 |
| 4.2.3 | US-2D-STE analysis | 81 |
| 4.2.4 | Data analysis and comparison between the two techniques . . | 82 |
| 4.3 | Results | 83 |
| 4.4 | Discussion | 89 |
| 4.5 | Summary | 92 |
| 5 | Application of 3D-DIC in an <i>ex vivo</i> experiment | 93 |
| 5.1 | Introduction | 94 |
| 5.2 | Materials and methods | 97 |
| 5.2.1 | <i>Ex vivo</i> heart preparation | 97 |
| 5.2.2 | 3D-DIC measurement | 98 |
| 5.3 | Results | 100 |
| 5.4 | Discussion | 106 |
| 5.5 | Summary | 108 |

| | | |
|----------|------------------------|------------|
| 6 | Conclusions | 110 |
| 6.1 | Key findings | 111 |
| 6.2 | Limitations | 112 |
| 6.3 | Future work | 114 |
| | References | 115 |

List of Figures

| | | |
|-----|--|----|
| 1.1 | Sectional anatomy of the heart and pathway of blood flow. Image adapted from Blausen Medical Communications, Inc., distributed under the terms of the Creative Common CC BY 3.0 licence. | 11 |
| 1.2 | Wall layers of the heart. Image adapted from OpenStax College, distributed under the terms of the Creative Common CC BY 3.0 licence. | 12 |
| 1.3 | The Wiggers diagram showing the different phases and events within the cardiac cycle. The diagram reports time on the x-axis, while blood pressures (i.e. aortic, ventricular and atrial pressures), ventricular volume, electrocardiogram and heart sounds on the y-axis. Adapted from DanielChangMD revised original work of DestinyQx; Redrawn as SVG by xavax, distributed under the terms of the Creative Common CC BY 2.5 licence. | 14 |
| 1.4 | Strain in a 1D object occurs only as lengthening $\varepsilon > 0$ or shortening ($\varepsilon < 0$) of the material. | 17 |
| 1.5 | Relationship between Eulerian and Lagrangian strain obtained using the following equation $Lagrangian\ strain = e^{Eulerian\ strain} - 1$ | 18 |

1.6 Strain in a 2D object can be characterised by four components: two normal strain components ε_x and ε_y , **(a)** and **(b)**, respectively; and two shear strain components ε_{xy} and ε_{yx} , **(c)** and **(d)**, respectively. Shear strain components are associated with the angles θ_x and θ_y 19

1.7 B-mode ultrasound image of the heart along the longitudinal-axis (LAX) **(a)** and short-axis (SAX) **(b)**. 21

1.8 Sectional anatomy of the heart along the longitudinal-axis view (LAX) **(a)** and short-axis view (SAX) **(b)**. Image adapted from Patrick J. Lynch, medical illustrator, distributed under the terms of the Creative Common CC BY 2.5 licence. 22

1.9 Schematic representation of the 2D-DIC **(a)** and 3D-DIC **(b)** experimental setup. 25

1.10 Schematic representation of a reference subset centred at (x_0, y_0) before deformation (reference image) and the corresponding deformed subset centred at (x'_0, y'_0) after deformation (deformed image). Size and spacing of the subset are defined by the *subset size* and *step size*, respectively. u and v are the components of the displacement vector mapping the position of the reference subset in the reference image to the position of the deformed subset in the deformed image. 27

1.11 Image of the speckle pattern applied on the human heart and used for 3D-DIC analysis. This figure has been taken from Soltani et al. (2018), an open access article distributed under the terms of the Creative Common CC BY 4.0 licence. 34

| | | |
|-----|---|----|
| 2.1 | <p>Example of an image pair from Camera 1 (a) and Camera 2 (b) showing the chequerboard (2 mm square size) used for the stereo cameras calibration. The green circles represent the position of the corner points extracted initially by the algorithm, while the red crosses represent these points after the projective transformation. (c) 3D visualisation of the location of the calibration pattern in the cameras' coordinate system. (d) Representation of the typical reprojection errors, a qualitative measure of calibration accuracy, obtained in this study.</p> | 38 |
| 2.2 | <p>Image of the stereo cameras system used in this study.</p> | 40 |
| 2.3 | <p>Influence of camera magnification M on the resulting FOV (a) and DOF (b). Influence of the object to lens distance u on the lens to sensor distance v (c) and DOF (d). These plots are only valid for the optical parameters and type of cameras used in this study.</p> | 41 |
| 2.4 | <p>Diagram describing the steps implemented in this study to carry out 3D-DIC. First, images of the object with the speckle pattern applied from left and right cameras prior the deformation (reference state) are matched using N_{corr} (a). Then, DIC analysis is carried out, separately for the left and right images ((b) and (c)), between the reference and deformed states of the object. At each configuration, the 3D reconstruction of the object surface is achieved using camera calibration data and triangulation of the corresponding points. Finally, strain is obtained by computing the deformations of the elements on the surface meshes respect to their configuration in the reference state, as further discussed in Section 2.4.2.</p> | 44 |
| 2.5 | <p>An example of a triangular element defined on the mesh of object surface prior (left) and after (right) the deformation.</p> | 47 |

| | | |
|------|--|----|
| 2.6 | Image of the porcine heart surface with the applied speckle pattern and representation of the ROI (red square) selected for the DIC analysis before and after binarisation, performed for morphological analysis of the speckles. | 51 |
| 2.7 | (a) Histogram of the grey level intensity of the pixels within the ROI. (b) Cumulative percentage of the speckles with a radius belonging to a specific interval. | 52 |
| 2.8 | Schematic representation of the procedure used to create two virtual stereo images by deforming the image of Fig. 2.6 onto the surface of a cylinder and prescribing geometrical transformation for the two views. Virtual deformed stereo images were, then, generated by increasing the radius of the cylinder. | 56 |
| 2.9 | Strain errors found following the experimental rigid body motion tests. Influence of the subset size (a) and camera shutter speed value (b) on the accuracy (average of surface strains) and precision (standard deviation of surface strains) of the method. | 57 |
| 2.10 | Strain error map on the surface specimen in a zero-strain configuration following the experimental RBM test. This map has been obtained with a DIC subset and step size of 33 and 9 pixels, respectively. This resulted in a spatial resolution of approximately 1.5 mm. | 57 |
| 2.11 | Results from the numerical test showing the strain errors obtained after applying a numerical deformation to the virtual stereo images. The errors were computed by subtracting the average of the surface strains measured to the theoretically imposed (i.e. 10.5%). In these tests, the Green-Lagrange strains E (Eq. (2.6)) have been reported. The effect of the subset size (a) and stereo angle (b) on the resulting strains is reported along with the errorbars indicating the standard deviation of the surface strains. | 58 |

3.1 Schematic diagram of the dynamic cardiac biosimulator. (1) Pulse duplicator replicating physiologic flow and ventricular pressure attached to the left ventricle chamber. (2) Porcine heart (3) Aortic cannula connected to the ascending aorta. (4) Afterload module. (5) Service reservoir. (6) Preload module. (7) Adjustable Starling resistor to ensure that atrial pressures are maintained at physiologic levels. Adapted with permission from (Leopaldi et al., 2018). 64

3.2 (a) Picture of the experimental setup showing the heart with applied speckle pattern within the Cardiac BioSimulator platform and position of the stereo cameras. (b) Close-up of the lateral region of the heart including the left ventricle and atrium overlaid with the region of interest (ROI) used in the 3D-DIC analysis. 65

3.3 . The corresponding points in the left (red dots) and right (green dots) images of the reference state of the heart were matched (a). Afterwards, the displacement of the corresponding points in the images of the deformed states of the heart for the left (b) and right (c) images, respectively, was computed. 67

3.4 Average of the maximum (E_1) and minimum (E_2) principal strain distributions over the reconstructed cardiac surface over multiple cardiac cycles in each heart. The asterisks denote the time point at which strain colour map is reported in Fig. 3.5. 69

3.5 The five hearts with the approximate location of the ROIs (red rectangle) identified on the left ventricles for the 3D-DIC measurements (**upper pane**). Strain colour map and directions of maximum (E_1 , **middle pane**) and minimum (E_2 , **lower pane**) principal strain on the reconstructed ROIs at the largest ventricular volume state indicated by the asterisk in Fig. 3.4. The reconstructed surfaces are seen in the xy-plane. 70

3.6 Haemodynamic variations recorded for the aortic pressure (**upper pane**) and cardiac output (**bottom pane**) between the Reduced and Normal conditions. 72

3.7 Comparison between the maximum principal strain (E_1) distributions under two different haemodynamic scenarios imposed on the same heart (Heart V). Mean aortic pressure for Normal and Reduced were 79 and 57 mmHg, respectively. Mean strain value is shown as a solid line, error bars show the standard deviation over the ROI on the cardiac surface at each time point. 72

4.1 Schematic representation of the experimental setup. The figure shows roughly the position and orientation of the US probe coordinate system, for the LAX (**a**) and SAX views (**b**), along with the stereo cameras coordinate system with respect to the heart. Examples of the corresponding B-mode and optical images acquired by the two methods are shown on the left and right, respectively. The US beam and the ROI selected for the 3D-DIC analysis are overlaid on the heart surface to show the approximate region of overlap between the two techniques. 79

4.2 Representation of the dynamic displacement of Heart I (red lines), Heart II (green lines), Heart III (black lines) and Heart IV (blue lines) in 3D along four cardiac cycles measured by 3D-DIC. The solid and dashed lines were obtained as the average of the displacement components (x, y and z) at each state of the heart deformations for the NT and HT condition, respectively. 84

4.3 Recorded pressures data in the LV (blue line), aorta (red line) and left atrium (green line) for the NT (**a**) and HT (**b**) conditions. 84

4.4 (a) B-mode image of the LAX and SAX views of each heart with points overlaid from which displacement and strain were extracted for comparison with 3D-DIC measurements. (b) Optical images of the LV surface of each individual heart with overlaid a schematic representation of the ROI selected in the 3D-DIC analysis. (c) Magnitude and direction of E_1 and E_2 at peak strain reconstructed with 3D-DIC over the ROI identified in (b). 85

4.5 (a) Average and standard deviation of the displacement distribution extracted from 3D-DIC along the y-axis (OM_y in Fig. 4.1) and US-2D-STE LAX and SAX views along the z-axis (US_z in Fig. 4.1) in each heart and their median values over a single cardiac cycle. (b) Average and standard deviation for the maximum (E_1) and minimum (E_2) principal strains derived from 3D-DIC and the longitudinal and circumferential strains derived from US-2D-STE in each heart and their median values over a single cardiac cycle. (c) Average and standard deviation for the longitudinal (E_x) and transverse (E_y) strains derived from 3D-DIC and the longitudinal and circumferential strains derived from US-2D-STE in each heart and their median values over a single cardiac cycle. 86

4.6 Linear regression between the displacement obtained from 3D-DIC and US-2D-STE, for the LAX and SAX views, for each heart (a) and their median values (b) along one cardiac cycle. Upper- and lower-bands represent the 95% confidence interval. 88

5.1 Picture of the experimental setup including the *ex vivo* model of the heart in a modified Langendorff preparation and positioning of the stereo cameras used for 3D-DIC measurement. 98

5.2 (a) Example of an experimental image in which the wet surface of the heart caused the degradation of the speckle pattern quality. (b) Image of the heart captured in the reference state (end diastole) with overlaid the rectangular ROI investigated in the 3D-DIC analysis. . . . 99

5.3 Representation of the displacement vector field extracted from frames captured during diastole (a) and systole (b). For visual clarity, vectors have been plots every other 18 pixels (two times the step size). . . 101

5.4 Recorded data in the heart and 3D-DIC measurements over the same cardiac cycles. (a) Coronary flow (green line), LV pressure (blue line) and perfusion pressure (red line) behaviour. (b) Plot of the average of each displacement components within the reconstructed ROI along the cardiac cycles. Referring to Fig. 5.2b, negative values of the displacement along x and y direction denoted a motion of the heart leftwards and upwards, while negative values of the displacement along z a motion of the heart towards the stereo cameras. (c) Combined representation of the average maximum (E_1 , black line) and minimum (E_2 , orange line) principal strains obtained in the reconstructed ROI on the LV surface along the cardiac cycles. In this plot, three consecutive cardiac cycles have been identified for a further analysis of displacement and strain using 3D-DIC since during these time points LV pressure values were within the human physiological range. 102

5.5 Representation of the dynamic displacement of the Langendorff-perfused heart in 3D along the three consecutive cardiac cycles measured by 3D-DIC. The lines were obtained as the average of the displacement components (x, y and z) at each state of the heart deformations. 103

- 5.6 Combined representation of the average maximum principal strain distribution (purple line) within the reconstructed ROI on the LV surface obtained from 3D-DIC with the perfusion pressure (red line) and LV pressure (blue line) for the three cardiac cycles investigated (**upper pane**). The start of the cardiac cycle corresponds to end-diastole in which strain is close to zero, while when the coronary flow (**bottom pane**) is maximum, strain magnitude reaches its peak value. 104
- 5.7 Full-field surface map of the maximum (**b-d**) and minimum (**e-f**) principal strain from the reconstructed ROI (red box) on the LV depicted in (**a**) at peak strain for the three cardiac cycles. Maximum (black segments) and minimum (red segments) principal directions are also shown on the map. Width and height of the ROI ranged approximately between 46-50 and 42-46 mm, respectively. 105

List of Tables

| | | |
|-----|--|----|
| 2.1 | Camera specifications. | 40 |
| 2.2 | Algorithms and functions implemented in Ncorr. | 44 |
| 3.1 | Camera parameters and settings used in the DIC analysis | 65 |
| 3.2 | Summary of the systematic (average) and random (standard deviation) zero-strain error over the reconstructed ROIs for the maximum (E_1) and minimum (E_2) principal strain. For each heart, the average and standard deviation of the strain values obtained between three un-deformed images of the heart were calculated. The median and range of the strain values over all five hearts are reported. | 69 |
| 3.3 | Measured haemodynamic and epicardial principal strain values (E_1 and E_2) strain at the end of the highest ventricular volume. For each measurement, the mean and standard deviation for five different heart cycles are given. | 71 |
| 4.1 | Camera parameters and DIC settings. | 81 |
| 4.2 | Peak strain values along a cardiac cycle in each heart measured by 3D-DIC (Maximum and Minimum principal strain) and US-2D-STE (Longitudinal and Circumferential strain) for the NT and HT conditions. | 89 |

| | | |
|-----|---|----|
| 5.1 | Review of relevant works using optical methods to quantify epicardial strains in animal heart preparations. | 96 |
|-----|---|----|

Introduction

Motivation

The heart is the key component in the cardiovascular system pumping blood in the circulatory systems. The effective contractions of the heart ensure the right amount of blood is delivered to all the organs and tissues in the body. However, when specific cardiovascular pathologies occur (e.g., heart failure and cardiomyopathy), they affect the structure or function of the heart altering the quantity of blood that is pumped to meet the metabolic requirements of the body.

Imaging of the heart is crucial to detect and monitor changes of the cardiac muscle behaviour when cardiac diseases arise. Medical imaging techniques including echocardiography, magnetic resonance and radiography are used to image the heart and obtain clinical indicator of its functionality (Tee et al., 2013). Ejection fraction (EF) of the left ventricle (LV) is a relevant parameter to evaluate the performance of the heart by quantifying the percent of blood ejected out at each contraction from the LV. However, the assessment of LV deformations expressed in terms of strain has been demonstrated to be a more sensitive indicator than EF in several clinical scenarios (Tops et al., 2017). For instance, the evaluation of cardiac strain in patients with heart failure with preserved or normal ejection fraction may identify LV dysfunctions by showing reduction in peak systolic strain, whilst in individuals who are evaluated for cardiomyopathy may early detect sub-clinical LV dysfunction

(Smiseth et al., 2015). Therefore, cardiac strain imaging (CSI) has been increasingly adopted as a tool to study the functionality of the heart. Because of its large availability and versatility in the clinical setting, ultrasound 2D speckle tracking echocardiography (US-2D-STE) has become the most used technique to perform CSI. However, although extensive research has been carried out to investigate and validate the applications of this technique, fundamental limitations associated with its operating principle remain. In fact, US-2D-STE suffers from low image quality, the use of foreshortened views of the heart and out-of-plane motion. Moreover, the different software algorithms and parameters used by ultrasound vendors pose additional problems of standardisation of such methodology. Although US-2D-STE has been validated against sonomicrometry and MRI (Mor-Avi et al., 2011), the use of further experimental techniques for CSI can be very useful to understand the performance of 2D-STE and, eventually, provide reference measurements of cardiac strain.

A powerful technique for displacement and strain measurements is digital image correlation (DIC), an optical-numerical method originating from the experimental mechanics field (Sutton et al., 2009) but nowadays widely investigated to study the mechanical behaviour of biological tissues (Palanca et al., 2016). The principal reason for its popularity in biomechanics is that DIC can perform non-contact and full-field measurements of strain, features that are highly desired to characterise such supposedly anisotropic and inhomogeneous materials. The basic operating principle of DIC relies on tracking and matching subset of pixels between images captured before and after the specimen deformation using correlation criteria (e.g., cross-correlation or sum-squared difference correlation criterion (Pan et al., 2009c)). It is essential that the surface of the object investigated owns multiple and distinctive features (called *speckle pattern*) to enable unambiguous correlation, thus, when the natural surface pattern of the object is not sufficient, an artificial speckle pattern should be created (Dong and Pan, 2017). Indeed speckle pattern quality greatly af-

fects the accuracy and precision of the DIC measurements (Lecompte et al., 2006). Clearly, speckle pattern application in biological materials, especially in cardiovascular tissues, results a very complex task to address because the pattern should resist to their relatively large deformations and very moist surface (Palanca et al., 2016). Researchers from Tampere University of Technology in Finland applied for the first time DIC to study the behaviour of the human right ventricle during open-heart surgeries (Hokka et al., 2015; Soltani et al., 2018). Although they performed strain measurements *in vivo*, the challenging nature of the experiment and the lack of an effective speckle pattern on the heart surface severely reduced the reliability and accuracy of the results.

Aim and objectives

The aim of this study is to develop an experimental framework that enables the use of a full-field optical technique based on the 3D digital image correlation (3D-DIC) method to characterise *in vitro* and *ex vivo* displacement and strain in cardiac tissues and provide further measurements of cardiac strain, which can support the ongoing validation process of the existing clinical strain imaging modalities, i.e ultrasound 2D speckle tracking echocardiography (US-2D-STE) and improve the understanding of cardiac tissues deformations behaviour.

The aforementioned aim is achieved through the fulfilment of the following objectives:

1. Design a stereo vision system for dynamic imaging of heart deformations;
2. Develop a 3D-DIC workflow to obtain local and high resolution surface strain measurements;
3. Improve the procedure for speckle pattern application in cardiac tissues to enable 3D-DIC analysis;
4. Validate the accuracy of 3D-DIC measurements through experimental and numerical tests;
5. Apply the 3D-DIC method to characterise strain in an *in vitro* dynamic heart model;
6. Compare the performance of 3D-DIC and US-2D-STE in quantifying cardiac displacement and strain;
7. Explore the use of 3D-DIC in an *ex vivo* beating heart model.

Outline of the thesis

The thesis is divided into several chapters including the development and validation of the methodology and its applications in experimental models of the heart. In particular, the objectives of this thesis are achieved and described in the different chapters as follows:

- In Chapter 1, the background of this project is presented. This consists of an introduction of the cardiovascular system and relevant diseases that affect the cardiac muscle as well as the challenges of the current clinical imaging techniques to assess heart functionality. Afterwards, the operating principle and existing studies employing digital image correlation to characterise the biomechanics of cardiovascular tissues are reviewed.
- In Chapter 2, the design of a stereo optical system for dynamic and synced imaging of the heart deformation is reported (Objective 1). This is followed by the description of the workflow implemented in this study to perform localised and full-field deformation measurement using 3D-DIC (Objective 2). Finally, the procedure to obtain an effective speckle pattern on the cardiac surface of a porcine heart is illustrated (Objective 3) along with the validation of the developed methodology through experimental and numerical tests, providing error metrics of this techniques (Objective 4).
- In Chapter 3, the *in vitro* application of 3D-DIC to analyse full-field strain in a porcine heart model reproducing controlled and realistic loading conditions in the LV is reported. (Objective 5).
- In Chapter 4, combined measurements of 3D-DIC and US-2D- STE are performed *in vitro* under the same experimental conditions imposed to the heart. This study shows the high repeatability of 3D-DIC in performing a dynamic analysis of the heart deformation (Objective 6).

- In Chapter 5, a preliminary application of 3D-DIC in an *ex vivo* beating heart is presented. In particular, this chapter explores the potential and limitations of using this technique in a model of the heart closely resembling human *in vivo* cardiac mechanics (Objective 7).

List of publications

Parts of the work presented in this thesis have been disseminated through written publications and oral presentations, which are listed below.

Peer-reviewed journal publications

1. P. Ferraiuoli, L. S. Fixsen, B. Kappler, R. G. P. Lopata, J. W. Fenner, and A. J. Narracott. Measurement of *in vitro* cardiac deformation by means of 3D digital image correlation and ultrasound 2D speckle-tracking echocardiography. *Medical Engineering & Physics*, 74:146–152, dec 2019a. ISSN 13504533. doi: 10.1016/j.medengphy.2019.09.021
2. P. Ferraiuoli, B. Kappler, S. van Tuijl, M. Stijnen, B. A. de Mol, J. W. Fenner, and A. J. Narracott. Full-field analysis of epicardial strain in an *in vitro* porcine heart platform. *Journal of the Mechanical Behavior of Biomedical Materials*, 91 (November 2018):294-300, mar 2019. ISSN 17516161. doi: 10.1016/j.jmbbm.2018.11.025
3. P. Ferraiuoli, J. Taylor, E. Martin, J. Fenner, and A. Narracott. The Accuracy of 3D Optical Reconstruction and Additive Manufacturing Processes in Reproducing Detailed Subject-Anatomy. *Journal of Imaging*, 3(4):45, oct 2017. ISSN 2313-433X. doi: 10.3390/jimaging3040045

Conference proceedings and abstracts

1. P. Ferraiuoli, J. W. Fenner, M. C. M. Rutten, A. J. Narracott. *In vitro* strain measurements of stent-artery interactions using 3D digital image correlation method. *British Society for Strain Measurement 13th International Conference on Advances in Experimental Mechanics*, Southampton, UK, August 2018

2. P. Ferraiuoli, B. Kappler, S. van Tuijl, M. Stijnen, J. W. Fenner, A. J. Narracott. Optical strain measurements in a passive heart simulator loaded with different haemodynamic conditions. *Frontiers of Simulation and Experimentation for Personalised Cardiovascular Management and Treatment Conference*, University College London, UK, July 2018
3. P. Ferraiuoli, B. Kappler, S. van Tuijl, M. Stijnen, J. W. Fenner, A. J. Narracott. Full-field strain measurements in the dynamic cardiac biosimulator using 3D digital image correlation. *8th World Congress of Biomechanics*, Dublin, Ireland, July 2018
4. P. Ferraiuoli, J. W. Fenner, and A. J. Narracott. Analysis of Speckle Pattern Quality and Uncertainty for Cardiac Strain Measurements Using 3D Digital Image Correlation. In J. M. R. Tavares and R. Natal Jorge, editors, *VipIMAGE 2017*, volume 27 of *Lecture Notes in Computational Vision and Biomechanics*, chapter 96, pages 883-892. Springer International Publishing, Cham, 1 edition, 2018. ISBN 978-3-319-68194-8. doi 10.1007/978-3-319-68195-5_96
5. P. Ferraiuoli, A. K. Smith, J. W. Fenner, A. J. Narracott. Uncertainty of 3D-DIC in cardiac strain measurements using numerically deformed stereo images. *International Digital Image Correlation Society (iDICs) Conference*, Barcelona, Spain, November 2017
6. P. Ferraiuoli, J. W. Fenner, A. J. Narracott. 3D shape and full-field strain measurement in a coronary artery using 3D-DIC. *British Society for Strain Measurement 12th International Conference on Advances in Experimental Mechanics*, Sheffield, UK, August 2017

Chapter 1

Cardiovascular system and strain imaging techniques

1.1 Introduction

This chapter introduces the clinical background of this research and the optical-based digital image correlation (DIC) method employed in this study to analyse strain in the heart. Firstly, the basic anatomy and physiology of the cardiovascular system is described. Next, the most important diseases affecting behaviour and structure of the heart muscle are reviewed together with key metrics to quantify the heart function. Afterwards, the current challenges of application of ultrasound-based techniques used in the clinic to assess heart function are discussed with focus on cardiac strain imaging as a powerful tool to detect and monitor the progression of cardiac diseases. Finally, the fundamental operating principle and the existing applications of DIC in the cardiovascular field are presented.

1.2 Cardiovascular system

The heart is the key component in the cardiovascular system acting as a pump that delivers blood through the circulatory system to all the tissues and organs in the body.

1.2.1 Structure of the heart

The heart (Fig. 1.1) is divided into two sides that share the same configuration but different functionality: the right side with the right atrium (RA), which collects de-oxygenated blood from the body via the inferior and superior vena cava, and the right ventricle (RV), which pumps blood through the pulmonary valve and pulmonary arteries to the lungs where carbon-dioxide in the blood is exchanged with oxygen; the left side with the left atrium (LA), which receives oxygenated blood from the lungs via the pulmonary veins, and the left ventricle (LV), which pumps blood through the aortic valve and the aorta to all the tissues and organs in the body. Atria and ventricles communicate through the atrioventricular valves, the tricuspid valve between the RA and RV and the mitral valve between the LA and LV. Collagenous fibres, called *chordae tendineae*, connect the valves to the papillary muscles that extend from the inferior ventricular surface and control the opening and closing of the valves.

The wall of the heart (Fig. 1.2) is composed of three layers with different thickness: an inner layer called the *endocardium*, a middle layer called the *myocardium* and an outer layer called the *epicardium*. The inner and outer layers are composed of thin collagenous membranes, whereas the myocardium, the thickest layer, consists largely of cardiac muscle cells (*myocytes*) arranged into locally parallel muscle fibres. The epicardium is also called the visceral pericardium being the innermost layer of the *pericardium*, a membrane surrounding the heart made of an outer fibrous layer and an inner double layer of serous membrane. Moreover, the walls of the ventricles

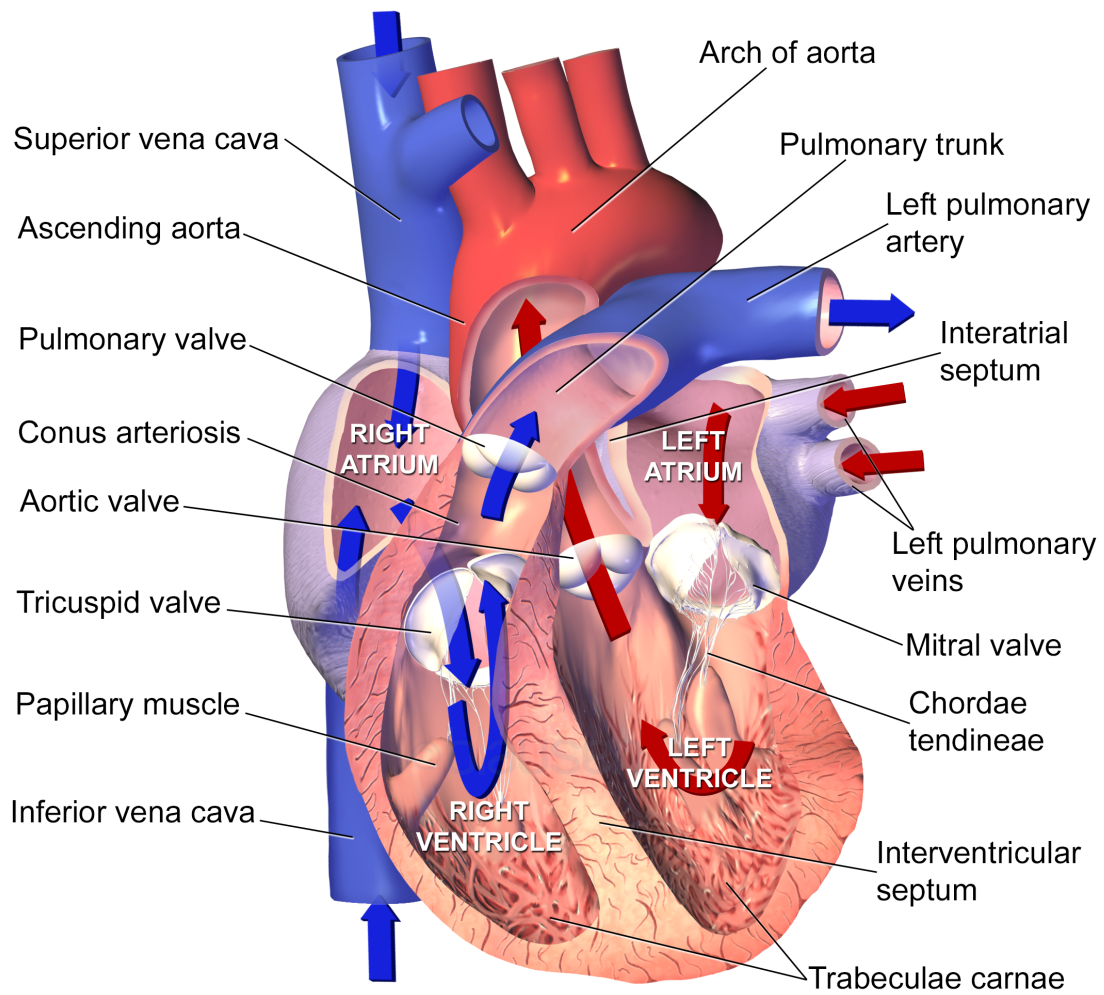


Figure 1.1: Sectional anatomy of the heart and pathway of blood flow. Image adapted from Blausen Medical Communications, Inc., distributed under the terms of the Creative Common CC BY 3.0 licence.

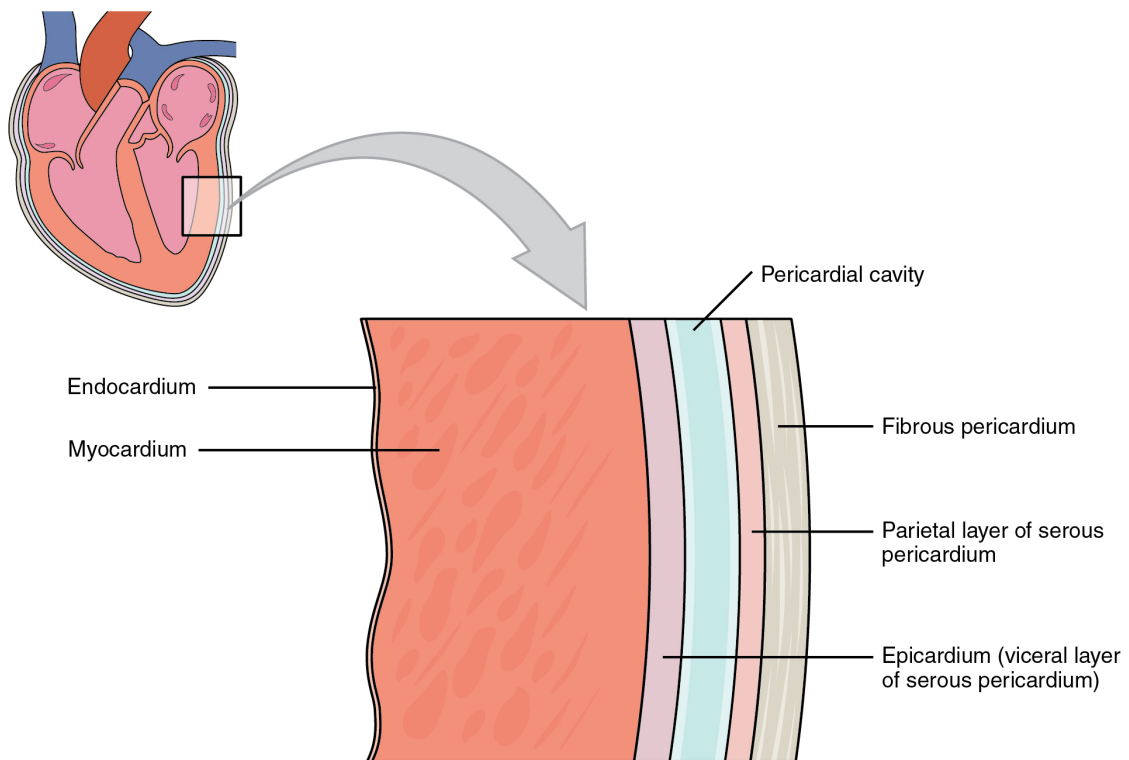


Figure 1.2: Wall layers of the heart. Image adapted from OpenStax College, distributed under the terms of the Creative Common CC BY 3.0 licence.

are characterised by ridges of cardiac muscle (*trabeculae carneae*) and a band of cardiac muscle (*moderator band* present only in the right ventricle).

1.2.2 Perfusion of the heart

The heart is perfused with blood via the coronary arteries originating at the root of the aorta. The left coronary artery (LCA) branches off from the left posterior aortic sinus and supplies blood to the left side of the heart, the left atrium and ventricle, and the interventricular septum, whereas the right coronary artery (RCA) branches off from the anterior aortic sinus and supplies blood to the right atrium, portions of both ventricles and the heart electrical conduction system. For a more detailed description of the coronary circulation refer to Berne and Levy (1967).

1.2.3 Cardiac pumping mechanism

The cyclic relaxations (i.e. *diastole*) followed by contractions (i.e. *systole*) of both the atria and ventricles (Fig. 1.3) allow the heart muscle to collect blood from the body and pump it into the arteries. In particular, it is possible to identify four separate phases in the cardiac cycle: i) all heart chambers are relaxed and the atrioventricular valves are open. This allows the returning blood from the body to fill the ventricles with approximately 80% of their capacity. The electrical impulses sent from the sinoatrial (SA) node to the atrioventricular (AV) node trigger the contraction of both atria contributing to empty them (atrial systole corresponding to the *a wave* in Fig. 1.3) and complete the ventricular filling (ventricular diastole); ii) depolarisation of the ventricles starts their contraction which increases the ventricular pressure. When this pressure exceeds the pressure in the atrium, the atrioventricular valves close. However, in this phase the pressure in the ventricles is still not enough to open the semilunar valves (aortic and pulmonary valves), thus the volume of blood within the chamber remains constant (*isovolumic ventricular contraction*). In this phase, the *c wave* in Fig. 1.3 corresponds to the bulging of the mitral valve into the atrium as atrial pressure increases; iii) continuous contraction of ventricular muscles raises the pressure within the ventricles becoming greater than the pressure in the aorta and pulmonary trunk. This pressure gradient causes the opening of the semilunar valves and the ejection of the blood from the ventricles (*ventricular ejection*); iv) ventricles start to relax following their repolarisation. Intraventricular pressure begins to fall and when it drops below the pressure within the aorta and pulmonary artery it causes a backflow of blood towards the heart (*dicrotic notch*) but the closure of the semilunar valves prevents the blood from flowing back into the ventricle. Since the atrioventricular valves are still closed in this phase (*v wave* in Fig. 1.3), the volume of blood in the ventricles remains constant (*isovolumic ventricular relaxation*). The LV and RV that propel blood into the aorta and pulmonary artery, respectively, work at different pressure levels. The LV operates at a higher

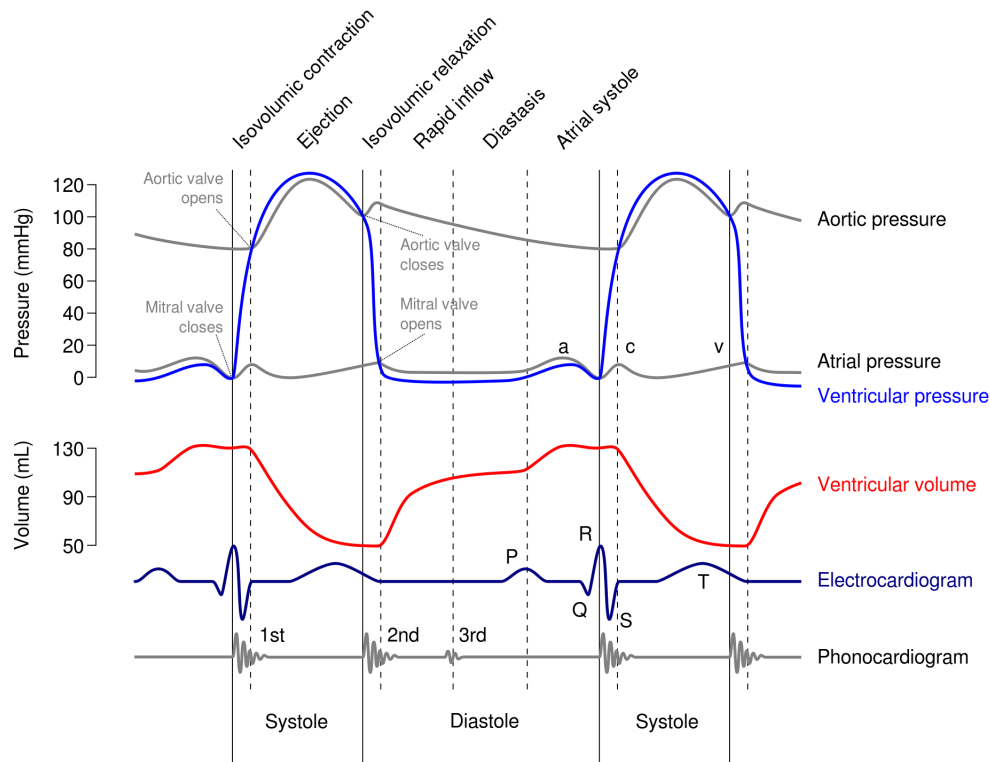


Figure 1.3: The Wiggers diagram showing the different phases and events within the cardiac cycle. The diagram reports time on the x-axis, while blood pressures (i.e. aortic, ventricular and atrial pressures), ventricular volume, electrocardiogram and heart sounds on the y-axis. Adapted from DanielChangMD revised original work of DestinyQx; Redrawn as SVG by xavax, distributed under the terms of the Creative Common CC BY 2.5 licence.

pressure (peak pressure about 120 mmHg) than the RV (peak pressure about 25 mmHg), since the former has to overcome resistances from the systemic circulation throughout the body while the latter only from the resistance of the lungs through the pulmonary circulation. This is also reflected in the different structure of the two ventricles with the LV myocardial layer being thicker to ensure blood is pumped at high pressure. It is clear that the effective contraction of the LV is crucial to ensure a blood supply to all the organs and tissues in the body.

The following sections describe the main cardiovascular diseases that affect the heart muscle and, in particular, the behaviour of the LV. A review of clinical techniques used to image the heart and extract information on its functionality is also provided.

1.3 Cardiovascular diseases

Cardiovascular diseases (CVDs) remain the leading cause of mortality in Europe accounting for 45% of all deaths (Wilkins et al., 2017). CVDs include a broad range of conditions that affect the heart and the blood vessels. CVDs involving the blood vessels, also known as vascular diseases, include coronary artery disease, peripheral arterial and cerebrovascular disease, which occur when the lumen of the artery narrows due to the build-up of plaque (e.g. *atherosclerosis*) causing an alteration of the blood flow that reaches the tissues and organs (e.g., heart, brain). In addition to diseases involving the circulation, there are specific conditions of the cardiac muscle such as cardiomyopathy that alter the structure and function of the heart, potentially leading to heart failure as the ability of the heart to effectively pump blood and meet the requirements of the body is compromised. Different types of cardiomyopathy are characterised depending on how the structure of the heart muscle is affected (Mozaffarian et al., 2016). Specifically, *Dilated cardiomyopathy* weakens the pumping action of the heart as the wall of the ventricular muscle becomes enlarged and thin. *Hypertrophic cardiomyopathy* reduces the volume of blood that the ventricles can host and makes harder for the heart to pump blood because of the thickening of the muscle of the ventricles. *Restrictive cardiomyopathy* prevents the walls of the heart chambers from fully relaxing to fill with blood because of the stiffening of the heart muscle.

The historical indicator used to classify the types and severity of heart failure is the left ventricular ejection fraction (LVEF) (Ponikowski et al., 2016) that quantifies the amount of blood that is ejected from the left ventricle at each heartbeat. The LVEF is calculated by dividing the *stroke volume* (SV) by the *end diastolic volume* (EDV), with SV defined as the difference between EDV and the end systolic volume (ESV). The LVEF has been shown to be an accurate predictor of clinical outcome in patients with heart failure with an LVEF less than 40% (heart failure with reduced LVEF). In patients with heart failure symptoms and an LVEF greater than 40%

(heart failure with normal or preserved LVEF), LVEF does not provide a comprehensive characterisation of the LV function (Ponikowski et al., 2016). In particular, LVEF as a global measure of LV activity may neglect the detection of regional cardiac tissues diseases, especially when structural changes of the myocardium occur impairing the LV contractility. Moreover, as volume-derived index, LVEF has several limitations including geometric assumptions regarding the shape of the ventricle and load dependency that result in a considerable loss of reproducibility (Cikes and Solomon, 2016).

A promising clinical indicator, which may overcome LVEF limitations and provide a more comprehensive representation of LV functionality, is the evaluation of cardiac strain that can describe the local shortening, thickening and lengthening of the myocardium during a cardiac cycle (Smiseth et al., 2015). In addition to providing a regional characterisation of cardiac muscle behaviour, allowing for early classification of myocardial dysfunction into different subtypes (Dandel et al., 2009), cardiac strain assessment has been demonstrated to be more sensitive than LVEF to detect subtle changes in LV systolic function (Tops et al., 2017). The most important applications of cardiac strain measurement may include (Smiseth et al., 2015): the diagnosis of myocardial ischemia by showing reduction in peak systolic strain; the prediction of coronary heart disease; the assessment of myocardial viability; the evaluation of systolic function in patients with hypertrophic cardiomyopathy, the identification of systolic dysfunction in patients with heart failure with preserved LVEF.

Both LVEF and cardiac strain are parameters that can be extracted from the imaging of the heart using techniques such as echocardiography, magnetic resonance imaging and computed tomography. In the next section, a particular emphasis is given to the ultrasound-based methods widely found in the clinical setting to quantify cardiac strain. For a complete review of the different cardiac imaging techniques please refer to Tee et al. (2013); Jan and Tajik (2017); Mawad and Mertens (2018).

1.3.1 Overview of medical imaging techniques for cardiac strain

Amongst the range of tools used in the clinic to diagnose and monitor the progression of CVDs, cardiac imaging plays a central role in providing qualitative and quantitative information about the physiology and pathophysiology of the heart. As discussed in the previous section, the function of the LV can be evaluated through the assessment of LVEF and cardiac strain, although the former has some limitations in identifying specific heart conditions. In this section, the basic concept and terminology of strain are provided within the cardiac imaging context.

1.3.1.1 Strain definition

Originating from the continuum mechanics field, strain is a dimensionless parameter used to describe the magnitude of the deformations which cardiac tissues undergo during a cardiac cycle. In its simplest representation for a 1D object (Fig. 1.4), strain (ε) can be written as:

$$\varepsilon = \frac{L - L_0}{L_0} = \frac{\Delta L}{L_0} \quad (1.1)$$

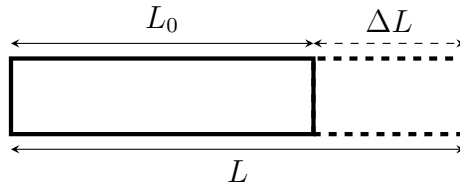


Figure 1.4: Strain in a 1D object occurs only as lengthening ($\varepsilon > 0$) or shortening ($\varepsilon < 0$) of the material.

where L_0 is the original length of the object, L is the length of the object after the deformation; with $\varepsilon < 0$ and $\varepsilon > 0$ indicating shortening and lengthening of the object, respectively. This is also called the *engineering strain* (Eq. 1.1).

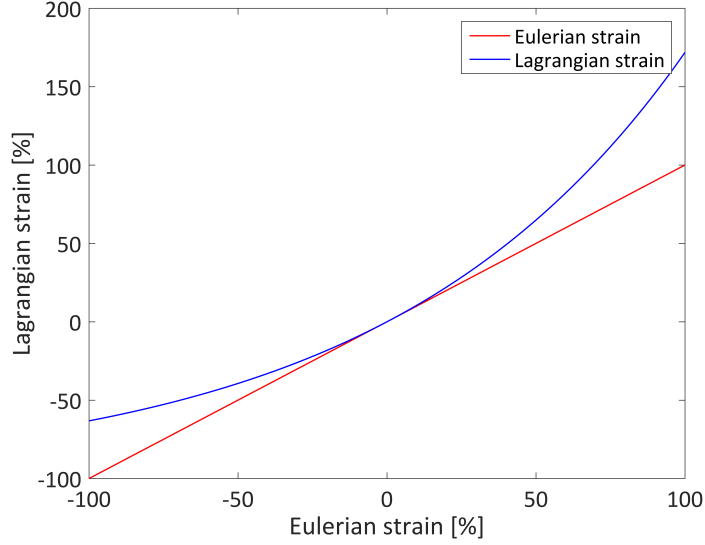


Figure 1.5: Relationship between Eulerian and Lagrangian strain obtained using the following equation $Lagrangian\ strain = e^{Eulerian\ strain} - 1$.

When changes in length of the object are known throughout the deformation process, it is possible to define the *instantaneous* strain as:

$$\varepsilon(t) = \frac{L(t) - L(t_0)}{L(t_0)} \quad (1.2)$$

where $L(t)$ is the length of the object at the time t and $L(t_0) \equiv L_0$ is the initial length. In this case, the instantaneous strain is computed relative to an initial object configuration (reference state) and is called *Lagrangian strain*. Moreover, strain can also be calculated relative to the object configuration at a previous time instance (current state) and is called *Eulerian strain*. As shown in Fig. 1.5, for a strain magnitude smaller than 10%, Lagrangian and Eulerian strains are approximately equal, while for larger strains, similar to those occurring during LV deformations at end-systole, differences can become significant (Amzulescu et al., 2019). In fact, normal values of strain across the heart layers range between 17 and 23% (Nagata et al., 2017).

For 2D objects, lengthening or shortening can occur along the x- and y-axis, as shown in Fig. 1.6. In this case, strain may have multiple components, which depend-

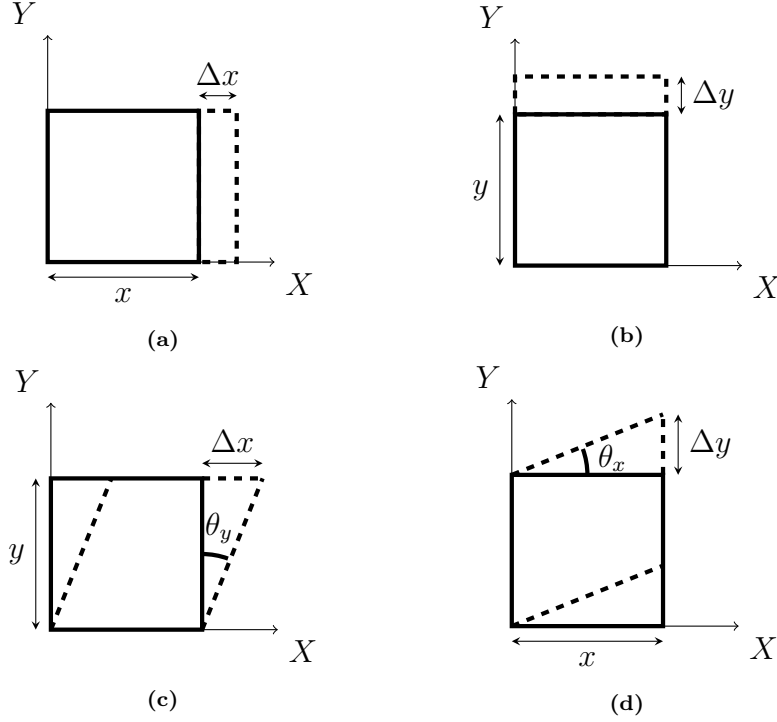


Figure 1.6: Strain in a 2D object can be characterised by four components: two normal strain components ε_x and ε_y , (a) and (b), respectively; and two shear strain components ε_{xy} and ε_{yx} , (c) and (d), respectively. Shear strain components are associated with the angles θ_x and θ_y .

ing whether deformations are perpendicularly or parallel to the object cross-section, are referred to *normal strains* ($\varepsilon_x, \varepsilon_y$) and *shear strains* ($\varepsilon_{xy}, \varepsilon_{yx}$), respectively:

$$\left\{ \begin{array}{l} \varepsilon_x = \frac{\Delta x}{x} \quad \text{and} \quad \varepsilon_y = \frac{\Delta y}{y} \\ \varepsilon_{xy} = \frac{\Delta x}{y} \quad \text{and} \quad \varepsilon_{yx} = \frac{\Delta y}{x} \end{array} \right. \quad (1.3)$$

However, as the heart is a 3D object it undergoes complex 3D deformations during the cardiac cycle, which can be described in terms of a local 3D coordinate system (D’Hooge et al., 2000) with: a *radial axis* (normal to the epicardial surface and pointing outward from the heart cavity; *longitudinal axis* (tangential to the epicardial surface and, thus, normal to the radial axis, pointing toward the base of the heart) and *circumferential axis* (normal to radial and longitudinal axes defining a right-handed coordinate system). In addition to strains along these three com-

ponents, as seen before, cardiac tissue also typically undergoes shear strains (i.e., longitudinal-radial, circumferential-radial and circumferential-longitudinal shear). Nonetheless, to date, most focus has been on the normal components (radial, longitudinal and circumferential strains) for clinical assessment, although measurement of the circumferential-longitudinal shear strain can give an estimate of the twist of the heart, a measure that may provide valuable insights in the clinical assessment of myocardial diseases (Omar et al., 2015). Throughout the cardiac cycle, it is possible to observe cyclic deformation behaviour of the LV: during diastole it undergoes longitudinal and circumferential lengthening (positive strain) and radial thinning (negative strain); whereas in systole it undergoes longitudinal and circumferential shortening and radial thickening.

1.3.1.2 Echocardiography methods

Although cardiac magnetic resonance imaging (cMRI) is deemed the gold standard technique for the quantitative assessment of myocardial strain, the requirement for highly-trained operators, the complex and lengthy analysis, the unavailability for patients with intra-cavity devices and claustrophobia restrict its application to mainly academic environments and research studies (Tee et al., 2013). Whereas, echocardiography has become the most established imaging modality to quantify the functionality of the LV in a clinical setting because of its high availability, portability, unique ability to provide non-invasive and real-time images of the beating heart (Jan and Tajik, 2017). In particular, the term echocardiography refers to all the ultrasound-based techniques used to image the heart and derive useful information on its functionality.

Initial measurements of cardiac strain were performed using Doppler techniques such as tissue Doppler imaging (TDI), which track the instantaneous velocity of a point on the myocardium in one frame and, then, using the relation between velocity and strain rate (strain per time unit), allows the reconstruction of strain

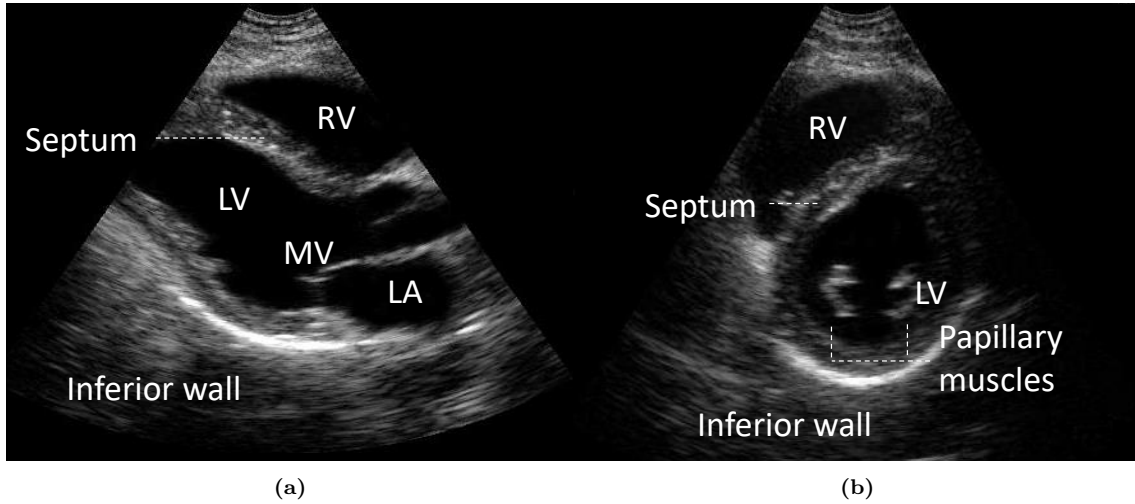


Figure 1.7: B-mode ultrasound image of the heart along the longitudinal-axis (LAX) (a) and short-axis (SAX) (b).

curves. However, TDI-derived strain may not truly represent actual contractions of the heart since measuring myocardial velocities includes also tethering and/or translational motion of the heart (Nesbitt et al., 2009). Moreover, as a Doppler technique, TDI provides velocity measurements along one-dimension (i.e. the ultrasound beam direction), whilst the heart deforms in 3D, thus, results are dependent on the angle of incidence between the ultrasound probe and the cardiac tissue under investigation.

An alternative echocardiographic method, which has largely replaced Doppler-based approaches for cardiac strain imaging (CSI), is ultrasound 2D speckle tracking echocardiography (US-2D-STE) (Nesbitt et al., 2009). This method consists in tracking natural acoustic markers in B-mode images that are created by constructive and destructive interference of ultrasound waves with the tissue structure, denoted as *speckles*, as shown in Fig. 1.7.

Usually, block-matching algorithms based on a similarity measure (e.g., cross-correlation criterion) are adopted to track kernels of speckles in consecutive frames and provide the local displacement of a tissue segment (Tee et al., 2013). Afterwards, radial, circumferential and longitudinal strains are calculated by taking the spatial derivative of the displacement field in the radial, circumferential and longitudinal

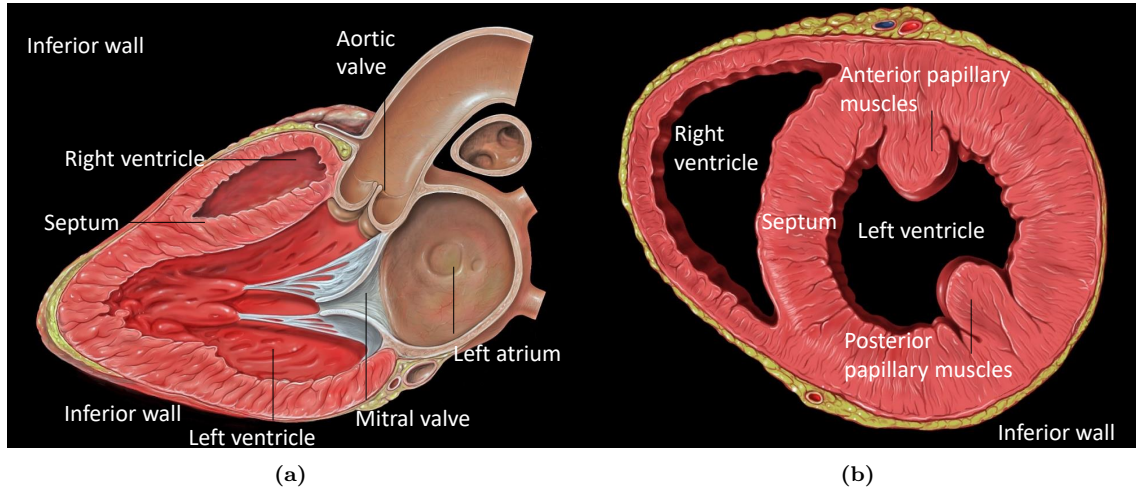


Figure 1.8: Sectional anatomy of the heart along the longitudinal-axis view (LAX) (a) and short-axis view (SAX) (b). Image adapted from Patrick J. Lynch, medical illustrator, distributed under the terms of the Creative Common CC BY 2.5 licence.

direction, respectively. In particular, circumferential and longitudinal strains can be extracted from the short-axis (SAX, Fig. 1.8a) and long-axis (LAX, Fig. 1.8b) views of the heart, respectively, while radial strains can be extracted from both views. A robust and relevant parameter of LV functionality, obtained from the long-axis view, is the global longitudinal strain (GLS), an average measure of the strains across the cardiac tissue segments (Kalam et al., 2014). Specifically, GLS has proved to be a very important indicator of different cardiac diseases especially to predict clinical outcomes in patients with heart failure and preserved LVEF (Tops et al., 2017) as well as to assess cardiomyopathies (Nesbitt et al., 2009). Moreover, the principal strain configuration has been adopted to analyse sub-clinical changes in left ventricular function to remove dependency from a coordinate system (Pedrizzetti et al., 2014).

1.3.1.3 Challenges and limitations of US-2D-STE

US-2D-STE has been validated in animals against sonomicrometry and in humans against tagged MRI, and it has become an effective clinical tool for quantifying myocardial strain (Amundsen et al., 2006). However, several limitations associated with its fundamental operating principle and the tracking process pose considerable

challenges in the interpretation and accuracy of strain results (Voigt et al., 2015). Specifically, despite being less angle dependent than TDI because tracking of the speckles can be performed both along the axial and perpendicular (lateral) directions of the ultrasound probe, measurements along the lateral direction are less accurate as ultrasound images typically have worse resolution perpendicular to the ultrasound beam compared to the axial direction. Therefore, US-2D-STE requires very good image quality and spatial resolution, typically achieved with low frame-rate acquisitions. However, use of a low frame rate may cause a loss of speckles that may move outside the correlation region in successive frames. Moreover, US-2D-STE suffers from the inherent limitations of 2D imaging which relies on the use of foreshortened views and the assumption that myocardial tissues deform within the 2D imaging plane (*in plane*), whereas the cardiac muscle exhibits complex 3D deformation (e.g., twisting). Thus, the tracked speckles may be lost during through-plane motion of the heart in the cardiac cycle, an issue that is very frequently observed in radial and circumferential strain measurements as short-axis views are more sensitive to *out-of-plane* motion of the speckles (Voigt et al., 2015). Furthermore, ultrasound speckle patterns are not temporally stable since they are generated by the interference of the ultrasound waves back-scattered from tissue structures, which may be altered throughout the cardiac cycle by the biological changes of living tissues and changes of interrogation angle between the investigated tissue and the ultrasound line (Voigt et al., 2015). Although the development of US-3D-STE techniques can overcome certain limitations, i.e. the ability to track the out-of-plane displacement of the speckles, the limited spatial and temporal resolution of US-3D-STE as well as the lower image quality than its 2D counterpart still limit the diagnostic value of the 3D technology (Mawad and Mertens, 2018).

1.4 Optical techniques for strain measurements

Optical techniques are increasingly used in the field of experimental mechanics to analyse surface displacement and strain in materials and structures (Rastogi, 2000). Contrary to conventional techniques (i.e. strain gauges) which only allow for point-wise measurements, optical techniques have the advantage of allowing full-field and non-contact measurements of object deformations. Optical methods can be distinguished as: i) interferometric techniques (e.g., moiré interferometry, speckle interferometry and holography interferometry), which retrieve the deformation by measuring the difference in phase of the scattered light wave from the specimen surface before and after the deformation using a coherent light source in a vibration-free environment; ii) non-interferometric techniques (e.g., grid method and digital image correlation), which measure the deformation by comparing the change in intensity level in the images of the specimen surface captured before and after the deformation.

1.4.1 Digital Image Correlation

Amongst non-interferometric techniques, digital image correlation (DIC) has seen widespread application in several research and industrial fields (Sutton et al., 2009; Pan, 2018). In fact, because of its flexibility, relatively easy implementation, simple and low-cost experimental setup, robustness to external experimental conditions (e.g., vibration and light variations), DIC has been adopted in new areas including aerospace, automotive, civil engineering, material sciences and biomechanics. In particular, DIC measurement can offer a detailed and localised surface map of displacement and strain with adjustable temporal and spatial resolution providing a comprehensive characterisation of the mechanical behaviour of the specimen. Moreover, the non-contact nature allows for less invasive measurements of the mechanical response of the material, resulting in an important feature for testing soft tissues.

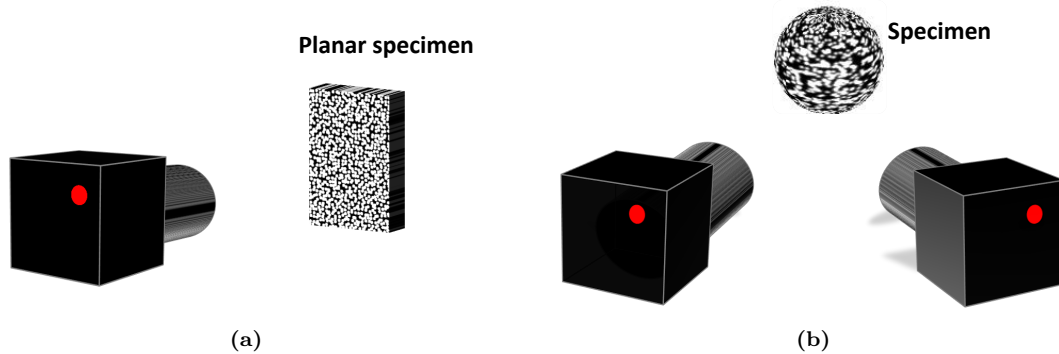


Figure 1.9: Schematic representation of the 2D-DIC (a) and 3D-DIC (b) experimental setup.

Depending on the number of cameras used to image the object deformation, a distinction is made between 2D- and 3D-DIC. The former, using only a single camera, allows in-plane measurements in planar objects whose surface should be placed perpendicular to the camera optical axis (Fig. 1.9a). However, 2D-DIC is very sensitive to out-of-plane motion, with in-plane strain errors being proportional to $\Delta Z/Z$ (where Z is the distance from specimen to the camera sensor and ΔZ the out-of-plane translation (Sutton et al., 2008b). Although the use of telecentric lenses or placing the specimen far from the camera may mitigate out-of-plane motion effects (Sutton et al., 2008b), only the use of an additional camera enabling stereo imaging (i.e. the use of two cameras) can reveal out-of-plane displacements (Fig. 1.9b). In fact, 3D-DIC (or stereo-DIC) combines stereo imaging to provide two different views of the object with the DIC method employed to address the stereo correspondence problem (Luo et al., 1993; Sutton et al., 2009; Orteu, 2009). In particular, knowing camera calibration data (i.e. the intrinsic and extrinsic parameters) and performing triangulation of the corresponding points in the image pair, 3D reconstruction of the points coordinates of the object surface can be achieved. In the next sections, the basic operating principle of DIC and its more relevant applications to study displacement and strain in cardiovascular tissues are discussed. For a wider overview of the historical developments and use of DIC in biomechanics, readers are encouraged to see Pan (2018) and Palanca et al. (2016), respectively.

1.4.1.1 Basic operating principle

DIC is an optical-numerical method that consists in processing digital images of the test-object surface acquired during its deformation and using numerical approaches to extract quantitative measurements of displacement and strain (Peters and Ranson, 1982; Sutton et al., 2009). Digital images stored as matrices of values representing the grey intensity levels of each pixel (e.g., values ranging from zero to 256 for a 8-bit digitisation) are compared to determine how a local neighbourhood of pixels (set of intensity values) displaces between states before and after the deformation. Subsets of pixels are matched rather than individual elements because they can be more uniquely identified since they encompass a wider variety of grey intensity levels. To ensure effective correlation, especially when the natural texture of the object surface does not result in distinctive features in the image, a high-contrast stochastic pattern (*speckle pattern*) is artificially created using a range of techniques (Dong and Pan, 2017).

Three phases are involved in the subset-based DIC approach: i) a region of interest is selected in the reference image and evenly divided into multiple subsets, whose size and spacing are defined by the user (the subset size and step size, respectively); ii) matching algorithms and optimisation of sub-pixel registration algorithms are applied to provide full-field displacement fields at sub-pixel accuracy; iii) the full-field strain distribution is obtained through the differentiation of the displacement field. As illustrated in Fig. 1.10, after selecting a region of interest (ROI), the subset size and step size, the square reference subset of $(2N + 1) \times (2N + 1)$ pixels centered at (x_0, y_0) in the reference image is tracked in the deformed image and matched with the deformed subset centered at (x'_0, y'_0) . This operation is performed at each point in the virtual grid to obtain full-field deformations. In particular, the degree of similarity between the reference subset and deformed subset is evaluated using a cross-correlation criterion or sum-squared differences correlation criterion, which provides an initial estimate of displacement at integer-pixel accuracy (Pan et al.,

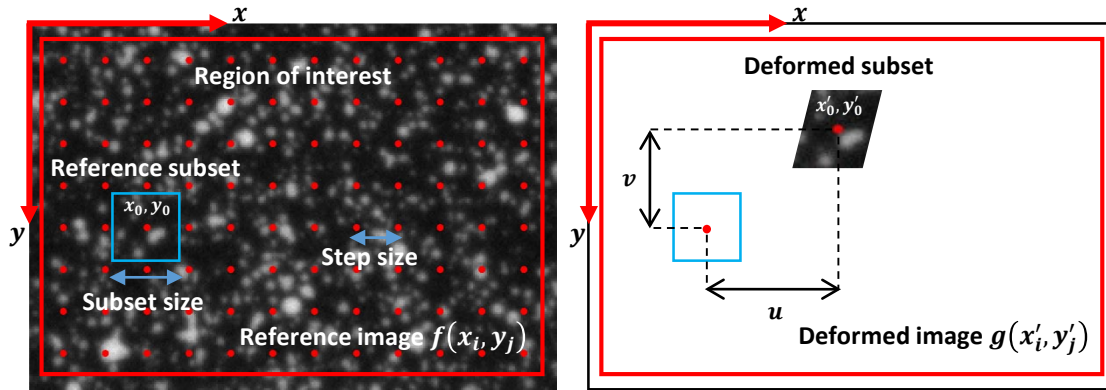


Figure 1.10: Schematic representation of a reference subset centred at (x_0, y_0) before deformation (reference image) and the corresponding deformed subset centred at (x'_0, y'_0) after deformation (deformed image). Size and spacing of the subset are defined by the *subset size* and *step size*, respectively. u and v are the components of the displacement vector mapping the position of the reference subset in the reference image to the position of the deformed subset in the deformed image.

2009b). A very robust and recommended metric for practical DIC experiments is the zero-normalised sum of squared differences (ZNSSD, Eq. 1.4) because it is insensitive to both scale and offsets in illumination which may result from lighting fluctuations in the deformed image (Pan, 2018).

$$C_{ZNSSD} = \sum_{i=-M}^M \sum_{j=-M}^M \left[\frac{f(x_i, y_j) - f_m}{\Delta f} - \frac{g(x'_i, y'_j) - g_m}{\Delta g} \right]^2$$

$$f_m = \frac{1}{(2M+1)^2} \sum_{i=-M}^M \sum_{j=-M}^M f(x_i, y_j),$$

$$g_m = \frac{1}{(2M+1)^2} \sum_{i=-M}^M \sum_{j=-M}^M g(x'_i, y'_j), \quad (1.4)$$

$$\Delta f = \sqrt{\sum_{i=-M}^M \sum_{j=-M}^M \left[f(x_i, y_j) - f_m \right]^2},$$

$$\Delta g = \sqrt{\sum_{i=-M}^M \sum_{j=-M}^M \left[g(x'_i, y'_j) - g_m \right]^2},$$

where $f(x_i, y_j)$ and $g(x'_i, y'_j)$ are the grey intensity levels at coordinates (x_i, y_j) and (x'_i, y'_j) in the reference subset and deformed subset, respectively; f_m and g_m represent the mean intensity values of the reference and deformed subset, respectively; and Δf and Δg denote the standard deviation of the intensity values of the reference and deformed subset, respectively.

The displacement of a point (x_i, y_j) in the reference subset can be mapped to the point (x'_i, y'_j) in the deformed subset using a displacement mapping function, also called a *shape function*. Depending on the anticipated deformation, first- or second-order shape functions are commonly used in DIC. A first-order displacement mapping function can describe subsets translation, rotation, normal and shear strains and their combinations:

$$\begin{aligned} x' &= x_0 + \Delta x + u + u_x \Delta x + u_y \Delta y, \\ y' &= y_0 + \Delta y + v + v_x \Delta x + v_y \Delta y. \end{aligned} \quad (1.5)$$

Whereas, a second-order shape function is usually employed to represent more complex deformation states of the deformed subset (Lu and Cary, 2000):

$$\begin{aligned}x' &= x_0 + \Delta x + u + u_x \Delta x + u_y \Delta y + \frac{1}{2} u_{xx} \Delta x^2 + \frac{1}{2} u_{yy} \Delta y^2 + u_{xy} \Delta x \Delta y, \\y' &= y_0 + \Delta y + v + v_x \Delta x + v_y \Delta y + \frac{1}{2} v_{xx} \Delta x^2 + \frac{1}{2} v_{yy} \Delta y^2 + v_{xy} \Delta x \Delta y.\end{aligned}\tag{1.6}$$

In equations (1.5) and (1.6), u and v are the displacement components of the reference subset centred at (x_0, y_0) along the x - and y -axis, respectively, as shown in Fig. 1.10; $\Delta x = x - x_0$ and $\Delta y = y - y_0$ are the distances between the subset centre to point (x, y) ; u_x, u_y, v_x, v_y are the first-order displacement gradient components of the reference subset, while $u_{xx}, u_{xy}, u_{yy}, v_{xx}, v_{xy}, v_{yy}$ are the second-order displacement gradient components of the reference subset.

The combination of sub-pixel registration algorithms with interpolation schemes is adopted to optimise a pre-defined function (e.g., the equation (1.4)) to achieve displacement sub-pixel accuracy and obtain full-field measurements (Pan et al., 2009b). In particular, to solve the correlation function equation, which has 6 or 12 unknown parameters depending on the order of the shape function used, a non-linear numerical optimisation method such as the classic Newton-Raphson (NR) method (Bing et al., 2006) can be used. A more efficient method based on the inverse compositional matching strategy combined with the Gauss-Newton (IC-GN) (Baker and Matthews, 2005) for fast, robust and accurate full-field displacement measurement has been proposed for use in DIC (Pan et al., 2013). Because digital image resolution is at a pixel level, the implementation of a sub-pixel registration algorithm requires a specific interpolation scheme such as bi-quintic B-spline functions to reconstruct the intensity levels at sub-pixel locations (Sutton et al., 2009).

As the NR and IC-GN methods are local iterative optimisation algorithms they both require an initial guess for the deformation, which should closely approximate the true value in order to start the iteration and ensure convergence. Since the deformation is generally quite small between the reference and deformed subset, the

initial displacement can be easily estimated with an integer displacement searching scheme implemented either in the spatial or frequency domain (Pan et al., 2009b). The approach called reliability-guided DIC (RG-DIC) has been demonstrated as a more effective and robust tool to provide an automate and accurate initial guess (Pan, 2009) and is now widely adopted in practical DIC measurements (Blaber et al., 2015). It is worth mentioning that although the optimisation of the ZNSSD is much easier to accomplish (Pan et al., 2013), the optimised ZNSSD coefficient is converted to the more commonly used zero-normalised cross-correlation (ZNCC) coefficient, according to the relation described in Pan et al. (2010), and used as a quality measure to guide the reliability process and ensure accurate displacement initial guess (Pan et al., 2013). A more detailed description of non-linear optimisation methods to perform subpixel registration (i.e. the NR and IC-GN method) and the RG-DIC approach for DIC measurements can be found in Pan et al. (2013); Pan and Wang (2016); Pan (2009).

A straightforward estimation of the strain can be obtained via the displacement gradient components:

$$\begin{aligned}
 e_x &= u_x + \frac{1}{2}(u_x^2 + v_x^2), \\
 e_y &= v_y + \frac{1}{2}(u_y^2 + v_y^2), \\
 e_{xy} &= \frac{1}{2}(u_x + v_x) + \frac{1}{2}(u_x u_y + v_x v_y).
 \end{aligned}
 \tag{1.7}$$

However, with this approach, involving numerical differentiation, any noise in the displacement fields will be amplified in the strain distributions. Therefore, smoothing of the computed displacement field first followed by differentiation is often employed to improve strain accuracy (Sutton et al., 2009). Furthermore, more practical techniques based on the pointwise least squares algorithm have been proposed to extract strain fields from the displacement fields (Pan et al., 2009a).

1.4.1.2 Applications of DIC in cardiovascular tissues

The first attempts to use DIC to characterise the mechanical behaviour of cardiovascular tissues were made by Zhang et al. (2002); Zhang and Arola (2004). Specifically, the authors used 2D-DIC to quantify the elastic modulus and Poisson's ratio in arterial tissues, excised from the bovine aorta, during uni-axial tensile tests. However, the out-of-plane displacement error introduced by the 2D system was shown to affect the outcome of the strain results. In order to overcome issues related to 2D-DIC, a microscope system (field of view of 2×2 mm) combined with 3D-DIC was adopted to evaluate the strain distribution in a pressurised mouse carotid artery (vessel diameter of 450μ and length of 4 mm) (Sutton et al., 2008a). An almost linear response between pressures applied and strains was observed, with values of strain reaching 15% at an internal pressure of 240 mmHg. Moreover, experimental results proved that such a technique could be adopted to investigate changes in local biomechanical response at the microscale.

Following these pioneering studies, DIC has been adopted by several researchers to investigate the mechanical behaviour of the arteries and heart under different conditions. For instance, different works have been carried out to assess strain in coronary arteries using the DIC technique both during *in vitro* and *ex vivo* experiments. In a preliminary experiment (Horny et al., 2012), 3D-DIC was applied to assess strains in *ex vivo* human coronary arteries during the expansion of a stent. A very large value of strain ($\sim 50\%$) on the artery surface was estimated at the peak pressure applied during the stent deployment and non-symmetrical strain distribution along the length of the coronary artery was observed. In a further study, a comprehensive analysis of the strain distribution at different phases of the stent expansion (i.e. expansion, pressurisation and recoil) was performed using 3D-DIC (Zhao et al., 2013). The *in vitro* results were compared with a computational model reproducing the stenting procedure showing a difference of about 7%. However, an important limitation of this work was the dimensions of the vessel analogue (inner

diameter of 6.32 mm and wall thickness of 1.55 mm), which were twice as large as those of human coronary arteries. In several other studies DIC has been employed as a tool to quantify the elastic modulus of healthy and atherosclerotic human coronary arteries during *ex vivo* tensile tests (Karimi et al., 2013) and to verify the hypothesis of incompressibility of the coronary arterial walls by measuring the Poisson's ratio (Karimi et al., 2016).

To avoid potential issues arising from stereo imaging such as the requirement for two cameras to be synchronised and ideally with the same optical parameters, optical systems involving only a single camera have been devised to enable 3D-DIC (Pan et al., 2017). To study the behaviour of vessel-shaped specimens, a panoramic DIC system was devised by Genovese et al. (2011a,b). In particular, a single camera placed within a conical mirror and coupled with a gimbal-mounted mirror, to provide multiple views, was used to measure surface strain fields along the full-length and around the entire circumference of a pressurised tubular sample using 3D-DIC. The reliability of this approach was assessed computing the error in the shape reconstruction of a cylinder of 1 mm diameter, found smaller than 2%, and in a zero-strain test, which produced mean strain errors smaller than 0.6 % with a standard deviation of approximately 2%. An improved version of this panoramic DIC system was later proposed (Genovese et al., 2013) and adopted to collect full-field biaxial data in a mouse model of dissecting abdominal aortic aneurysm (Genovese et al., 2012) as well as to perform an inverse characterisation of regional variation in the properties of murine aortas (Bersi et al., 2016). In fact, the dense set of full-field data that DIC provides can be very useful for inverse material characterisation. For instance, using 3D-DIC full-field displacement and strain data obtained during an inflation test of a human aortic aneurysm and an inverse procedure, Kim et al. (2012) calculated the material parameters and stress components to identify the rupture of the aneurysm.

Concerning applications more closely related to the focus of this thesis, DIC has been employed to study displacement and strain in the heart muscle under

different experimental conditions. In particular, an optical system including 2D-DIC was designed to extract full-field displacement measurements on the surface of a porcine ventricle slab during an indentation test (Genovese et al., 2015). The developed method captured the asymmetrical deformation of this in-homogeneous and anisotropic tissue, which was also compared with the response to an indentation of a homogeneous and isotropic latex foam. Moreover, the full-field surface map of the maximum principal strain on the ventricle slab showed further the presence of tissue anisotropy and maximum values of strain of approximately 8% close to the indenter. Recently, researchers from Tampere University of Technology in Finland employed 3D-DIC to monitor *in vivo* the deformation behaviour of the right ventricle in patients undergoing a cardiopulmonary bypass surgery. In particular, Hokka et al. (2015) placed stereo cameras in the operating theatre above the chest of the patient and captured images during surgery at 10 frame per second. 3D-DIC analysis was performed using a commercial software and subset and step size of 121×121 and 1×1 pixels, respectively. Measurements of maximum principal strain on the right side of the heart ranged between 0 and 15%. However, the challenging nature of the experiment severely limited the control of error sources arising from 3D-DIC. Moreover, since only the natural surface texture of the heart was considered in the pattern matching, this resulted in a loss of accuracy and resolution, requiring the use of a large subset size. In a subsequent work, Soltani et al. (2018) attempted to create a speckle pattern on the heart surface using a biocompatible marker. However, as shown in Fig. 1.11, this appeared to be a very coarse pattern considering the field of view of approximately 700×700 pixels, the number of speckles applied and the large subset size used in the analysis (79 pixels). Therefore, 3D-DIC measurements reported in the aforementioned study were still affected by low resolution and absence of error metrics (i.e. accuracy and precision).

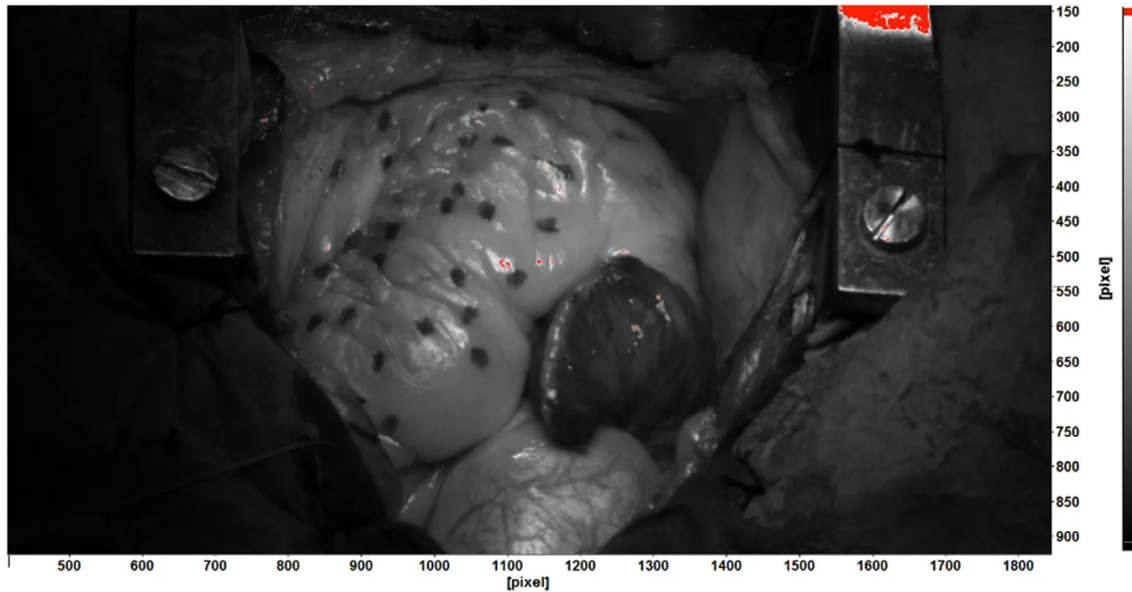


Figure 1.11: Image of the speckle pattern applied on the human heart and used for 3D-DIC analysis. This figure has been taken from Soltani et al. (2018), an open access article distributed under the terms of the Creative Common CC BY 4.0 licence.

1.5 Summary

This chapter reviews the clinical background, the operating principle and applications of the methodology employed in this study to perform strain measurements in cardiovascular tissues. Firstly, the structure and functioning of the cardiovascular system is illustrated, highlighting also the diseases that affect the heart muscle. Then, the existing tools used to evaluate the functionality of the heart are discussed, in particular, the ultrasound 2D speckle tracking technique, currently the most used in clinic, is described showing the limitations associated with its use. Finally, this chapter introduces the working principle and relevant biomedical applications of the digital image correlation (DIC) technique. Although, this technique cannot replace non-invasive clinical imaging of the heart being an optical method, 3D-DIC has the potential to perform a high resolution and accurate measurement of deformations in *in vitro/ex vivo* model of the heart, as shown in the later chapters.

Design of a 3D-DIC system for cardiac strain assessment

2.1 Introduction

This project builds on previous works carried out within the Mathematical Modelling in Medicine Group, Department of Infection, Immunity and Cardiovascular Disease at the University of Sheffield, which focussed on performing optical measurements to determine strain variation during coronary stent deployment (Zwierzak, 2014). Adopting a stereo photogrammetric approach, landmarks on the stent structure were reconstructed and their 3D geometry accuracy was found in a good agreement with measurements obtained from gold standard technique micro-CT (Cosentino et al., 2014; Zwierzak et al., 2014). Although the limitations of point-wise 3D measurement were, later, overcome by the introduction of DIC, the lack of a dynamic imaging system still needed to be addressed (Zwierzak, 2014). This previous work assessed strain at a smaller scale (~ 10 mm) than the heart dimensions, but suggested the potential of 3D-DIC to provide a robust and effective methodology to characterise strain in the heart with an improved accuracy and spatial resolution, identified as lacking by the wider scientific community (Hokka et al., 2015).

This chapter describes the steps taken within the current project to design a

stereo system focused on dynamic imaging of deformation at the length scale of the heart as well as the procedures developed to reconstruct full-field surface strain fields using 3D-DIC. Finally, a set of experimental and numerical tests are presented to validate the proposed 3D-DIC methodology.

2.2 Stereo cameras calibration

Stereo imaging resembling human binocular vision (*stereopsis*) allows the reconstruction of the 3D geometry of an object given two different views seen from two cameras (Cardenas-Garcia et al., 1995). However, prior knowledge of the camera optical parameters and relative position and orientation is required to establish the relationship between the acquired 2D image views and the 3D object. Such information can be retrieved through a camera calibration procedure, which consists in computing the so-called *intrinsic* and *extrinsic* camera parameters. The former represent optical and geometrical properties of the camera (i.e, the focal length, principal point, scale factor along the vertical and horizontal axes of the image and skew coefficient of the lens); while the latter describe the relative position and orientation of the camera with respect to a world coordinate system. Considering the *pinhole* camera model, which assumes no lens distortions, a 3D point $P(X, Y, Z)$ is related to its 2D projection on the image plane $p(x, y)$ by the following equation:

$$c\tilde{p} = K[R \ t]\tilde{P}$$

$$K = \begin{pmatrix} f_x & s & c_x \\ 0 & f_y & c_y \\ 0 & 0 & 1 \end{pmatrix}, \quad \tilde{p} = [x, y, 1]^T, \quad \tilde{P} = [X, Y, Z, 1]^T, \quad (2.1)$$

where c is a constant (*scale factor*); $[R \ t]$ are the extrinsic parameters, the rotation matrix and translation vector, respectively, which relate the world coordinate system to the camera coordinate system; K represents the intrinsic parameters — c_x and c_y are the coordinates of the principal point (optical centre), f_x and f_y are the focal length in pixels along the x - and y -axis, respectively, and s is the skew coefficient that describes the distortion of the two image axes ($s = 0$ if the image axes are perpendicular).

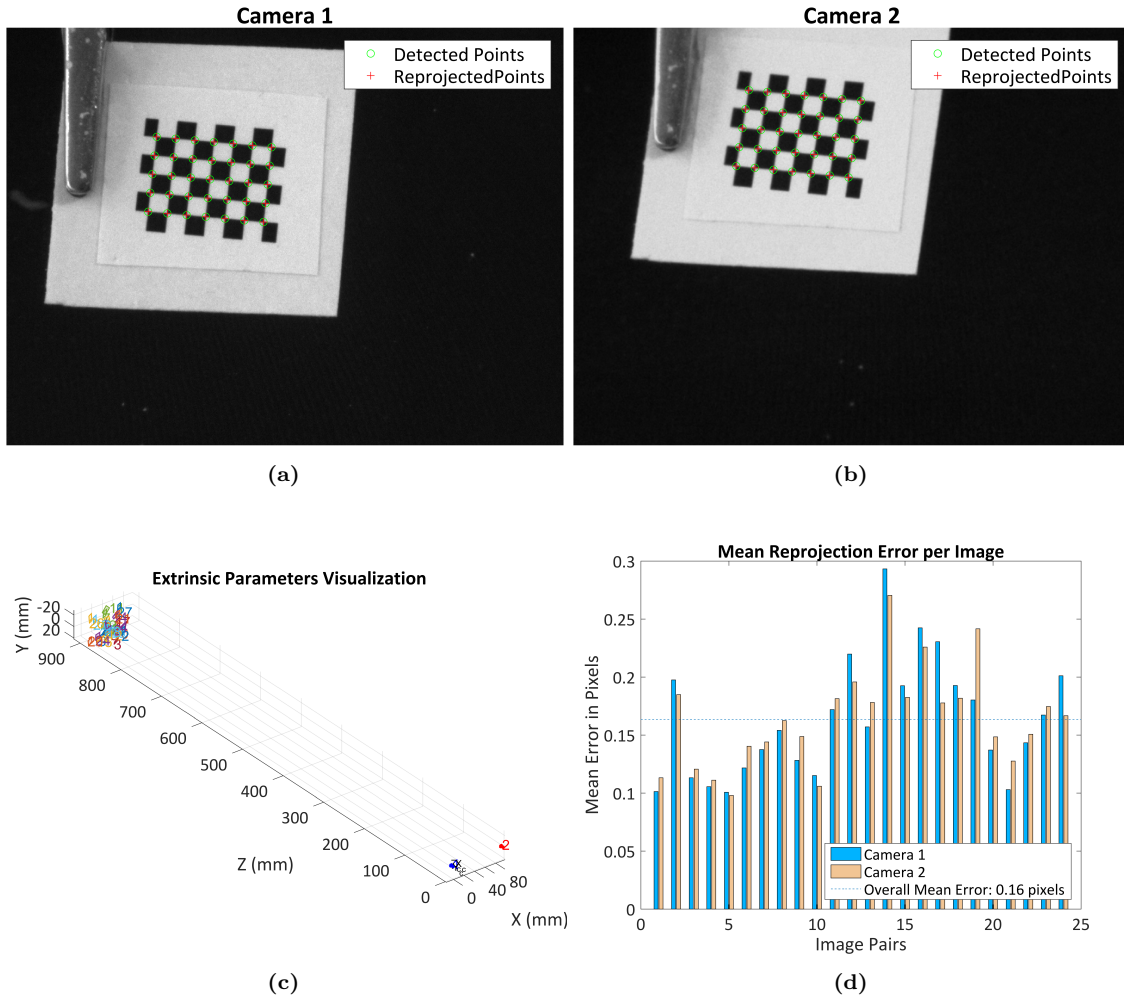


Figure 2.1: Example of an image pair from Camera 1 (a) and Camera 2 (b) showing the checkerboard (2 mm square size) used for the stereo cameras calibration. The green circles represent the position of the corner points extracted initially by the algorithm, while the red crosses represent these points after the projective transformation. (c) 3D visualisation of the location of the calibration pattern in the cameras' coordinate system. (d) Representation of the typical reprojection errors, a qualitative measure of calibration accuracy, obtained in this study.

In this work, stereo cameras calibration was achieved using the Matlab Stereo Camera Calibrator application (Image Processing and Computer Vision Toolbox Release 2015b, The MathWorks, Inc., Natick, Massachusetts, United States), which is built on the works of Heikkila and Silven (1997) and Zhang (2000). This application processes multiple images of a flat checkerboard pattern, with known geometrical dimensions, placed in different positions and orientations (Fig. 2.1c) within the cameras field of view (FOV) and depth of field (DOF), as shown in Fig. 2.1a and 2.1b. The implemented algorithm extracts the corner points of the checkerboard grid and

uses them to compute a projective transformation between the image points of the different images. Afterwards, camera calibration is performed in two steps (Zhang, 2000): firstly, intrinsic and extrinsic parameters are computed using a closed form-solution, assuming that lens distortion is zero; finally, the total reprojection error (Fig. 2.1d), which represents the distance between the reprojected and the detected points in the image, is minimised through a non-linear optimisation method over all the calibration parameters computed and including lens distortion.

2.3 Stereo imaging system

As mentioned earlier, this work extends previous efforts of static measurements of strain in coronary arteries during stent deployment (Zwierzak, 2014) to dynamic measurements of strain in the heart. The fulfilment of such objective requires temporal syncing between the cameras as well as adjusting the optical parameters (i.e., FOV and DOF) to a length scale adequate to obtain high quality images during heart deformation.

Therefore, this section outlines the design of a stereo imaging system to specifically address dynamic imaging at the heart length scale.

2.3.1 Cameras specification and synchronisation

Throughout all the experiments reported in this work, image pairs were captured by a stereo imaging system comprised of two digital charge-coupled device (CCD) cameras (Flea2-13S2, Point Grey Research Inc., Vancouver, BC, Canada), as shown in Fig. 2.2. Specifications of the cameras are reported in Table 2.1.

The two cameras were connected through FireWire cables to the same 1394 bus, in order to be synchronised at the hardware level within $125 \mu\text{s}$, as stated by the manufacturer. While, camera synchronisation at software level was addressed through a graphical user interface (GUI) developed in Matlab, able to control camera



Figure 2.2: Image of the stereo cameras system used in this study.

Table 2.1: Camera specifications.

| | |
|---------------------------|--|
| Sensor Model | ICX445 1/3" |
| Sensor Max Pixels | 1288 × 964 |
| Sensor Pixel Size | 3.75 × 3.75 μm |
| Maximum Frame Rate | 30 fps (two cameras synchronised) |
| Gain | Automatic or Manual (0 to 24 dB) |
| Shutter | Automatic or Manual (0.01 to 33.33 ms at 30 fps) |
| Camera Control | Matlab GUI |
| Cable Connection | IEEE-1934b (FireWire) |
| Dimensions | 29 × 29 × 30 mm |
| Lens Mount | C-mount |

parameters (i.e. image resolution and bit depth, shutter speed, gain and frame rate) and synchronously start camera acquisition. However, due to the bandwidth limit of the FireWire technology, when cameras were synchronised, image resolution and bit depth, at the highest frame rate available (30 fps), were limited to 1024 × 768 pixels and 8-bit, respectively.

2.3.2 Characterisation of the optical parameters

The use of a C-mount system and extension tubes provide flexibility to adjust the camera magnification at the required FOV. Namely, camera magnification (M) is defined as the ratio between the sensor size (S) and FOV ($M = SS/FOV$).

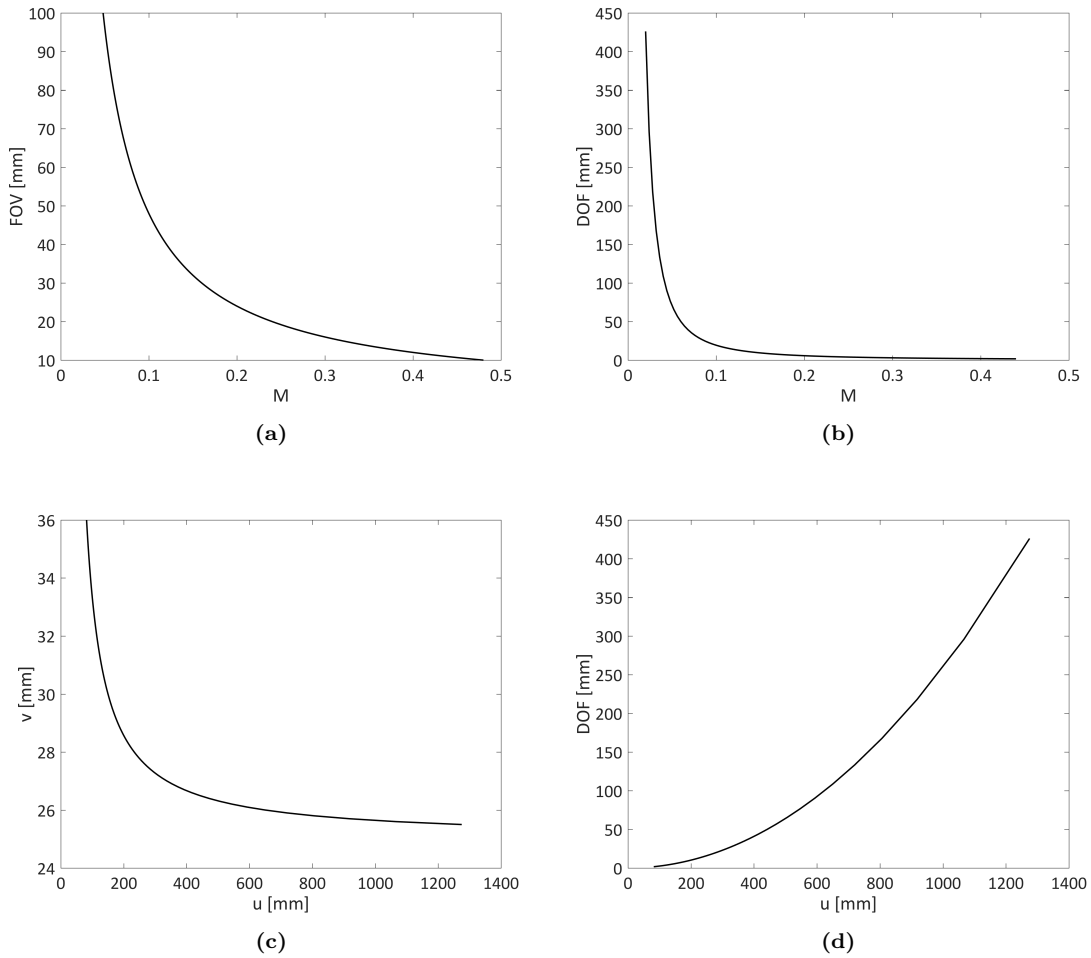


Figure 2.3: Influence of camera magnification M on the resulting FOV (a) and DOF (b). Influence of the object to lens distance u on the lens to sensor distance v (c) and DOF (d). These plots are only valid for the optical parameters and type of cameras used in this study.

Given the sensor size of the camera employed in this work, Fig. 2.3a shows the relationship between the FOV required for the applications of this study (60-100 mm) and camera magnification (M). Moreover, M can be set at the required length scale by adjusting the lens to sensor distance (v) and object to lens distance (u), according to Eq. (2.2) (Jacobson et al., 2000).

In this work, cameras were equipped with planoconvex lenses (10 mm diameter, Comar Optics Ltd, Linton, CB, United Kingdom) with a focal length (f) of 25 mm and an aperture (D) of 2 mm, which, based on the experimental findings in Zwierzak (2014), produced reduced diffraction effects whilst ensuring an adequate DOF. Therefore, given the lens focal length and the magnification needed in this

work, v and u can be determined by solving the system of Eq. (2.2) and the *lens conjugate equation* (Eq. (2.3)). In particular, the relationship between v and u have been reported in Fig. 2.3c.

$$\begin{cases} M = \frac{v}{u} & (2.2) \\ \frac{1}{f} = \frac{1}{u} + \frac{1}{v} & (2.3) \end{cases}$$

Another important parameter to consider in the design of an optical system is the DOF, the distance between the nearest and farthest objects that are perfectly in focus in the image. Particularly, in this study, the DOF needed to be sufficient to guarantee that the heart remained in focus in the image throughout its deformation. The DOF depend on four factors: f , D , u and the sensor size. In fact, it is characterised by the following equation (Jacobson et al., 2000):

$$DOF = \frac{2Ncf^2u^2}{f^4 - N^2c^2u^2} \quad (2.4)$$

where N is called *relative aperture*, which is the focal length divided by the diameter of the entrance pupil ($N = f/D$); c is the *circle of confusion* (typically 0.004 mm for 1/3" image sensors). For the designed optical system in the current work, the influence of magnification M and object to lens distance u on the DOF are illustrated in Fig. 2.3b and 2.3d, respectively.

2.4 3D-DIC methodology

2.4.1 Image matching and 3D reconstruction

After mapping the 3D coordinates of a point in the real world to its corresponding 2D coordinates in the image through the camera calibration procedure, 3D reconstruction requires addressing the *stereo correspondence problem* to match the 2D coordinates of the same points in the two image views and, finally, performing *tri-*

angulation (Hartley and Zisserman, 2004).

Different image matching algorithms have been proposed and used according to the required task (Wang et al., 2015). In particular, *feature-based* algorithms, which extract salient features in the image (e.g., edges or contours) and match them between the stereo views, are widely used in computer vision, in which computational speed is often preferred to accuracy. Whereas, *area (or intensity) -based* algorithms such as digital image correlation (DIC), which correlates the grey levels of image subsets between the stereo views, although more computationally expensive, can provide dense matching maps with sub-pixel accuracy.

Because of the aim of this thesis, DIC was chosen as a matching algorithm to enable full-field measurements of strain in the heart. In particular, by combining DIC with the stereo imaging system described previously (Section 2.3), 3D-DIC was implemented and used throughout the experiments presented in this work. Specifically, the *Ncorr* open-source Matlab program for 2D subset-based DIC was adopted in this study to perform image matching (Blaber et al., 2015), while custom Matlab codes were developed for 3D reconstruction and strain computation. In particular, this program was selected as DIC tool for this study because it offers great flexibility and integration within the Matlab environment allowing convenient post-processing of the data. The algorithms implemented in *Ncorr* are inspired by the works published in Pan (2009); Pan et al. (2010, 2013). Particularly, referring to Section 1.4.1.1, *Ncorr* adopts a first-order shape function, the normalised cross-correlation criterion (NCC) for the displacement initial guess (pixel resolution), the zero-normalised sum of squared differences (ZNSSD) criterion as a cost function to be minimised by the state-of-the-art inverse compositional Gauss-Newton (IC-GN) non-linear optimiser (sub-pixel resolution) and the Reliability Guided (RG-DIC) method and Biquintic B-spline interpolation scheme to reconstruct full-field displacements. Metrics and algorithms implemented in *Ncorr* are summarised in Table. 2.2. The diagram in Fig. 2.4 illustrates the workflow for stereo image correlation and 3D reconstruction

Table 2.2: Algorithms and functions implemented in Ncorr.

| | |
|-----------------------|---|
| Shape Function | First-order |
| Correlation Criteria | NCC (initial guess) and ZNSSD (cost function) |
| Non-linear Optimiser | IG-GN method |
| Interpolation Scheme | Biquintic B-spline |
| Displacement tracking | Reliability Guided DIC (RG-DIC) method |

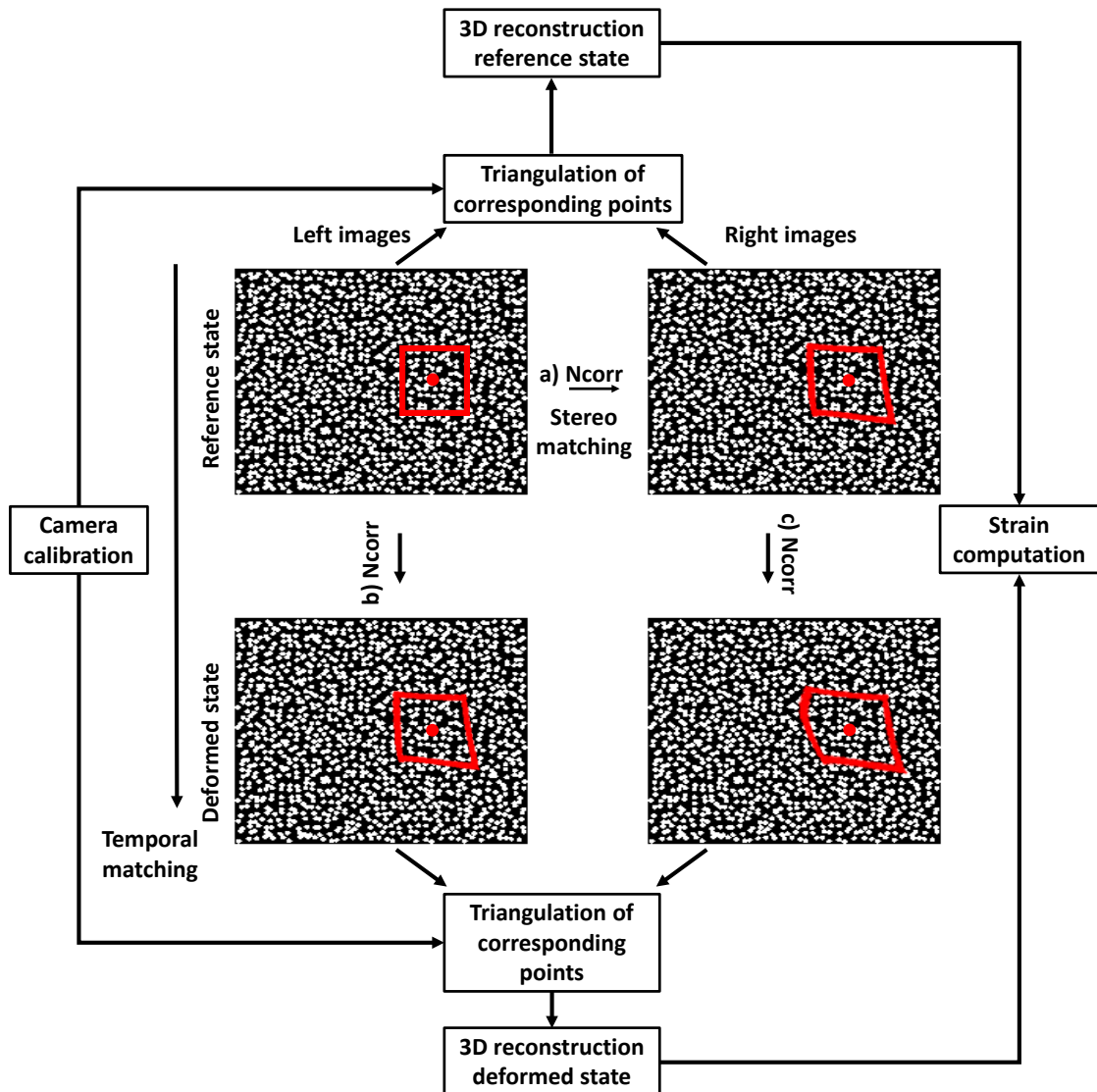


Figure 2.4: Diagram describing the steps implemented in this study to carry out 3D-DIC. First, images of the object with the speckle pattern applied from left and right cameras prior the deformation (reference state) are matched using Ncorr (a). Then, DIC analysis is carried out, separately for the left and right images ((b) and (c)), between the reference and deformed states of the object. At each configuration, the 3D reconstruction of the object surface is achieved using camera calibration data and triangulation of the corresponding points. Finally, strain is obtained by computing the deformations of the elements on the surface meshes respect to their configuration in the reference state, as further discussed in Section 2.4.2.

developed in this work, in which it is possible to identify three main phases:

- *Stereo matching* between the left reference image (L_{t_0}) and right reference image (R_{t_0}), where t_0 corresponds to the un-deformed (reference) state;
- *Temporal matching* separately between the left reference image (L_{t_0}) and deformed images (L_{t_0+i}) and between the right reference image (R_{t_0}) and deformed images (R_{t_0+i}), where i = number of frames;
- *Triangulation* of the corresponding points in the image pairs at each state.

As depicted in Fig. 2.4 (for clarity only a single subset has been represented but the following discussion applies to all the subsets within the region of interest, as DIC provides full-field measurements), the reference subset in the left reference image is matched in the right reference image using Ncorr (step a in Fig. 2.4). This step gives an estimate of the *perspective*¹ displacements between the subsets in the two reference images, which allow a given reference subset of points from the left image to be identified in the right reference image in order to provide left and right 2D coordinates of the correspondence points for subsequent 3D reconstruction. Next, the temporal matching is performed for the left (step b in Fig. 2.4) and right (step c in Fig. 2.4) deformed images, respectively, to track the 2D displacements between the subsets in the reference image and corresponding subsets in the deformed images. Positions of the deformed subsets in the right deformed images are updated at each deformed state considering the initial displacement estimate from the stereo matching (step a). Afterwards, with knowledge of the corresponding points and stereo cameras calibration data, triangulation can be performed to reconstruct the 3D coordinates of the points in the region of interest (ROI). Finally, by computing the difference between the 3D coordinates of the deformed states with those of the reference state, the full-field displacement can be obtained.

¹Perspective here means that it is not a true displacement between the subsets since two images from two different cameras are being correlated.

2.4.2 Strain calculation

As mentioned in Section 1.4.1.1, strain can be easily extracted either from the displacement gradients obtained from the non-linear optimisation (e.g., NR method) or through numerical differentiation of the displacement components. Both these approaches introduce large variation and amplification of the displacement noise in the calculated results, which can be mitigated by the use of smoothing algorithms (Pan et al., 2009b). Although this approach is widely adopted by several researchers in practical DIC measurements, the effect of smoothing and other strategies (e.g., strain window (Sutton et al., 2009)) result in a loss of control on the measured spatial resolution.

Therefore, to preserve the local character of the strain analysis, in this study strain fields were calculated directly from the raw data of the 3D positions in the reference and deformed configurations. The adoption of the strain calculation procedure outlined therein whilst providing slightly noisier strain distributions and outliers, it allows a local characterisation of the cardiac surface strain field preserving the original resolution of the DIC measurement and avoiding loss of information given by the smoothing of existing strain gradients.

In particular, the Green-Lagrange strain tensor was computed based on the approach first proposed by McCulloch et al. (1989) and further investigated by Humphrey (2002) and Genovese et al. (2011a) for biomechanical assessment. Specifically, by defining a connectivity list between the 3D reconstructed points, surface meshes made of triangular elements, whose vertexes are thus defined by the 3D reconstructed points, are generated at each deformed configuration and used in the strain computation. Fig. 2.5 shows an example of a single triangle element from the surface mesh in the reference and deformed states. In detail, the components of the deformation gradient tensor F are calculated locally for each flat triangular domain defined by three control points A , B and C , as shown in Fig. 2.5, by computing how vectors $\Delta V^{(1)} = V_B - V_A$ and $\Delta V^{(2)} = V_C - V_A$ in a reference configuration

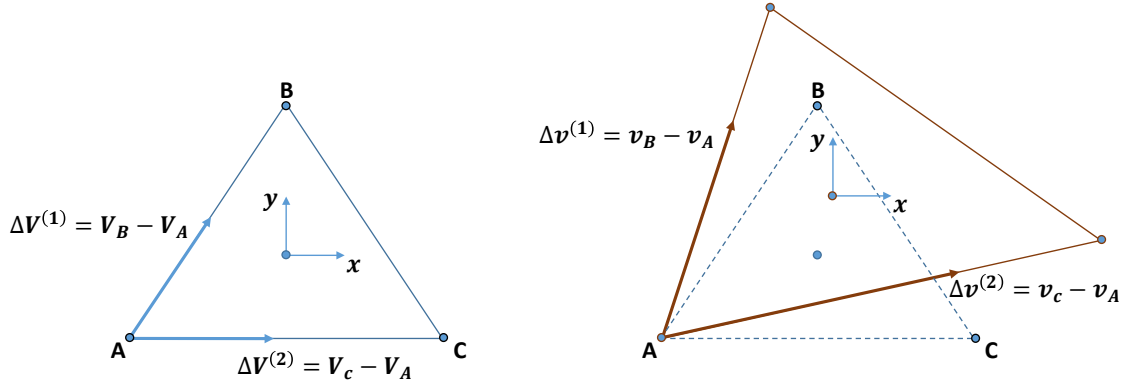


Figure 2.5: An example of a triangular element defined on the mesh of object surface prior (**left**) and after (**right**) the deformation.

(un-deformed state) change to vectors $\Delta v^{(1)} = v_B - v_A$ and $\Delta v^{(2)} = v_C - v_A$ in a deformed configuration of interest. Assuming that each triangular element is sufficiently small, the associated surface deformation is assumed to be homogeneous within it ($\Delta v \approx F \cdot \Delta V$). Accordingly, the four components of the F can be determined by solving the following system of four equations:

$$\begin{bmatrix} \Delta v_x^{(1)} \\ \Delta v_y^{(1)} \end{bmatrix} = \begin{bmatrix} F_x & F_{xy} \\ F_{yx} & F_y \end{bmatrix} \begin{bmatrix} \Delta V_x^{(1)} \\ \Delta V_y^{(1)} \end{bmatrix}, \quad (2.5)$$

$$\begin{bmatrix} \Delta v_x^{(2)} \\ \Delta v_y^{(2)} \end{bmatrix} = \begin{bmatrix} F_x & F_{xy} \\ F_{yx} & F_y \end{bmatrix} \begin{bmatrix} \Delta V_x^{(2)} \\ \Delta V_y^{(2)} \end{bmatrix},$$

where $\Delta V^{(1)}$, $\Delta V^{(2)}$, $\Delta v^{(1)}$ and $\Delta v^{(2)}$ are expressed with respect to a local 2D coordinate system (x, y) with the origin at the centre of the triangular element; while F_x , F_y and $F_{xy, (yx)}$ are the unknown components of the deformation gradient.

The Green-Lagrange strain tensor (E), which is independent of rigid body motion, is obtained from the evaluation of the deformation gradient tensor (F) through the following equation:

$$E = \frac{1}{2}(F^t F - I), \quad (2.6)$$

where I is the identity tensor.

The 2D strain tensor E , being symmetrical, has two components that describe strain along the x - and y -axis (E_x and E_y , respectively) and a shear component ($E_{xy} = E_{yx}$):

$$E = \begin{pmatrix} E_x & E_{xy} \\ E_{yx} & E_y \end{pmatrix} \quad (2.7)$$

To remove the dependency from a coordinate system, the strain tensor E can be expressed in terms of the *principal strain* configuration, which allows strain to be described by two normal components: the maximum and minimum principal strain directions. Given the symmetry of E , an algebraic eigenvalue problem can be solved to determine principal strains and direction of the principal axes. In particular, principal strains are obtained by solving the *characteristic equation* of E :

$$\begin{vmatrix} E_x - \lambda & E_{xy} \\ E_{yx} & E_y - \lambda \end{vmatrix}, \quad (2.8)$$

$$(E_x - \lambda)(E_y - \lambda) - E_{xy}^2 = 0,$$

which gives:

$$\lambda_{1,2} = \frac{E_x + E_y}{2} \pm \sqrt{\left(\frac{E_x - E_y}{2}\right)^2 + E_{xy}^2}, \quad (2.9)$$

where λ_1 and λ_2 are the eigenvalues of E associated with eigenvectors v_1 and v_2 , satisfying:

$$Ev_i = \lambda v_i \quad \text{where } i = 1, 2. \quad (2.10)$$

The eigenvalues λ_1 and λ_2 represent magnitudes of the maximum E_1 and minimum E_2 principal strains, respectively, whose axes are oriented in mutually perpendicular directions defined by the eigenvectors.

2.5 Validation of the developed 3D-DIC methodology

Since its conception (Peters and Ranson, 1982), digital image correlation (DIC) has undergone considerable investigation aimed at improving accuracy and performance. With the advent of high-resolution cameras and development of state-of-the-art matching algorithms, it has been shown that such technique can reach up to 0.01 pixel displacement accuracy and 0.01% strain accuracy (Sutton et al., 2009). However, accuracy, precision and resolution of DIC vary significantly according to the selected hardware, software and experimental conditions. Thus, it is essential for a correct interpretation of the results to provide such metrics for each test. As described in Section 1.4.1.1, DIC encompasses multiple steps: i) the application of a speckle pattern to the specimen surface, ii) the acquisition of consecutive digital images captured before and after the specimen deformation, iii) the image correlation analysis to calculate pixels subsets displacement and, finally, iv) the post-processing of the full-field displacement data to obtain strain distributions. In each of the steps outlined above, error sources can arise and affect the accuracy of DIC. Moreover, the extension to 3D-DIC measurement requires additional steps such as camera calibration and 3D reconstruction whose outcomes can further influence the resulting accuracy.

Accordingly, this section reports a set of experiments aimed at optimising and assessing the accuracy of the developed 3D-DIC system. Specifically, the objectives of these studies were to:

- Generate an effective speckle pattern on the cardiac tissue surface;
- Perform experimental and numerical tests to optimise camera and DIC parameters for the applications of this study;

2.5.1 Speckle pattern application

As already mentioned, DIC usually requires an artificial pattern (*speckle pattern*) to be applied to the object surface to provide distinctive features in the image to enable effective tracking (Sutton et al., 2009). More importantly, the speckle pattern quality strongly affects the success and accuracy of DIC analysis (Lecompte et al., 2006). Nevertheless, ensuring appropriate pattern quality can be very challenging in soft tissues because of their moist and reflective surface. To tackle this problem, Lionello et al. (2014) developed an effective procedure to mark porcine ligaments — firstly, staining the sample with a dark dye and, then, spraying the surface with white speckles (*white on black* speckle pattern). This approach was later used by other researchers to characterise strain in the human tendon (Luyckx et al., 2014) and porcine spine (Palanca et al., 2018) using DIC. Several criteria have been proposed to define the optimal quality of the speckle pattern by assessing, for instance, the morphology of the speckles or the grey-level intensities of the images (Dong and Pan, 2017).

In the next sections, the methods and results of an effective procedure to apply a speckle pattern to the surface of an *in vitro* porcine heart and the assessment of the speckle pattern quality are outlined.

2.5.1.1 Materials and methods

Specimen preparation and stereo imaging A porcine heart was collected from a local slaughterhouse and kept hydrated within a Phosphate Buffered Saline solution until the experiment was started. The heart was dissected along its frontal plane and a slab comprising the three layers of the heart (Section 1.2) was excised. After the dissection procedure, the specimen was prepared for the speckle pattern application. Firstly, methylene blue (Sigma-Aldrich Company Ltd, Dorset, UK) was applied onto the sample surface using a soft-brush to generate a dark background and enhance the contrast of the speckles. Afterwards, an opaque white water-based

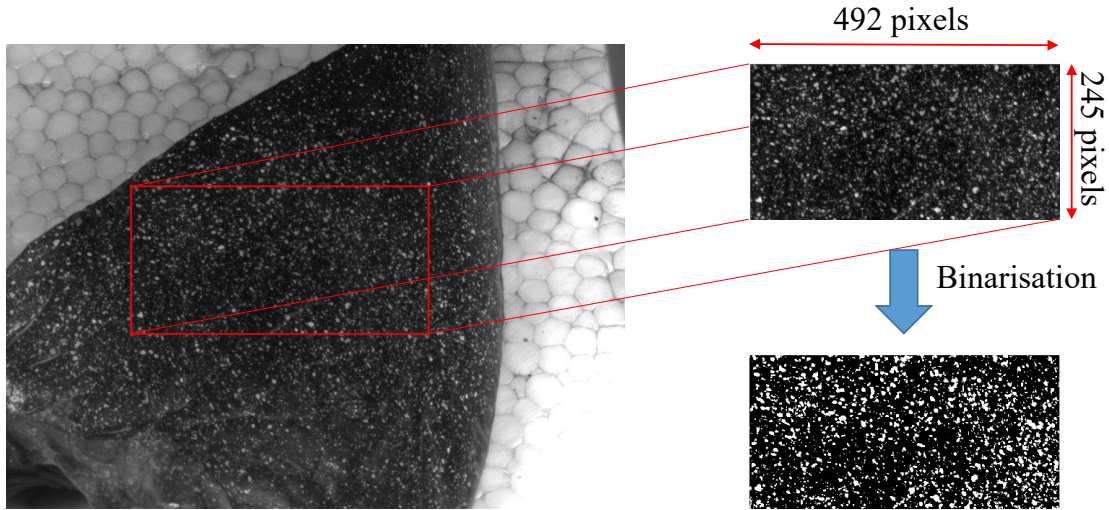


Figure 2.6: Image of the porcine heart surface with the applied speckle pattern and representation of the ROI (red square) selected for the DIC analysis before and after binarisation, performed for morphological analysis of the speckles.

acrylic paint (Com-Art, Anest Iwata-Medea Inc., Portland,OR, US) was sprayed onto the specimen surface with an airbrush operating at 124 kPa, with a 0.3 mm nozzle diameter and 15 cm spraying distance (Iwata Hi-Line HP-CH, Anest Iwata-Mededa, Inc., Portland, OR, US) to create a stochastic distribution of white speckles, as shown in Fig. 2.6. Stereo images of the specimen were captured using the cameras and optics described in Sections 2.3.1 and 2.3.2, respectively. Specifically, camera field of view was roughly 65×50 mm giving an image resolution of $64 \mu\text{m}/\text{pixel}$. Cameras were calibrated using 20 images of a 9×7 square chequerboard (internal square size 2 mm), as illustrated in Section 2.2.

Speckle pattern characterisation The characterisation of the speckle pattern was carried out within the region of interest (ROI) on the cardiac surface selected for the DIC analysis. Namely, a ROI of 492×245 pixels (31×16 mm) was identified in the reference image, as depicted in Fig. 2.6. Firstly, a qualitative analysis of the speckle pattern was achieved exploring the pixel intensities distribution of the sub-image. Subsequently, a quantitative analysis of the speckle patterns was performed investigating the size of the speckles. Two approaches are usually adopted to examine the size of the speckles: the first relies on the computation of the au-

tocorrelation function (Rubin, 2004) and the second consists in the morphological analysis of the speckles (Lecompte et al., 2006). The latter approach was implemented in this work through custom Matlab codes. Namely, the grey-scale image of the speckle pattern was binarised using Otsu's method that provides a threshold that minimises the intraclass variance of the thresholded black and white pixels (Otsu, 1979). Afterwards, the binarised image (Fig. 2.6) was processed using the *imopen* Matlab function, which can be used to recursively dilate and erode binarised images. In detail, the image of the speckle pattern was morphologically opened using disk-shaped structuring elements with different radii ranging between 1 and 7 pixels. Quantitative measurement of the speckles size was achieved by counting the number of white 4-connected pixels present in the binarised image with a radius greater than a specific value (Lecompte et al., 2006).

2.5.1.2 Results

Figure 2.7a illustrates the intensity distribution of the pixel greyscale level in the speckle pattern image ranging between zero and 256 (8-bit digitisation). While, the cumulative percentage of the speckles with a radius belonging to a specific interval is shown in Fig. 2.7b.

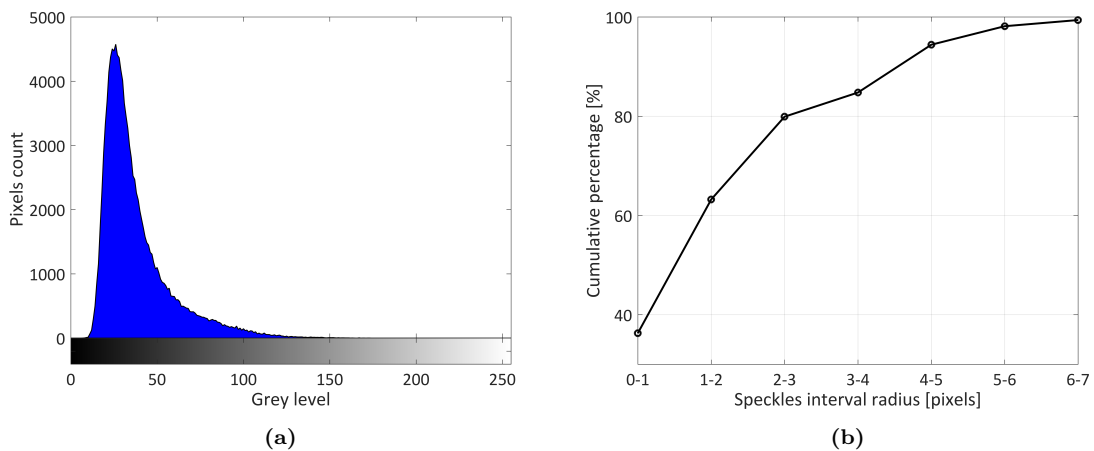


Figure 2.7: (a) Histogram of the grey level intensity of the pixels within the ROI. (b) Cumulative percentage of the speckles with a radius belonging to a specific interval.

2.5.1.3 Discussion

The histogram of the pixels grey level intensities showed the typical distribution of the speckle pattern images used for practical DIC applications, which should be ideally a Gaussian or bell-shaped distribution (Berfield et al., 2007). It is worth noting that the shift towards the left of the histogram reflected the dark background generated to produce a white on black speckle pattern.

The morphological analysis of the speckle size proved that the highest percentage of speckles had a radius lying between 1 and 3 pixels (0.06-0.2 mm), which belonged to the range suggested to avoid aliasing (i.e. 3-5 pixels in diameter) (Sutton et al., 2009).

2.5.2 Optimisation of DIC parameters using experimental and numerical tests

The assessment of baseline errors is an important task in 3D-DIC. In particular the accuracy and resolution of the 3D-DIC analysis strongly relies on the setup preparation (e.g., camera, lighting, camera calibration, stereo angle, etc.) as well as on the DIC settings (e.g., subset size, step size, shape function, etc.). Researchers have widely investigated the metrological performance of 3D-DIC through the use of experimental and numerical studies (Sutton et al., 2009; Bornert et al., 2009; Wang et al., 2011; Ke et al., 2011; Hu et al., 2011; Zhong et al., 2019). For instance, an experimental procedure to estimate error metrics consists in performing the analysis of images of the specimen captured in a zero-strain condition that can be achieved either in a static configuration or during a rigid body motion (RBM) test (Smith et al., 1998; Haddadi and Belhabib, 2008; Genovese et al., 2011a). Whereas, the use of numerical approaches allows specific conditions to be imposed during a test enabling the isolation of potential errors occurring in practical 3D-DIC measurements (Balcaen et al., 2017a,b).

The subset size and step size are the most investigated parameters that significantly affect 3D-DIC outcomes (Robert et al., 2007). In particular, the subset size determines the displacement spatial resolution, while, the step size defines the number of computed points in the image, hence, influences the strain spatial resolution. The choice of the subset size and step size depends on several factors such as the granularity of the pattern (Yaofeng and Pang, 2007; Lava et al., 2009) and the type of deformation measured (i.e. heterogeneous or homogeneous) (Wang et al., 2012). More importantly, despite the use of a large subset size tends to increase the precision, acting as a smoothing filter to the data, this also reduces the spatial resolution of the DIC measurements. Moreover, when performing a 3D-DIC measurement, the choice of the stereo angle greatly impacts the in-depth resolution, with larger stereo angles providing a better precision in the out-of-plane direction (Wang et al., 2011). Conversely, smaller stereo angles improve the in-plane sensitivity and the stereo-matching accuracy since the two views are very similar as they present only slight perspective distortion. Therefore, it is important to consider the optimal DIC parameters that preserve the spatial resolution needed for the specific application whilst reducing noise in relevant output data.

In the next section, the use of experimental and numerical tests is presented to explore the errors arising from the 3D-DIC system developed in this study and to define the optimal parameters to provide accurate, high-resolution measurements of strains in the heart. Specifically, an experimental analysis of the effects of the subset size and step size on the strain errors was carried out during a rigid body motion (RBM) test applied to the heart specimen presented in Section 2.5.1.1. A further benchmark test was undertaken to evaluate the optimal value of the camera shutter speed to capture dynamic images, appropriate for capturing heart deformation. Finally, a numerical approach was developed to impose a controlled strain field to virtual stereo images of the heart specimen and quantify the influence of the subset size and stereo angle on the calculated results.

2.5.2.1 Materials and methods

Experimental tests The heart specimen was rigidly displaced to four different unknown locations within the camera field of view and images were captured at each position. The 3D-DIC methodology illustrated in Section 2.4 was employed to calculate full-field surface strains. Under these conditions, any non-zero components in the strain distribution represent an error. The strain evaluation was carried out at different subset sizes ranging from 17×17 to 47×47 pixels in increments of 6 pixels, while three step sizes were investigated (1, 5 and 9 pixels). The quantitative assessment of the strain errors was achieved by calculating the systematic error (i.e. accuracy) and random error (i.e. precision) of strain values obtained from the 3D-DIC analysis. Accuracy and precision were defined as the average and standard deviation of the strains over the specimen surface in the rigidly translated positions, respectively.

The benchmark test to find the optimal value of shutter speed was carried out by imaging the displacement of a rigid plastic cylinder prepared with the speckle pattern presented in Section 2.5.1.1 and attached to a linear actuator, which simulated the typical displacement and frequency of a beating heart (e.g., Fassina et al. (2017)). The highest frame rate available for the cameras was selected and gain was set in the automatic mode (Section 2.3.1); while dynamic images of the cylinder were taken by varying the shutter speed values at 1, 5 and 33 ms. Under this zero-strain condition, accuracy and precision were computed, as described previously.

Numerical test Starting from the experimental image captured by one of the two cameras of the cardiac tissue with the applied speckle pattern shown in Fig 2.6, two virtual stereo images were created by deforming the experimental image onto the surface of a 3D cylinder using the *imwarp* Matlab function, as illustrated in Fig. 2.8. Then, a pair of deformed stereo images were created using the same process but increasing the initial radius of the cylinder by 10% ($R_{fin} = R_{in} + R_{in} \cdot 10\%$), a

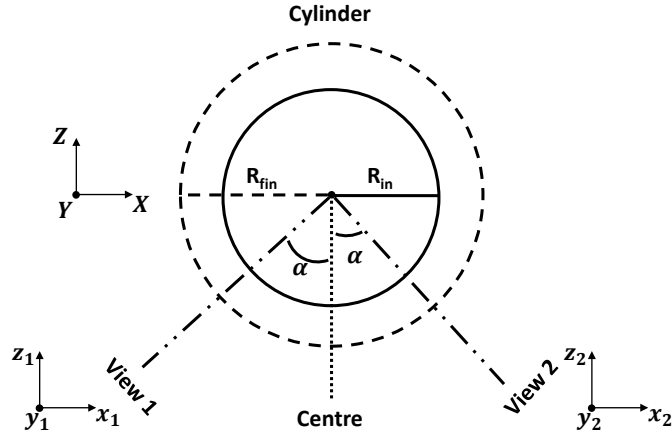


Figure 2.8: Schematic representation of the procedure used to create two virtual stereo images by deforming the image of Fig. 2.6 onto the surface of a cylinder and prescribing geometrical transformation for the two views. Virtual deformed stereo images were, then, generated by increasing the radius of the cylinder.

value representative of the typical strains measured in the epicardial surface. This resulted in a uniform engineering strain ($\varepsilon = 10\%$, see Eq. (1.1)) in the x -direction of the image only since the same y -coordinates were used for both camera views ($y_1 = y_2 = Y$). The DIC analysis between the reference and deformed stereo images was performed with Ncorr and used, along with the prescribed geometry of the stereo rig, to reconstruct the 3D surface of the cylinder in the initial and deformed configurations. Simulating a uni-axial test, the theoretical Green-Lagrange strain E , calculated with the equation $E = 1/2(\lambda^2 - 1)$, where $\lambda = 1 + \varepsilon$, was equal to 10.5%, hence, any deviation from this value represented an error. Specifically, the accuracy (i.e. the average of the strain values) and precision (i.e. the standard deviation of the strain values) over the 3D cylinder surface were computed and investigated whilst changing (i) the stereo angle α (from 15° to 25° in increments of 5°) and (ii) the subset size (from 17×17 to 71×71 pixels in increments of 10 pixels).

2.5.2.2 Results

Experimental tests In both the RBM tests, the average of the absolute values and standard deviation of the maximum principal surface strains obtained in each translated configuration was computed. Afterwards, the median value of these two

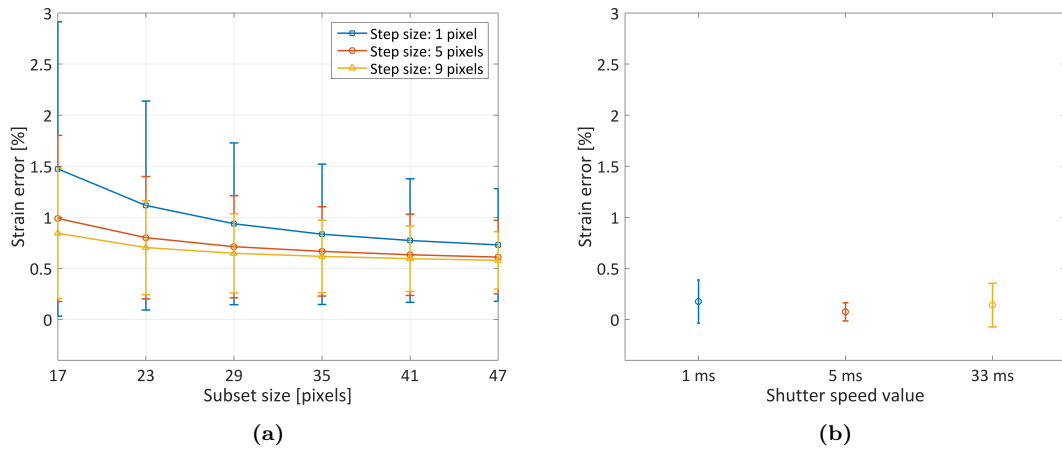


Figure 2.9: Strain errors found following the experimental rigid body motion tests. Influence of the subset size (a) and camera shutter speed value (b) on the accuracy (average of surface strains) and precision (standard deviation of surface strains) of the method.

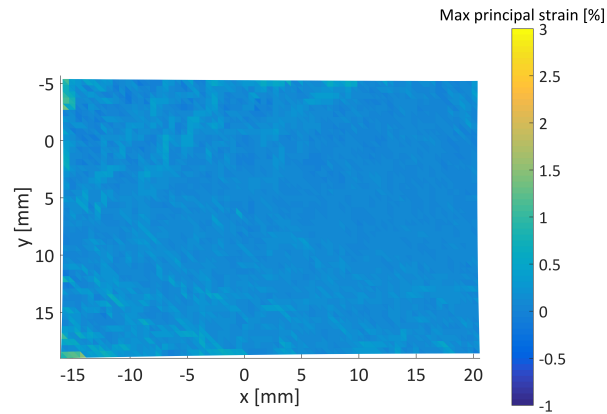


Figure 2.10: Strain error map on the surface specimen in a zero-strain configuration following the experimental RBM test. This map has been obtained with a DIC subset and step size of 33 and 9 pixels, respectively. This resulted in a spatial resolution of approximately 1.5 mm.

quantities over all the different configurations was calculated and reported as a metric of accuracy and precision. In particular, Fig. 2.9a illustrates the influence of the subset size on the strain errors in the heart specimen for the three step sizes considered. While, Fig. 2.9b describes the strain errors introduced when different shutter speed values were investigated in the benchmark test. Fig. 2.10 shows the surface strain map under the zero-strain configuration imposed to the heart specimen obtained with a subset and step size of 33 and 9 pixels, respectively.

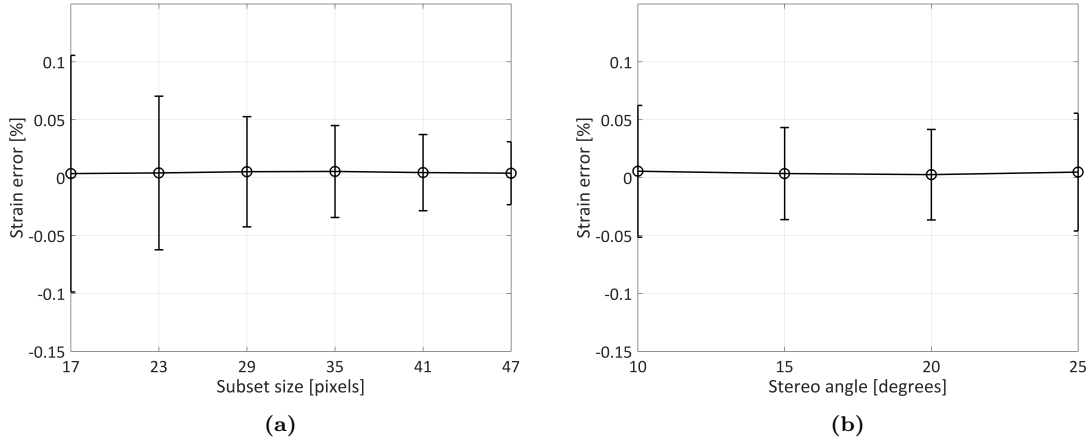


Figure 2.11: Results from the numerical test showing the strain errors obtained after applying a numerical deformation to the virtual stereo images. The errors were computed by subtracting the average of the surface strains measured to the theoretically imposed (i.e. 10.5%). In these tests, the Green-Lagrange strains E (Eq. (2.6)) have been reported. The effect of the subset size **(a)** and stereo angle **(b)** on the resulting strains is reported along with the errorbars indicating the standard deviation of the surface strains.

Numerical tests From the analysis of the virtual deformed stereo images with a stereo angle of 15° , average and standard deviation of the surface strain values found after the numerical deformation were plotted against the different subsets considered, as shown in Fig. 2.11a. Moreover, the effect of stereo angles is reported in Fig. 2.11b, for a 33×33 pixels subset size. In all the tests, the step size was fixed at 9 pixels.

2.5.2.3 Discussion

As shown in Fig. 2.9a, the choice of the subset size greatly affected the precision of the strain measurements. In particular, by varying the subset sizes from 17×17 to 47×47 pixels, precision was improved by approximately 60% in all cases. Whereas, the influence of the subset size on the accuracy was less significant, especially at subset sizes greater than 29×29 pixels. Concerning the strain errors resulting from the analysis with different step sizes, these showed that the step size choice had a minor effect on the accuracy and precision for values greater than 5 pixels, although higher strain errors were found for a step size of 1 pixel. Accordingly,

subsets size ranging between 29×29 and 35×35 pixels and step size of 9 pixels were demonstrated to be the optimal DIC parameters for this specific application ensuring a high spatial resolution (≈ 0.6 mm) and total error (sum of systematic and random errors) less than 1%.

Furthermore, the analysis of the strain errors in the benchmark test, performed with the optimised DIC parameters, showed that a better accuracy and precision was achieved when the shutter speed value was set at 5 ms (Fig. 2.9b). This result could be explained by the lower image quality produced when using the other two shutter speed values. In particular, darker images with a poorer speckle pattern contrast and motion blur were obtained at the smallest and largest values, respectively, which very likely contributed to larger errors in the image correlation and matching.

As shown from the results of the numerical analysis (Fig. 2.11), the subset size and stereo angle did not have a significant impact on the accuracy of the strain results, with values found in good agreement with the numerically imposed strain (10.5%). Whereas, strain precision noticeably varied by changing the subset size, as shown in Fig. 2.11a. Particularly, by increasing the subset from the smallest to the largest size, precision was improved by approximately 70%. Nonetheless, the effect of the stereo angle on the precision was less significant, although smaller errors were observed between 15° and 20° .

The experimental and numerical tests performed in this study demonstrated the relevant role played by the subset size over the other parameters investigated in determining the precision of the DIC measurement. This has been also reported in previous research (Robert et al., 2007; Lava et al., 2009; Wang et al., 2012; Kashfuddoja et al., 2014). Nevertheless, the step size was found to influence both the accuracy and precision at the lowest value investigated, whilst after a certain threshold was found less relevant.

Although the strain errors in the heart specimen surface estimated following the experimental RBM test are acceptable to perform accurate 3D-DIC measurements,

given the typical magnitude of strains ($\approx 10\%$) measured on the epicardial surface (Prinzen et al., 1986; McCulloch et al., 1989; Zhang et al., 2016), it is worth noting that such errors were two orders of magnitude larger than those obtained in the benchmark and numerical tests. This highlights the great influence of the experimental conditions and the challenging nature of applying 3D-DIC in soft tissues, with a complex geometry and material property, such as the cardiac surface.

2.6 Summary

This chapter describes the design and validation of the methodology employed in this thesis to characterise epicardial deformation. In particular, this technique comprises a low-cost and versatile stereo optical system combined with an open-source package for image correlation. After investigating the optical parameters (e.g., magnification, FOV, DOF, etc.) and enabling cameras synchronisation to allow dynamic stereo imaging of the heart deformation, the chapter reports in detail the procedures implemented for stereo image matching and 3D shape reconstruction. Moreover, a local approach to compute full-field deformation is presented, which preserves the spatial resolution of the DIC measurement, defined by subset and step size. Finally, this chapter illustrates a series of experimental and numerical studies to validate the developed 3D-DIC methodology in applications including images of a porcine heart surface prepared with an appropriate speckle pattern. Specifically, these tests determined the optimal DIC settings as well as estimates on the accuracy and precision of this method, which will be used as metrics for the 3D-DIC measurements performed in the experiments reported in Chapters 3-5.

Chapter 3

Application of 3D-DIC to *in vitro* assessment of passive cardiac deformation

This chapter describes the application of the developed 3D-DIC methodology to characterise full-field surface strains in an *in vitro* porcine heart. Specifically, this chapter explores the use of 3D-DIC to analyse strain under dynamic conditions using a passive heart simulator, which replicates controlled heart wall contraction and realistic haemodynamic conditions, extending the static measurements performed in the the previous chapters. The dynamic performance of 3D-DIC was evaluated over several cardiac cycles in a single heart and between multiple hearts. Furthermore, the ability of 3D-DIC to differentiate strain variation with changes in haemodynamic conditions imposed on the same heart was examined.

Part of this chapter has been published in:
P. Ferraiuoli, B. Kappler, S. van Tuijl, M. Stijnen, B. A. de Mol, J. W. Fenner, and A. J. Narracott. Full-field analysis of epicardial strain in an *in vitro* porcine heart platform. *Journal of the Mechanical Behavior of Biomedical Materials*, 91 (November 2018):294-300, mar 2019. ISSN 17516161. doi: 10.1016/j.jmbbm.2018.11.025

3.1 Introduction

Before considering the DIC methodology as a reference technique for the validation of US-2D-STE, a thorough and comprehensive investigation of its metrological performance for cardiac strain imaging (CSI) is required.

The aim of this chapter is to explore the feasibility of using 3D-DIC to map full-field strains on the surface of an *in vitro* haemodynamically loaded porcine heart platform (Leopaldi et al., 2018). Specifically, performance assessment of the 3D-DIC method is carried out to evaluate:

- The repeatability of 3D-DIC strain measurement over multiple cardiac cycles in the same heart and between heart samples;
- The ability of 3D-DIC to differentiate variation of strain following changes in the loading conditions on the heart.

3.2 Materials and methods

3.2.1 Heart harvesting and mounting within the biosimulator platform

Five hearts were obtained from Dutch Landrace pigs. The animals, each weighed about 110 kg, were slaughtered for human consumption. After the pigs were CO₂ stunned, hung and exsanguinated until death, a parasternal incision was made in the thorax and the inner organs removed en-block. After veterinary investigation of the organs, the lung veins and pulmonary artery were harvested, and the aorta was transect under the first supra-aortic vessel. The hearts were then isolated and transported to the laboratory. For a more detailed description of heart preparation, for use in the Cardiac BioSimulator (CBS, LifeTec Group, Eindhoven, NL) see Leopaldi et al. (2018). Briefly, the aorta and left atrium were cannulated and attached to

an external circuit to simulate cardiac circulation, as depicted in Fig. 3.2a. The apex region of the left ventricle was cannulated and connected to a piston pump, which provides pulsatile flow (70 bpm) to the left ventricle using a pulse duplicator system, as shown schematically in Fig. 3.1. The circuit was filled with saline as the working fluid at room temperature. The preload and afterload were adjusted to create a mean preload of 15 mmHg (measured in the left atrium) and an afterload of 80 mmHg (measured in the aorta). The mean cardiac output was set to 3-5 L/min and measured using an ultrasound flow probe (SonoTT™ Clamp-On Transducer, emtec GmbH, Finning, Germany), after the afterload.

3.2.2 Speckle pattern application and stereo-imaging

The placement of the stereo-imaging system is shown in Fig. 3.2a. To enable DIC measurements, a high contrast stochastic white-on-black speckle pattern was created on the epicardium, as described in Section 2.5.1.1. Speckle pattern quality was examined through a morphological analysis of the speckles using the procedure outlined in Section 2.5.1.1. Camera parameters used in the experiments are described in Table 3.1. As described in Section 2.3.2, two synchronised digital CCD cameras (8-bit, Flea2-13S2, Point Grey Research Inc., Vancouver, Canada) equipped with C-mount 25 mm lenses (Comar Optics Ltd, Linton, UK) were arranged in a stereo configuration to capture image pairs during heart deformation (Fig. 3.2a). The cameras were positioned at a distance of approximately 30 cm from the platform. The camera field of view (FOV) was set to image the lateral view of the left ventricle surface, as shown in Fig. 3.2b. Upon completion of each test, cameras were calibrated to retrieve information on their internal and external parameters using the Matlab Stereo Camera Calibrator application and 25 images of a flat chequerboard with 2 mm internal squares placed at different positions and orientation within the cameras FOV, as described previously in Section 2.2.

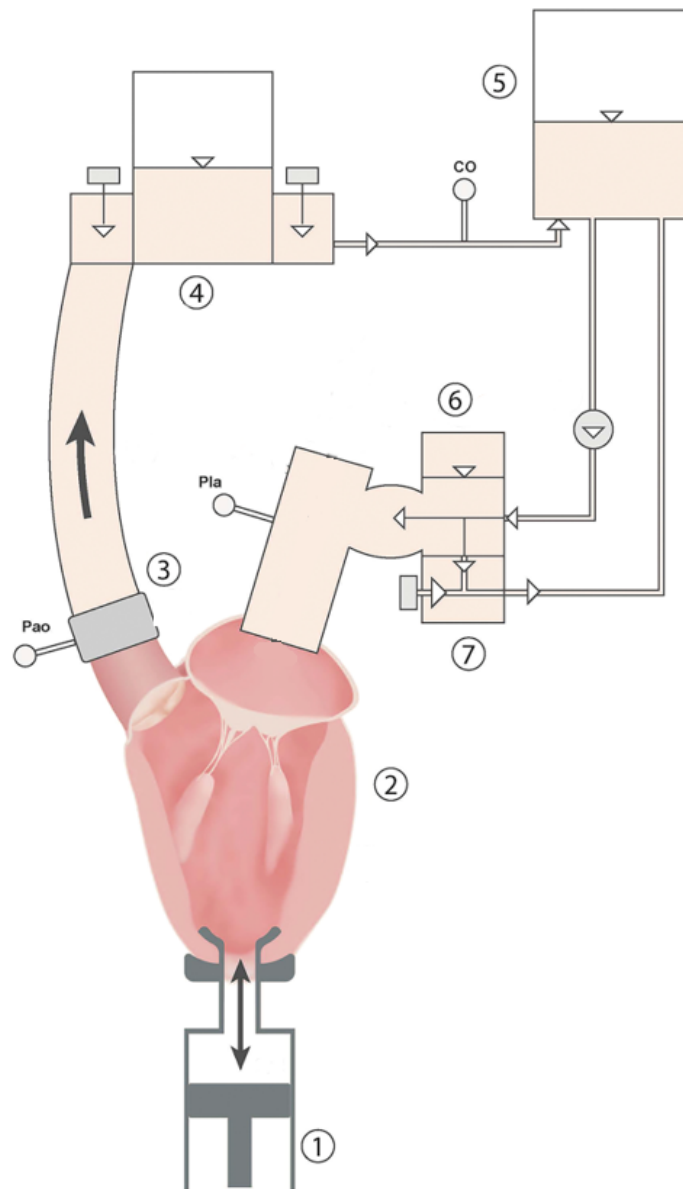


Figure 3.1: Schematic diagram of the dynamic cardiac biosimulator. (1) Pulse duplicator replicating physiologic flow and ventricular pressure attached to the left ventricle chamber. (2) Porcine heart (3) Aortic cannula connected to the ascending aorta. (4) Afterload module. (5) Service reservoir. (6) Preload module. (7) Adjustable Starling resistor to ensure that atrial pressures are maintained at physiologic levels. Adapted with permission from (Leopaldi et al., 2018).

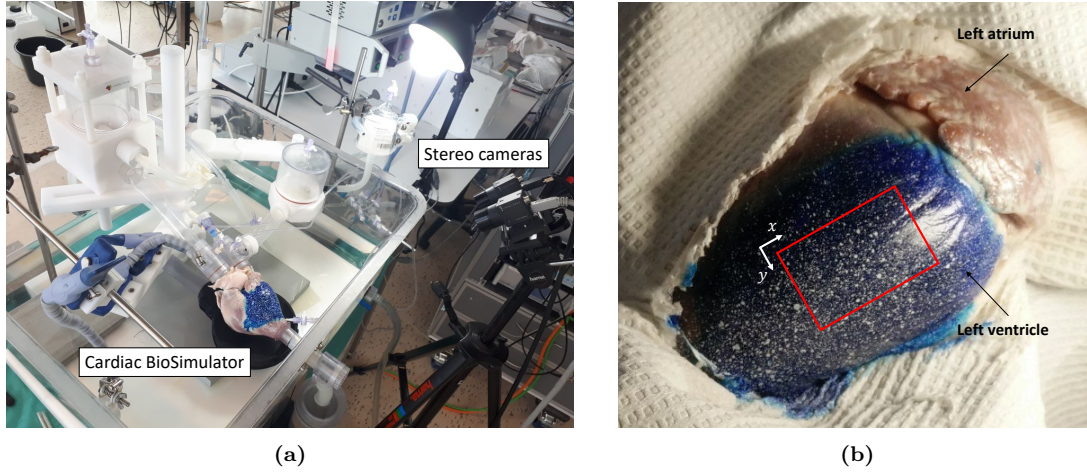


Figure 3.2: (a) Picture of the experimental setup showing the heart with applied speckle pattern within the Cardiac BioSimulator platform and position of the stereo cameras. (b) Close-up of the lateral region of the heart including the left ventricle and atrium overlaid with the region of interest (ROI) used in the 3D-DIC analysis.

Table 3.1: Camera parameters and settings used in the DIC analysis

| Camera parameters | |
|--------------------------|--------------------|
| Camera resolution | 1024 × 768 pixels |
| Lens focal length | 25 mm |
| Image resolution | 0.05 mm/pixels |
| Magnification | 0.07 |
| Frame Rate | 30 FPS |
| Gain | Automatic mode |
| Shutter speed | 5 ms |
| DIC settings | |
| Software | Ncorr |
| Subset size | 33 × 33 pixels |
| Step size | 9 pixels |
| Shape function | First-order |
| Interpolation | Biquintic B-spline |

3.2.3 Digital image correlation and full-field strain calculation

Using the 3D-DIC approach presented in Section 2.4, full-field strain analysis in the rectangular region of interest (ROI) identified in the image of the lateral view of the left ventricle (Fig. 3.2b) was performed. Namely, Ncorr was used to achieve the stereo matching between the corresponding points of the left and right images of the heart at the beginning of the ventricular filling (reference state) (Fig. 3.3, step a). Subsequently, the temporal matching was performed for the left (Fig. 3.3, step b) and right deformed images (Fig. 3.3, step c), respectively, to track the 2D disparity of the corresponding points during the heart deformation. As illustrated in Section 2.4, the 3D reconstruction of the heart was achieved in the reference and deformed states and, finally, magnitude and direction of the maximum (E_1) and minimum (E_2) principal strains on the epicardial surface were calculated, as described Section in 2.4.2, between the reference (i.e. lowest ventricular volume) and deformed states along multiple cardiac cycles.

3.2.4 Evaluation of strain variation in the unloaded configuration

Strain errors were investigated by running a 3D-DIC analysis between images of the heart captured at the beginning of ventricular filling (reference state). The deviation from zero in the strain results was used to assess the variation in strain between each unloaded configuration of the heart, reported as the average (i.e. systematic error) and standard deviation (i.e. random error) of the maximum and minimum principal strains, respectively, in each heart.

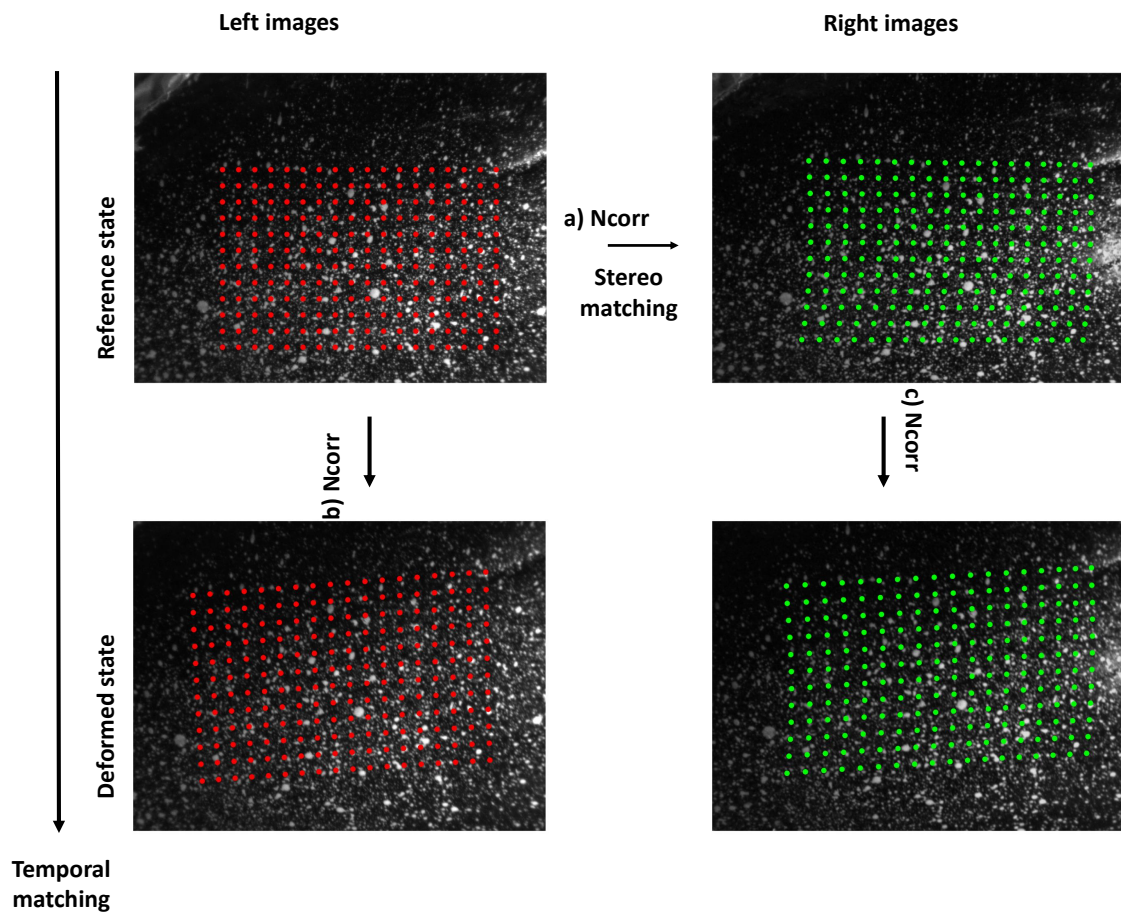


Figure 3.3: . The corresponding points in the left (red dots) and right (green dots) images of the reference state of the heart were matched (a). Afterwards, the displacement of the corresponding points in the images of the deformed states of the heart for the left (b) and right (c) images, respectively, was computed.

3.2.5 3D-DIC repeatability and strain variation assessment

The repeatability of 3D-DIC measurements was quantified between multiple cardiac cycles across the five hearts tested. The intraclass correlation coefficient (ICC) was used to determine the reliability of the strain measurements (Pettersen et al., 2017). Based on a two-way random effect model (Koo and Li, 2016), the assessment of 3D-DIC repeatability was performed by comparing the variability of different strain measurements within the same heart to the overall variation across all the measurements and all the five hearts. Specifically, ICC was computed between the average values of the maximum and minimum principal strains, respectively, at the highest ventricular volume states for each individual heart in the different cardiac cycles. With a confidence interval (CI) of 95%, an ICC value lower than 0.5, between 0.5 and 0.75, between 0.75 and 0.9, and greater than 0.9 indicates a poor, moderate, good and excellent reliability, respectively (Koo and Li, 2016).

To assess the ability of 3D-DIC to differentiate haemodynamic states, loading conditions in one heart (Heart V) were modified, simulating a hypotensive state (Leopardi et al., 2015), and compared with the normal state.

3.3 Results

The 3D-DIC analysis was successfully accomplished in all the hearts over a region of the left ventricle surface to measure epicardial deformations. However, the reconstructed ROIs were slightly different between hearts because of changes in the anatomical structures and positioning within the cameras FOV. In particular, average wall thickness at the middle of the ventricle, measured with a ruler upon termination of the experiments and dissecting the hearts, varied from 11 to 17 mm.

Speckle size characterisation achieved through the morphological analysis showed that the speckles had a size of 4 ± 1 pixels, which belonged to the range recommended to avoid aliasing (Sutton et al., 2009). While, mean reprojection errors, a

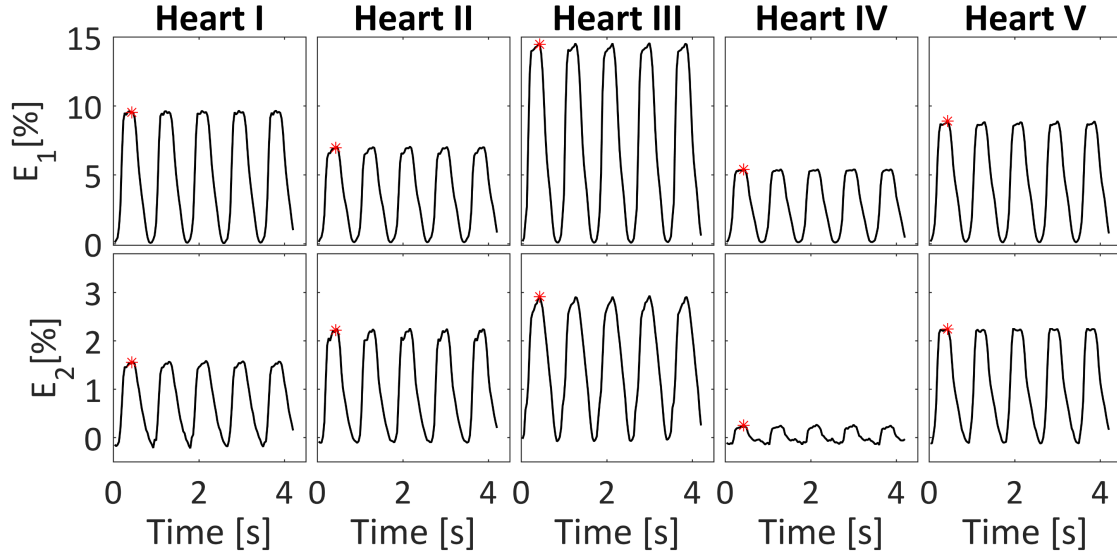


Figure 3.4: Average of the maximum (E_1) and minimum (E_2) principal strain distributions over the reconstructed cardiac surface over multiple cardiac cycles in each heart. The asterisks denote the time point at which strain colour map is reported in Fig. 3.5.

qualitative measure of camera calibration accuracy, were typically 0.3 pixels (0.015 mm) across the experiments.

The strain errors obtained between the five consecutive reference states of the heart (i.e. unloaded configuration) were less than 0.2% in all cases. The median value and range of the average and standard deviation of the surface strain errors in the five hearts are reported in Table 3.2.

The repeatability assessment reported here was performed under the measured haemodynamic parameters reported in Table 3.3.

These were selected for each heart to be within a physiological range. 3D-DIC

Table 3.2: Summary of the systematic (average) and random (standard deviation) zero-strain error over the reconstructed ROIs for the maximum (E_1) and minimum (E_2) principal strain. For each heart, the average and standard deviation of the strain values obtained between three undeformed images of the heart were calculated. The median and range of the strain values over all five hearts are reported.

| | Systematic errors median (min-max) [%] | Random errors median (min-max) [%] |
|-------|---|---------------------------------------|
| E_1 | 0.14 (0.08-0.16) | 0.12 (0.10-0.15) |
| E_2 | 0.09 (0.08-0.12) | 0.09 (0.09-0.13) |

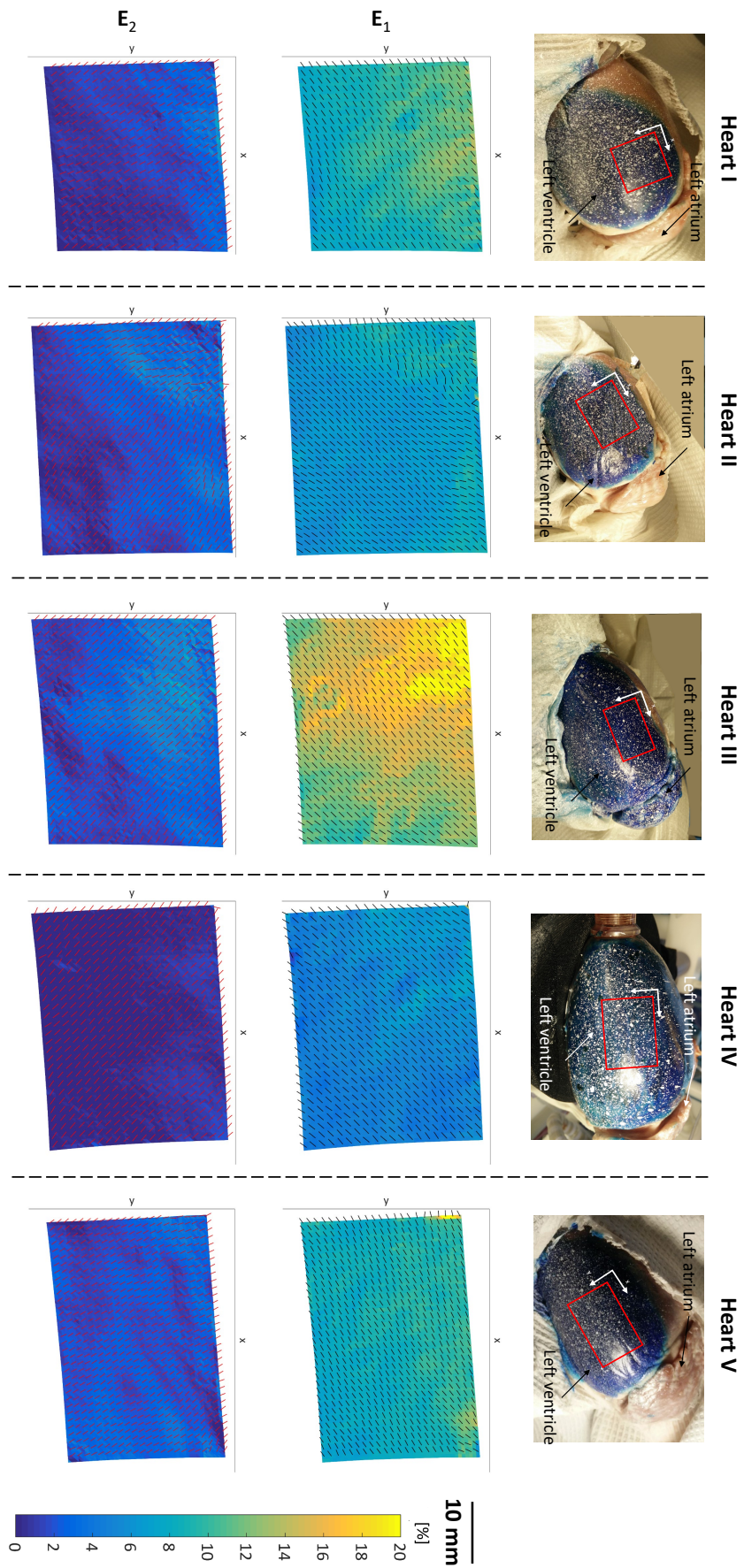


Figure 3.5: The five hearts with the approximate location of the ROIs (red rectangle) identified on the left ventricles for the 3D-DIC measurements (upper pane). Strain colour map and directions of maximum (E_1 , middle pane) and minimum (E_2 , lower pane) principal strain on the reconstructed ROIs at the largest ventricular volume state indicated by the asterisk in Fig. 3.4. The reconstructed surfaces are seen in the xy-plane.

Table 3.3: Measured haemodynamic and epicardial principal strain values (E_1 and E_2) strain at the end of the highest ventricular volume. For each measurement, the mean and standard deviation for five different heart cycles are given.

| | Heart I | Heart II | Heart III | Heart IV | Heart V | |
|--------------------------------|---------------|---------------|----------------|---------------|---------------|---------------|
| Haemodynamics | | | | | Normal | Reduced |
| Minimum aortic pressure [mmHg] | 50 | 55 | 44 | 40 | 45 | 37 |
| Maximum aortic pressure [mmHg] | 109 | 112 | 115 | 109 | 118 | 82 |
| Mean aortic pressure [mmHg] | 77 | 82 | 76 | 71 | 79 | 57 |
| Cardiac output [L/min] | 3.4 | 3.5 | 4.2 | 4.2 | 4.5 | 2.7 |
| Epicardial strains | | | | | | |
| Mesh triangular elements | 3780 | 6100 | 4730 | 4510 | 6120 | 6120 |
| E_1 [%] (Mean \pm SD) | 9.5 \pm 1.5 | 7.0 \pm 1.0 | 14.1 \pm 2.5 | 5.4 \pm 0.9 | 8.7 \pm 1.1 | 6.2 \pm 0.1 |
| E_2 [%] (Mean \pm SD) | 1.6 \pm 1.0 | 2.2 \pm 1.2 | 2.8 \pm 1.4 | 0.2 \pm 0.6 | 2.2 \pm 0.7 | 1.5 \pm 0.0 |

repeatability assessment was described both quantitatively through the ICC and qualitatively by plotting the average of principal strain surface values over the cardiac cycles, as shown in Fig. 3.4. The ICC showed an excellent repeatability of 3D-DIC in assessing strains with values of 0.99 for a CI of 95% in both E_1 and E_2 . As shown in Fig. 3.4, the frequency of the temporal strain variation in each heart was very similar to the heart rate applied to the pump (70 bpm). Starting from near zero, average strains increased in magnitude as the ventricle expanded and returned to zero at end of the cardiac cycle. The number of mesh triangular elements used in the strain computation shown in Fig. 3.4 at the highest ventricular volume state in all the five hearts are reported in Table 3.3. The number of triangular domains varied between hearts because of the different size of the reconstructed ROI on the epicardial surface. Overall, the area of each triangular facet was approximately 0.15 mm².

The maximum principal strain direction represents the direction of the greatest stretching of the cardiac surface at the highest ventricular volume and is shown in Fig. 3.5, along with the minimum principal strain directions, orthogonal to the maximum principal strain directions. Specifically, Fig. 3.5 shows the surface strain maps and directions of E_1 and E_2 in the reconstructed ROIs, schematically depicted in the image of the hearts, at the highest ventricular volume.

Fig. 3.6 illustrates the behaviour of the aortic pressure and cardiac output for the two loading conditions (reduced and normal) imposed on Heart V to investigate

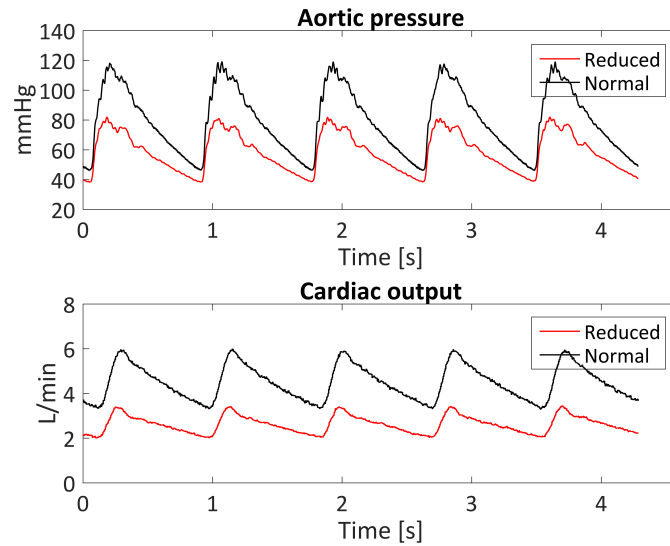


Figure 3.6: Haemodynamic variations recorded for the aortic pressure (**upper pane**) and cardiac output (**bottom pane**) between the Reduced and Normal conditions.

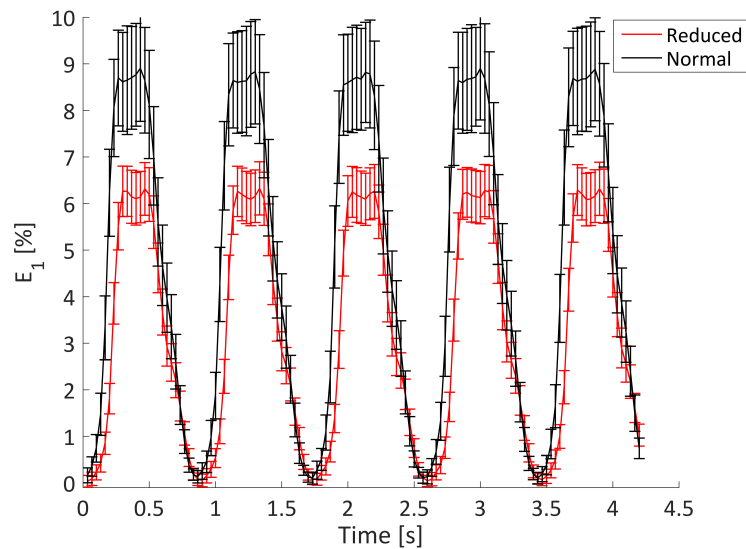


Figure 3.7: Comparison between the maximum principal strain (E_1) distributions under two different haemodynamic scenarios imposed on the same heart (Heart V). Mean aortic pressure for Normal and Reduced were 79 and 57 mmHg, respectively. Mean strain value is shown as a solid line, error bars show the standard deviation over the ROI on the cardiac surface at each time point.

the ability of 3D-DIC to differentiate different haemodynamic conditions. Haemodynamic values for the reduced condition are also reported in Table 3.3. The strain distribution in the same heart under reduced (hypotensive) and normal loading conditions are illustrated in Fig. 3.7, showing variation in peak strain between the two states of around 2.5%.

3.4 Discussion

This chapter shows that 3D-DIC was able to analyse epicardial strains in a dynamic heart model. Specifically, the feasibility of performing repeatable and accurate 3D-DIC based strain measurements over multiple cardiac cycles in several hearts was demonstrated. The use of an *in vitro* cardiac biosimulator platform was shown to be effective for precise, controlled and standardised ventricular deformation to assess the repeatability of strain measurements made on the soft tissue surface, allowing possible errors in the 3D-DIC measurements to be identified. The 3D-DIC analysis was successfully achieved for all the tests as a result of adequate speckle pattern creation on the cardiac surface. In particular, the coating of the epicardium with methylene blue greatly enhanced the contrast of the white speckles and partially reduced specular reflections, a common problem experienced in the optical imaging of curved objects such as the cardiac surface.

Strain evaluation, performed in the five different hearts, was undertaken while simulating realistic physiological cardiac output and aortic pressure values (Leopaldi et al., 2015, 2018). Reported strain measures were consistent and highly repeatable over cardiac cycles and hearts (ICC = 0.99). The subset size selected in the DIC analysis was responsible for the spatial resolution of the measurement (≈ 1.5 mm), while the step size defined the number of data points in the 3D reconstructed meshes and triangles sides (≈ 0.5 mm).

Considerable variations were observed in peak strain magnitude between hearts,

as illustrated in Table 3.3, because of the inherent difference in heart size and ventricular wall thickness. Variation in heart size and wall thickness have been shown to influence the magnitude of epicardial deformations as reported by McCulloch et al. (1989). The direction of the principal strains was in good agreement over all hearts at the end of ventricular filling, as depicted in Fig. 3.5. At low ventricular volume, principal strain directions (not reported here for brevity) showed a highly scattered distribution, whereas with ventricular filling the principal directions assumed a consistent pattern. In particular, the maximum principal strain was typically aligned close to the longitudinal axis of the heart at higher ventricular volumes, while second principal strain in the circumferential direction. Such behaviour has been observed in previous research (McCulloch et al., 1989), in which the authors demonstrated that during passive ventricular filling maximum extensions become more longitudinal due to muscle fibre orientations. The difference in magnitude between first and second principal strains observed in this work reflects the complex behaviour represented in continuum mechanics models of ventricular filling that assume the passive myocardium to be an anisotropic material affected by the muscle fibre orientation (Gültekin et al., 2016).

Overall, average strain distributions in each heart demonstrated similar time varying form of amplitude and frequency with values at the end of the cardiac cycle very close to zero. These results encourage the use of 3D-DIC to quantify residual tracking errors of 2D-ultrasound-speckle tracking echocardiography (2D-US-STE) that have been shown to accumulate over each heart beat (Pettersen et al., 2017). 3D-DIC clearly detected variability in strain distribution between two different haemodynamic scenarios imposed on the same heart, with strain variation larger than the estimated error of the system. Although in this case strain differences reflected changes in the loading condition, the ability to resolve different deformation states of the heart can be used to indicate myocardial dysfunction by measuring the reduction in peak systolic strain (Smiseth et al., 2015). However, in order to

accurately detect abnormal strain, a robust and reproducible method is required. Therefore, results reported in this chapter promote the use of 3D-DIC to investigate the reliability of clinical imaging modalities such as 2D-US-STE in distinguishing subtle strain variations.

Biplane optical techniques have been already examined to study epicardial deformations. Recently, Zhang et al. (2016) presented an optical method to map simultaneously epicardial contraction and membrane potential in beating hearts to study the electromechanical coupling mechanisms. Furthermore, McCulloch et al. (1989) assessed regional variation of epicardial deformations in the passive heart revealing the anisotropic nature of the cardiac muscle with respect to the muscle fibre directions. However, in these studies, tracking of heart motion was accomplished measuring the displacement of fiducial markers attached to the epicardium that limited the spatial resolution measurement to the number of markers and distance between them (~ 10 mm). Whereas, in this chapter, epicardial deformations were retrieved tracking the displacements of the applied speckles which deformed with the underlying tissues to provide a more accurate strain measurement and a higher spatial resolution.

However, some limitations associated with the 3D-DIC method and the experimental platform should be considered in the interpretation of these results. Although an optimisation of the DIC parameters was undertaken to find a compromise between strain uncertainties and a good spatial resolution, as discussed in Chapter 2, 3D-DIC strain results may be affected by other parameters related to both the stereo-optical system (e.g., lens characteristics, image resolution, stereo-angle, and cameras calibration accuracy) and the DIC process (e.g., shape function, correlation criteria and interpolation scheme). Furthermore, synchronisation between camera acquisition and measurements of ventricular volume and pressure change were not available in this study. Thus, the reference image used in the 3D-DIC analysis was determined by identifying the state associated with the lowest ventricular volume

of the heart. Moreover, although the CBS platform replicates physiologically relevant haemodynamic conditions, as the heart is passively distended by an external pump connected to the apex, the ventricular mechanics were not directly comparable with that in a beating heart, which includes three-dimensional dynamic myocardial contraction and ventricular twisting.

3.5 Summary

In this chapter, an experimental framework combining a highly controlled *in vitro* porcine heart model and the 3D-DIC optical technique has been developed to perform a full-field dynamic analysis of epicardial strain. Highly repeatable and accurate 3D-DIC measurements were obtained over multiple cardiac cycles and different hearts. Most importantly, non-contact measurements were obtained with a higher spatial resolution than other optical techniques allowing resolution of local variations in strain on the epicardial surface. Moreover, the application of 3D-DIC enables the collection of highly dense set of data, which may be used to inform mathematical and computational modelling of the heart. Outcomes from this study demonstrate that the CBS platform can act as a controlled model of the heart in which to carry out simultaneous measures of cardiac deformations for direct comparison between 3D-DIC and US-2D-STE, as presented in Chapter 4.

Chapter 4

Measurement of *in vitro* cardiac deformation using both 3D-DIC and US-2D-STE

This chapter describes the combined use of 3D-DIC and US-2D-STE in the Cardiac BioSimulator (CBS, section 3.2.1). The coupling of these two techniques in the CBS allows the evaluation of their performance under controlled experimental conditions isolating error sources related to each method. Specifically, this chapter reports a quantitative assessment and comparison of the optical and ultrasound-based methods in determining displacement and strain in the heart.

Part of this chapter has been included in:
P. Ferraiuoli, L. S. Fixsen, B. Kappler, R. G. P. Lopata, J. W. Fenner, and A. J. Narracott. Measurement of *in vitro* cardiac deformation by means of 3D digital image correlation and ultrasound 2D speckle-tracking echocardiography. *Medical Engineering & Physics*, 74:146–152, dec 2019a. ISSN 13504533. doi: 10.1016/j.medengphy.2019.09.021

4.1 Introduction

As discussed in previous chapters, unlike many clinical imaging techniques (i.e. MRI, radiography and US) which can create an image of internal body structures, as 3D-DIC is an optical method it is limited to surface measurements and cannot be used for non-invasive imaging of the heart. However, as demonstrated in Chapter 3, 3D-DIC can be used as a high quality reference for evaluating full-field strain distributions in the heart during *in vitro* experiments. Moreover, *in vitro* models such as the CBS allow specific haemodynamic conditions to be imposed on the heart and reproducible deformations of the LV.

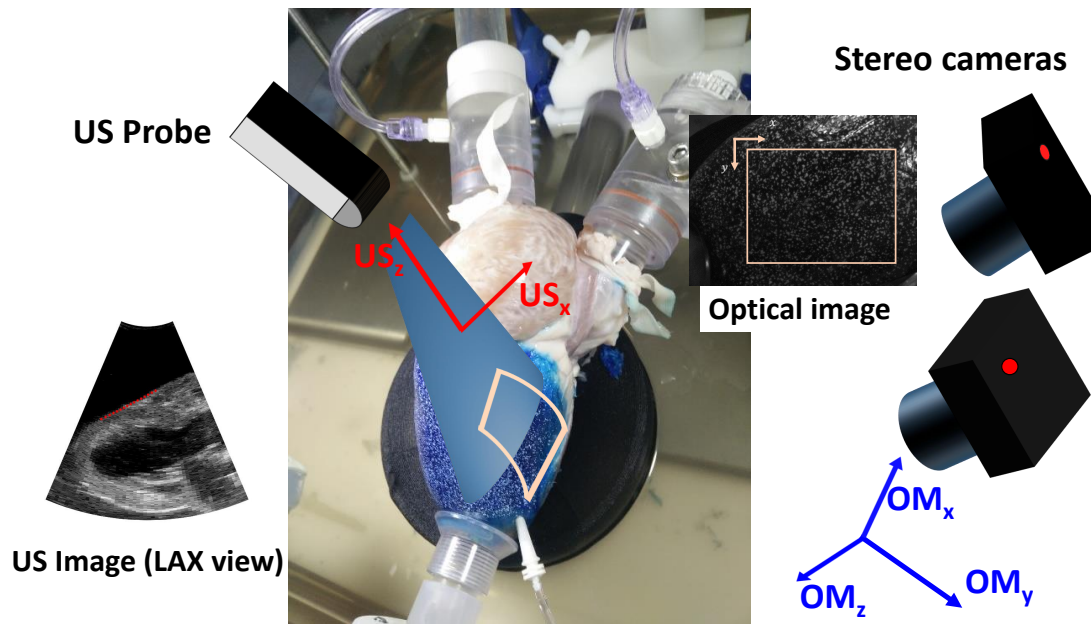
In Chapter 3, the feasibility of applying 3D-DIC to an *in vitro* model of the heart was explored and the results showed highly repeatable measurements of high-resolution strain on the epicardial surface as well as error metrics under a zero-strain state of the heart. Furthermore, the control of the CBS platform ensured that heart deformations were consistent throughout the experiment providing suitable conditions for carrying out comparisons between imaging modalities.

The aim of the current chapter is to assess and compare 3D-DIC and US-2D-STE in the analysis of displacement and strain in the CBS platform. This study was a collaborative effort with contributions from members of the VPH-CaSE Marie Curie Initial Training Network at TU/e and LifeTec Group.

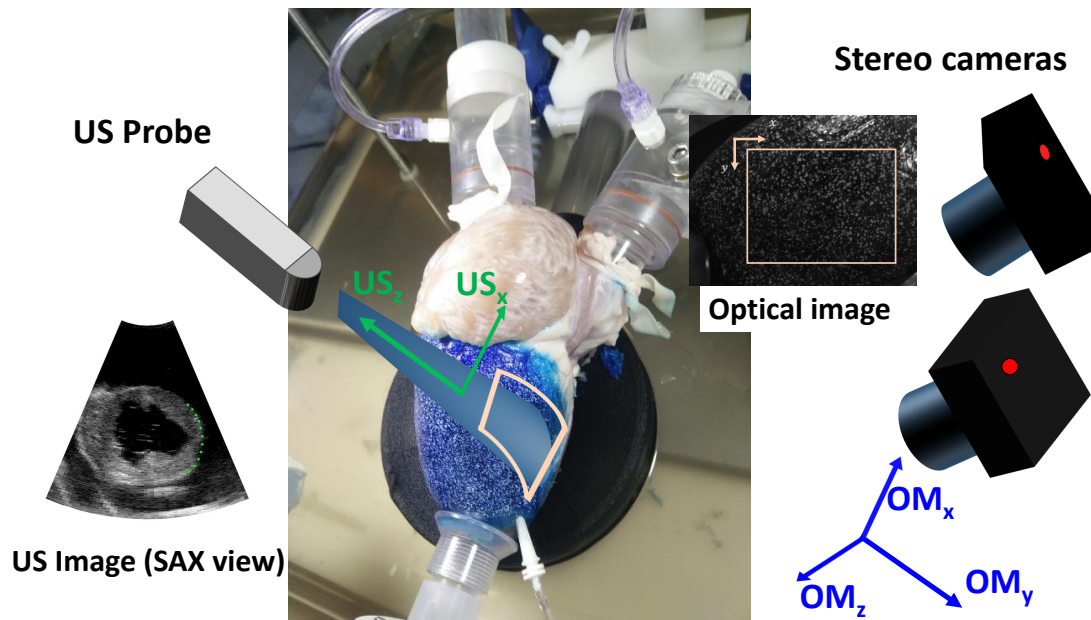
4.2 Materials and methods

4.2.1 Platform preparation

The CBS platform was prepared following the same procedure described in Chapter 3 and Leopaldi et al. (2018). Four porcine hearts were used for *in vitro* testing. Two different dynamic loading conditions were applied to the heart to reproduce a normotensive (NT) haemodynamic condition (mean atrial pressure and mean aortic



(a)



(b)

Figure 4.1: Schematic representation of the experimental setup. The figure shows roughly the position and orientation of the US probe coordinate system, for the LAX (a) and SAX views (b), along with the stereo cameras coordinate system with respect to the heart. Examples of the corresponding B-mode and optical images acquired by the two methods are shown on the left and right, respectively. The US beam and the ROI selected for the 3D-DIC analysis are overlaid on the heart surface to show the approximate region of overlap between the two techniques.

pressure of 15 mmHg and 100 mmHg, respectively) and a hypertensive condition (HT) (mean atrial pressure and mean aortic pressure of 15 mmHg and 130 mmHg, respectively) (Leopaldi et al., 2015).

To compare 3D-DIC and US-2D-STE, the experimental protocol was designed to accommodate the requirements of the two techniques and improve their image quality. Specifically, the heart was placed on a soft support within a tank, which was filled with saline solution to submerge the heart when US-2D-STE was performed. Whereas, when 3D-DIC was carried out, the tank was drained and the heart was left in air. Fig. 4.1 shows a schematic representation of the experimental setup.

4.2.2 3D-DIC analysis

Before placing the heart in the platform, an artificial speckle pattern was created on the LV surface and its quality was assessed through a morphological analysis, as previously described in Section 2.5.1.1.

Using the same optical system presented in Section 2.3.2, cameras were arranged in a stereo configuration with a baseline distance of 200 mm and stereo angle of approximately 15° to capture synchronised image pairs at 30 frames per second (fps) of the heart during its deformation. Shutter speed was set at 5 ms to avoid motion blur of the speckles, as suggested from the experiments in Section 2.5.2, whilst this required the use of additional lighting; a white-light LED lamp was used to improve lighting conditions and avoid flickering. The cameras were placed roughly 1 m away from the platform with magnifications adjusted to ensure the whole region of the lateral LV surface was imaged. Upon completion of the experiment, the cameras were calibrated by capturing 20 images of a flat chequerboard made of 2 mm internal squares and using the procedure outlined in Section 2.2. Camera parameters and DIC settings are reported in Table 4.1.

The 3D-DIC methodology, developed in this thesis and reported in Section 2.4, was applied to the region of interest (ROI) on the LV surface, shown in Fig. 4.1,

Table 4.1: Camera parameters and DIC settings.

| Camera parameters | |
|--------------------------|--------------------|
| Camera resolution | 1024 × 768 pixels |
| Lens focal length | 40 mm |
| Image resolution | 0.01 mm/pixels |
| Magnification | 0.05 |
| Frame Rate | 30 fps |
| Gain | Automatic mode |
| Shutter speed | 5 ms |
| DIC settings | |
| Software | Ncorr |
| Subset size | 33 × 33 pixels |
| Step size | 9 pixels |
| Shape function | First-order |
| Interpolation | Biquintic B-spline |

to reconstruct its 3D shape during the heart deformation. From the reconstruction of 3D points on the LV surface, displacement and strain were computed with respect to a reference state corresponding to the maximum loading condition in the LV. By adopting the strain calculation procedure outlined in Section 2.4.2, the Green-Lagrange strain tensor (E) was calculated and, finally, by solving the eigenvalue/eigenvector problem of the local strain tensor, the magnitude and direction of the maximum and minimum principal strains were obtained.

4.2.3 US-2D-STE analysis

US-2D-STE data were acquired using a MyLab70 XVG US system (Esaote, Maastricht, NL) and a curved array transducer (centre frequency of 2.7 MHz and 55° opening angle). An imaging depth of 130 mm was used, resulting in a frame rate of 47 Hz. Radio-frequency (RF) data were acquired at the mid-level of the heart, halfway between the apex and mitral valve, with the papillary muscles visible. Images of the LV were acquired in the cross-sectional short-axis (SAX) and the longitudinal-axis (LAX) view by rotating the probe 90°, as shown in Fig. 4.1a and b, respectively. Data were imported into Matlab for displacement tracking and strain estimation.

The sequences of RF data were first segmented into clips of at least four heart cycles, based on M-mode of the LV centre-line. Displacement tracking was performed using the ‘coarse-to-fine’ algorithm, previously published by Lopata et al. (2009b). The method uses a window of RF data that reduces in size over three iterations. Displacements were estimated in both the axial (in the US beam path) and lateral (across the lines of RF data) directions. Prior to displacement estimation, the endocardial and epicardial borders of the LV were segmented, and a mesh of 11 radial and 91 circumferential coordinates generated covering the segmented region. The mesh was annular in shape for the SAX view and U-shaped in the LAX view. The points of the mesh were tracked based on the obtained displacement field. Start- and end-points of the sequence were shortened to peaks in the surface area. Strain was calculated by taking the spatial derivative of the deformation of the mesh from the initially segmented geometry using a least-squares strain estimator (Lopata et al., 2009a), in the true local directions. Circumferential strain was calculated in the SAX view, longitudinal strain in the LAX view. Radial strain was calculated in both views.

4.2.4 Data analysis and comparison between the two techniques

Before comparing results from the two imaging modalities, a performance assessment of 3D-DIC was undertaken to evaluate its accuracy and repeatability. To preserve camera calibration accuracy and due to constraints imposed by the pump in the platform, the established test to assess strain error (Smith et al., 1998) was not feasible. However, a metric of deviation from anticipated zero strain was estimated by measuring the strain between multiple images of the heart captured in the unloaded configuration.

Comparison of cardiac displacement and strain measurements obtained from 3D-DIC and US-2D-STE was conducted for the NT condition over a single cardiac cycle.

Specifically, from the points identified in the B-mode images on the outer surface of the heart wall, in both the LAX (red dots) and SAX (green dots) views (Fig. 4.1a and b, respectively), lying within the optical reconstructed ROI, the US-2D-STE displacement components were extracted and their average and standard deviation were calculated. The same approach was applied to the displacement values retrieved from the 3D-DIC method. Some assumptions are required relating to the relative configuration of US probe and stereo cameras, as shown in Fig. 4.1. Comparison between the two methods was undertaken by analysing the displacement along the axial direction of the US beam US_z , both in the LAX and SAX views, and the displacement along the y-axis of the left camera OM_y . Furthermore, the median values of the displacement from all four hearts over the first cardiac cycle were calculated and the correlation between 3D-DIC and US-2D-STE, for the two views, was evaluated. Concerning the strain measurements, average and standard deviation were computed for both the maximum and minimum principal strains over the ROI reconstructed with 3D-DIC and the longitudinal and circumferential strains derived from US-2D-STE in the LAX and SAX views, respectively.

4.3 Results

From the morphological analysis of the speckle pattern it was observed that most of the speckles (roughly 70%) had a size of 4 ± 1 pixels, while mean reprojection errors, from camera calibration, were typically 0.16 pixels (0.016 mm) across the experiments.

Fig. 4.2 illustrates a dynamic representation of the 3D displacement components of the four hearts obtained from 3D-DIC at the NT (solid lines) and HT (dashed lines) conditions, which are shown in Fig. 4.3a and 4.3b, respectively. Specifically, the plot in Fig. 4.2 shows the average of each displacement component (x, y and z) within the ROI on the epicardial surface along four cardiac cycles.

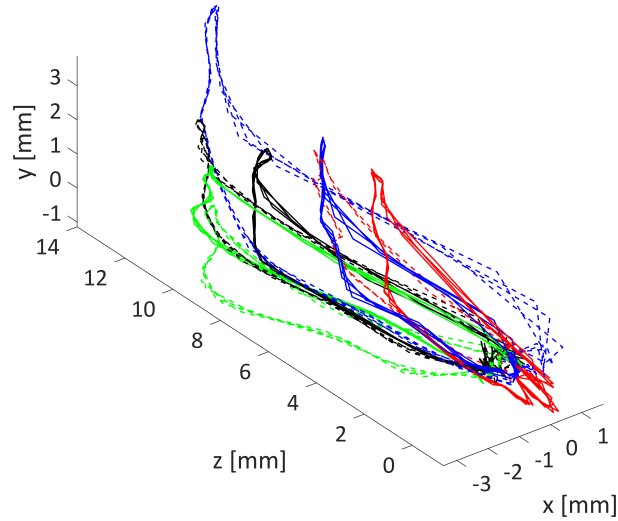


Figure 4.2: Representation of the dynamic displacement of Heart I (red lines), Heart II (green lines), Heart III (black lines) and Heart IV (blue lines) in 3D along four cardiac cycles measured by 3D-DIC. The solid and dashed lines were obtained as the average of the displacement components (x, y and z) at each state of the heart deformations for the NT and HT condition, respectively.

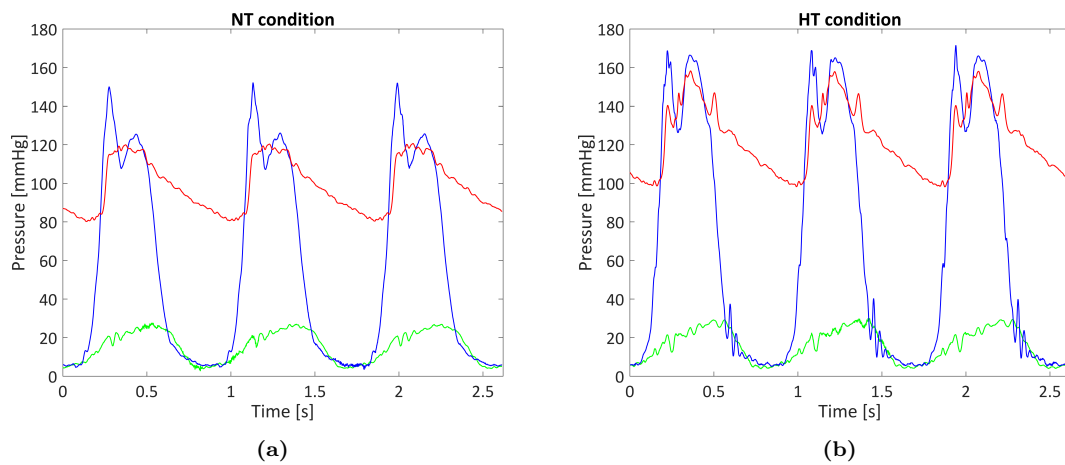


Figure 4.3: Recorded pressures data in the LV (blue line), aorta (red line) and left atrium (green line) for the NT (a) and HT (b) conditions.

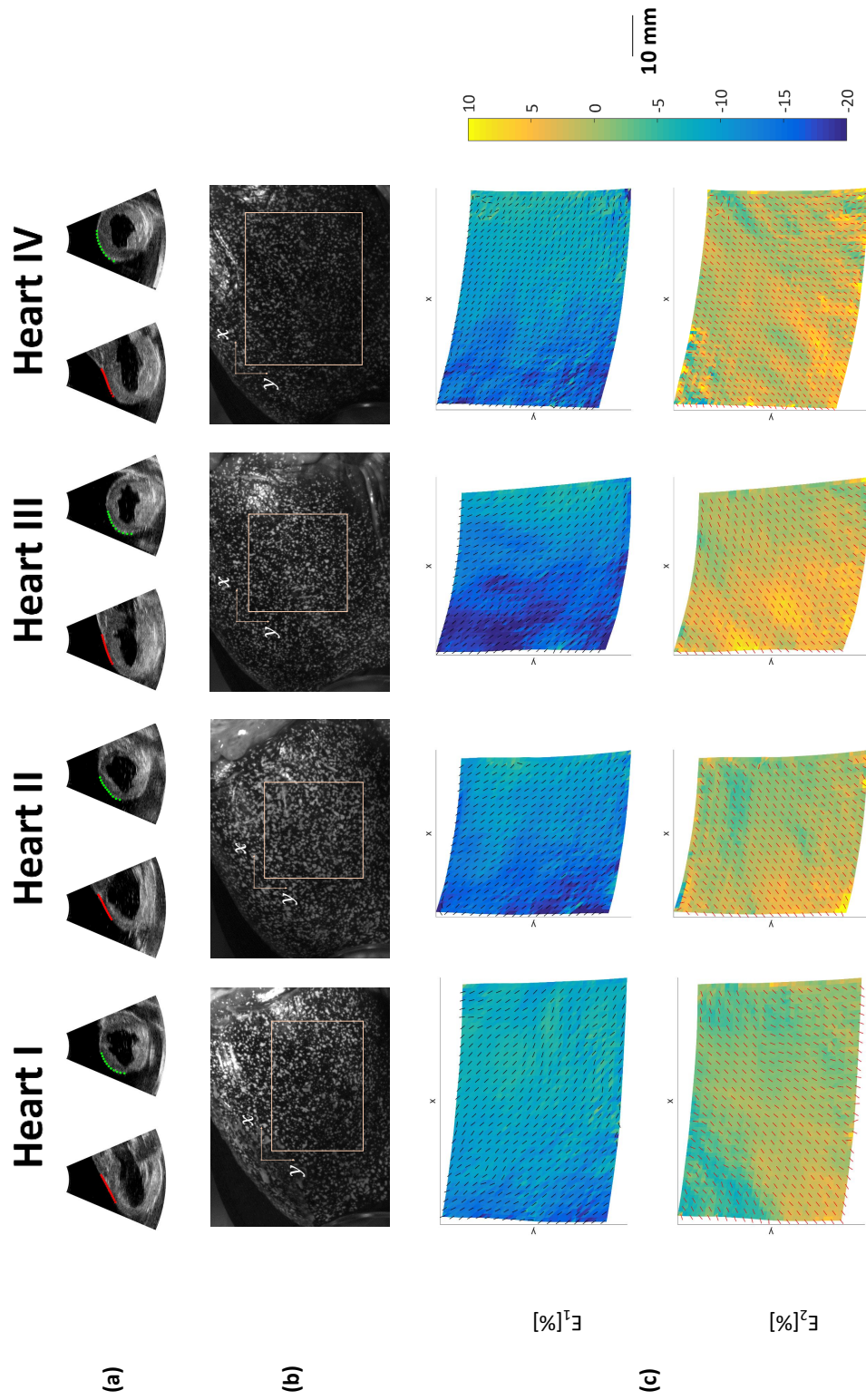


Figure 4.4: (a) B-mode image of the LAX and SAX views of each heart with points overlaid from which displacement and strain were extracted for comparison with 3D-DIC measurements. (b) Optical images of the LV surface of each individual heart with overlaid a schematic representation of the ROI selected in the 3D-DIC analysis. (c) Magnitude and direction of E_1 and E_2 at peak strain reconstructed with 3D-DIC over the ROI identified in (b).

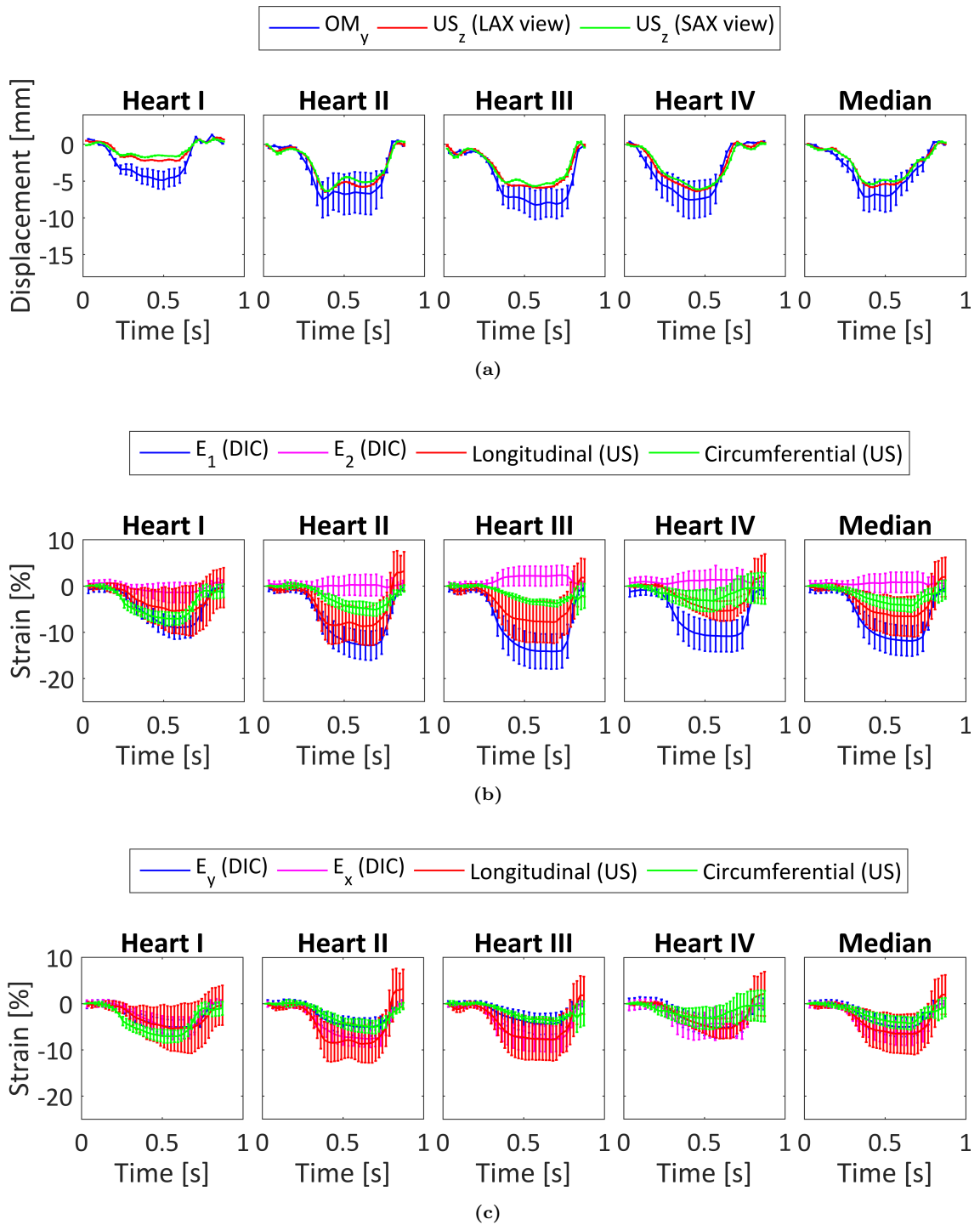


Figure 4.5: (a) Average and standard deviation of the displacement distribution extracted from 3D-DIC along the y-axis (OM_y in Fig. 4.1) and US-2D-STE LAX and SAX views along the z-axis (US_z in Fig. 4.1) in each heart and their median values over a single cardiac cycle. (b) Average and standard deviation for the maximum (E_1) and minimum (E_2) principal strains derived from 3D-DIC and the longitudinal and circumferential strains derived from US-2D-STE in each heart and their median values over a single cardiac cycle. (c) Average and standard deviation for the longitudinal (E_x) and transverse (E_y) strains derived from 3D-DIC and the longitudinal and circumferential strains derived from US-2D-STE in each heart and their median values over a single cardiac cycle.

Fig. 4.4a depicts the B-mode images of LAX and SAX views for each individual heart indicating the region (dotted lines) used to extract displacement and strain, estimated to correspond to the ROI imaged by the stereo cameras. Displacement curves showing average and standard deviation over a single cardiac cycle computed with 3D-DIC and US-2D-STE, for every heart, are reported in Fig. 4.5a. In details, median values of peak displacement amongst the four hearts were -7.1 ± 1.9 mm, -5.8 ± 0.1 mm and -5.4 ± 0.1 mm, from 3D-DIC, US-2D-STE LAX and SAX view, respectively. Fig. 4.5b shows the maximum (E_1) and minimum (E_2) principal strains quantified with 3D-DIC and the longitudinal and circumferential strains obtained from US-2D-STE. Fig. 4.5c shows also comparison of the US-2D-STE measurements with the longitudinal (E_x) and transverse (E_y) strains (i.e. Eq. (2.7)) quantified with 3D-DIC. In details, median values at peak strain over all four hearts were $-11.9 \pm 3.3\%$, $0.9 \pm 2.2\%$, $-6.4 \pm 2.6\%$, $-5.0 \pm 2.0\%$, $-6.6 \pm 4.4\%$ and $-4.3 \pm 1.4\%$, for E_1 , E_2 , E_x , E_y , longitudinal and circumferential strains, respectively. In each individual heart, full-field strains over the ROI reconstructed on the LV surface (Fig. 4.4b) with 3D-DIC are shown in Fig. 4.4c. In particular, this figure reports the spatial distribution of E_1 and E_2 over the ROI together with the principal directions at peak strain. As depicted in Fig. 4.4b, size and position of the reconstructed ROIs were different over the hearts because of changes in the anatomical structures and positioning of the heart with respect to the stereo cameras. Overall, width and height of the ROIs ranged between 45 to 60 mm and 35 to 40 mm, respectively.

Fig. 4.6a shows the linear regression between the displacements obtained from 3D-DIC and US-2D-STE in each heart along one cardiac cycle. In particular, as reported in Fig. 4.6b, median displacements measured from 3D-DIC showed a very strong correlation with US-2D-STE measurements in both the LAX view ($R^2 = 0.97$) and SAX view ($R^2 = 0.96$). Errors associated with data in Fig. 4.6b for each technique have not been reported here, however, error metrics from 3D-DIC and US-2D-STE are discussed in Section 4.4.

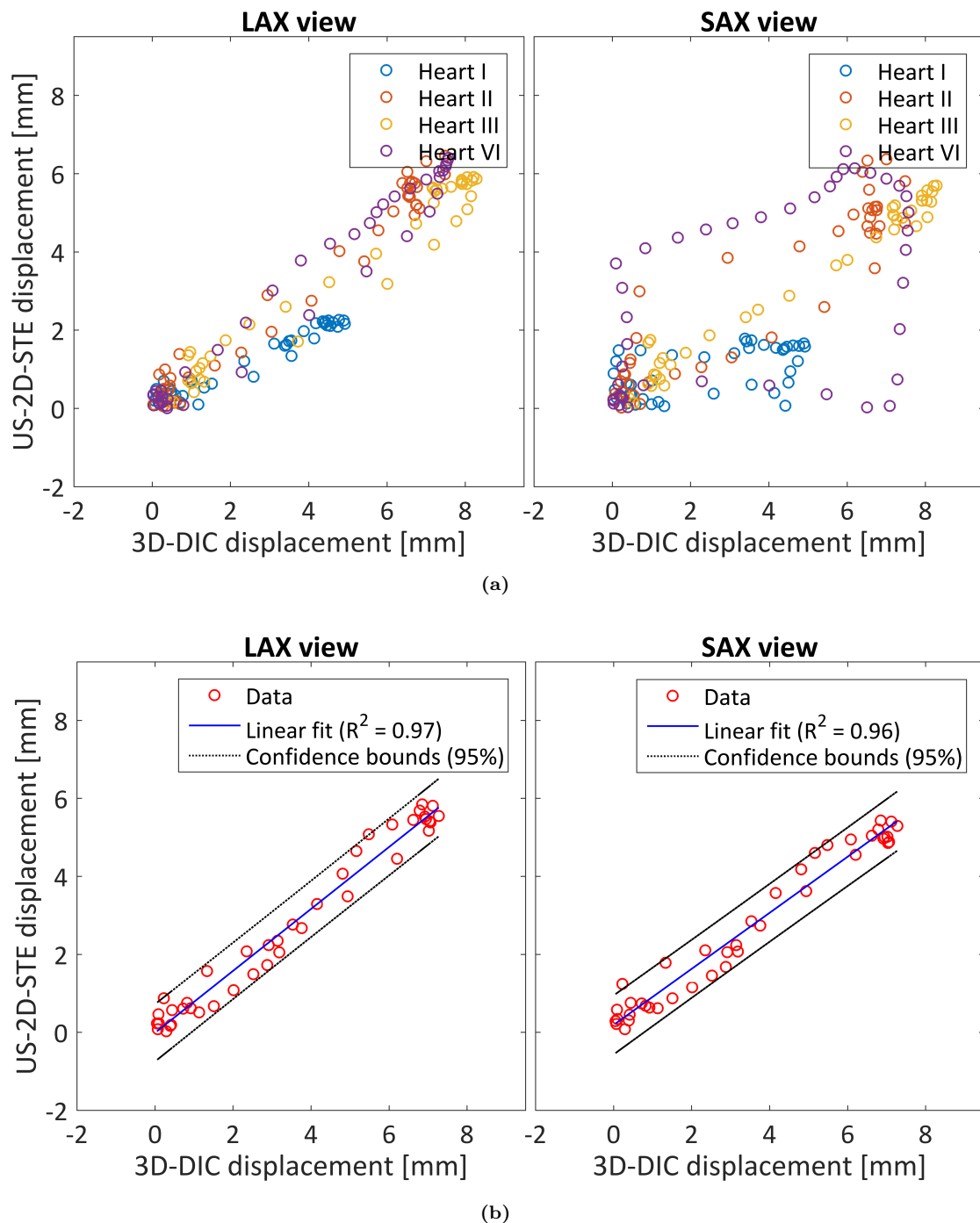


Figure 4.6: Linear regression between the displacement obtained from 3D-DIC and US-2D-STE, for the LAX and SAX views, for each heart (a) and their median values (b) along one cardiac cycle. Upper- and lower-bands represent the 95% confidence interval.

Table 4.2: Peak strain values along a cardiac cycle in each heart measured by 3D-DIC (Maximum and Minimum principal strain) and US-2D-STE (Longitudinal and Circumferential strain) for the NT and HT conditions.

| | Heart I | | Heart II | | Heart III | | Heart IV | |
|--------------------------|----------------|-------|-----------------|-------|------------------|-------|-----------------|-------|
| Peak strain[%] | NT | HT | NT | HT | NT | HT | NT | HT |
| Maximum principal strain | -9.0 | -11.3 | -12.9 | -15.2 | -14.2 | -15.5 | -10.9 | -13.0 |
| Minimum principal strain | 1.5 | 0.7 | 0.6 | 0.9 | 2.4 | 1.7 | 1.5 | 0.9 |
| Longitudinal strain | -5.4 | -8.7 | -8.7 | -10.6 | -7.9 | -6.0 | -5.4 | -7.9 |
| Circumferential strain | -7.1 | -6.9 | -5.1 | -7.0 | -3.8 | -6.0 | -3.2 | -7.6 |

Results obtained under the HT condition demonstrated similar overall behaviour to those presented in Fig. 4.5b for the NT condition. Peak strain values reported for the HT condition were greater than those for the NT condition for most outputs, as shown in Table 4.2.

4.4 Discussion

In this chapter, an experimental framework that enabled direct comparison of ultrasound- and optical-based strain imaging in an *in vitro* heart model has been described. Specifically, the aim of this work was to analyse displacement and strain obtained from 3D-DIC and US-2D-STE in order to evaluate the performance of these techniques. Estimation of displacement and strain errors, obtained from the 3D-DIC analysis of multiple images of the heart in the un-loaded configuration, showed deviations smaller than 6 μm and 1%, respectively.

Results shown in Fig. 4.2 demonstrate the ability of 3D-DIC to report the dynamic 3D displacement components of the epicardial surface and further confirm the repeatability of the process over multiple cardiac cycles. This is supported by results obtained in Chapter 3 of repeatability in the CBS platform and is in contrast to the typical behaviour observed when tracking displacements over multiple cycles with US-2D-STE resulting in residual tracking errors (i.e. drift) (Pettersen et al., 2017).

It should be noted that for the comparison between the two techniques, displace-

ment and strain behaviour were very similar, thus, results were reported in details only for the NT condition. Analysis of displacement values obtained from 3D-DIC and US-2D-STE reported in Fig. 4.4b shows very good agreement between the two US views and very strong correlation between two techniques, although with consistently larger displacements reported by 3D-DIC, as illustrated in Fig. 4.6b.

Although surface strain fields computed with 3D-DIC were reported in the principal strain configuration to remove coordinate system dependence, an absolute comparison of the strain measurements between these two methods remains challenging to accomplish because of the different nature of the two techniques and procedures used to calculate strain. However, Fig. 4.4 illustrates that maximum principal strain exceeded both the longitudinal and circumferential strains and minimum principal strain reported was less than either US-2D-STE measurement. This is coherent with the computed direction of the maximum principal strains shown in Fig. 4.4e, which lies between the longitudinal and circumferential directions consistently for all experiments. This suggests that a component of the increased magnitude of strain reported using 3D-DIC is associated with the orientation of the principal strain direction. It is feasible to repeat such an experiment with a greater number of US views to report strain at multiple angular increments, which would address this issue. However, it is also possible that the 3D motion of the cardiac surface demonstrated in Fig 4.2 leads to underestimation of strain in both the LAX and SAX views when using US-2D-STE as it is unable to detect out-of-plane motion.

Although the two deformation computation methods share some similarity (i.e. use of template matching algorithms), they do present many differences, especially, on how they calculate and process the displacement in order to derive strain, which makes a direct comparison of spatial resolution challenging. In particular, although US-2D-STE was performed on RF data to improve displacement tracking resolution (Lopata et al., 2009b), this is known to vary between the axial and lateral direction. In this study, speckle-tracking resolution, defined by the window size of the

last coarse-to-fine iteration, was 3.9 and 20.5 mm in the axial and lateral direction, respectively. However, due to the non-linearity of median filtering to regularise the estimated displacement and the subsequent use of a least-squares strain estimator, an exact quantification of the resulting strain resolution with US-2D-STE was not possible to achieve. Conversely, the evaluation of the spatial resolution of the 3D-DIC measurements reflected the choice of the parameters selected in the DIC analysis. Namely, the subset size accounted for the displacement spatial resolution, which corresponds to approximately 3.3 mm, while strain measurements were reported at a resolution determined by the step size (≈ 0.9 mm).

Comparing with other studies which have applied US-2D-STE, the absence of muscle contractility may explain the lower magnitude of longitudinal and circumferential strain estimated in this study when compared to strains measure achieved in isolated beating hearts (Pettersen et al., 2017). Underestimation of US-2D-STE strain, previously observed in another study comparing US-2D-STE with 2D-DIC (Gijbsbertse et al., 2018), is a known limitation of US-2D-STE which can be caused by its sensitivity to acoustic shadowing or reverberations, poor image quality and lower accuracy of tissue tracking at the depth associated with cardiac imaging and in the lateral direction (Mor-Avi et al., 2011). In addition, the experimental set-up used in the current study is limited as it was not possible to either acquire 3D-DIC and US-2D-STE image simultaneously or ensure precise alignment of the coordinate systems of the stereo cameras and US probe. It was also necessary to estimate the positions of the reconstructed ROI with 3D-DIC, as shown in Fig. 4.4d, within the LAX and SAX views, as shown in Fig. 4.4a, which may introduce some additional uncertainty in direct comparison between the methods. As a result, it is not possible to separate effects associated with inherent measurement errors from relative rotation of the coordinate system and uncertainty in ROI location.

Combined US- and DIC-based measurements have already been performed to study the behaviour of biological tissues; Chernak Slane and Thelen (2014) used 2D

US elastography to quantify motion and strain in *ex vivo* porcine flexor tendons and results strongly correlated with separate surface measurements obtained from 2D-DIC. Moreover, 2D-DIC was used as a reference to validate US strain measurements during *ex vivo* axial loading of human lateral collateral ligaments (Gijbertse et al., 2018). Furthermore, Campo et al. (2014) compared results from US and 3D-DIC obtained for assessment of pulse wave velocity in healthy individuals, although they could only compare velocity and acceleration between the two methods as strain was only calculated using 3D-DIC.

4.5 Summary

This chapter presents an experimental framework for strain imaging in an *in vitro* porcine heart platform using two distinct imaging techniques. Cardiac deformation was assessed under realistic haemodynamic conditions and controlled deformations of the heart. Combined measurements of 3D-DIC and US-2D-STE were carried out to analyse displacement and strain of the heart surface. 3D-DIC demonstrated high repeatability in assessing the dynamic 3D motion and strain of the LV surface over multiple cardiac cycles unlike US-2D-STE, which is prone to accumulated errors over time that cause a drift in the tracking. Therefore, analysis of displacement and strain was performed over a single cardiac cycle. Results showed a very strong correlation of displacements obtained from the two methods, however, with systematically larger displacement measured by 3D-DIC. Directions of maximum principal strain reconstructed with 3D-DIC showed a distinctive orientation at peak strain, which reflected the distribution of the circumferential and longitudinal strain obtained from US-2D-STE. This chapter demonstrates the potential of 3D-DIC to perform repeatable and dynamic measurement of displacement and strain during heart deformations providing a localised measurement of strain, which cannot be achieved with US-2D-STE.

Chapter 5

Application of 3D-DIC in an *ex vivo* experiment

The previous chapters have described the development of an optical method based on 3D-DIC (Chapter 2) and *in vitro* applications of this method (Chapter 3 and 4). In particular, starting from the benchmark tests of earlier chapters, this work has investigated the performance of 3D-DIC in experiments intended to resemble the pumping function of the heart using the Cardiac BioSimulator. However, although this platform offers repeatable controlled behaviour of heart deformation (through tuning of the loading conditions) providing ideal conditions for assessment of multi-modal strain imaging (Chapter 4), the clinical relevance of the strain measured on the heart is limited as cardiac contraction is absent. This chapter reports a preliminary effort to apply 3D-DIC to determine high-resolution full-field strain in an isolated porcine heart, in which contraction of the cardiac muscle is restored.

5.1 Introduction

The first measurements of epicardial deformation in animals using optical methods date back to the 1980s and consisted mainly of tracking the motion of markers attached to the epicardial surface (Table 5.1). Prinzen et al. (1986) measured *in vivo* strains of the canine epicardium before and after local ischemia induced by occluding the anterior branch of the left coronary artery. In particular, they recorded using a video camera the motion of approximately fifty markers (diameter 1.5 mm) attached to the epicardial surface over a region of 15-20 cm². Distinctions between the two states of the heart were highlighted in the strain results and authors claimed that the method could achieve a spatial resolution of 5 mm and an accuracy of 0.5% in measuring deformations. In a similar study, McCulloch et al. (1987) sutured three markers, positioned 8-27 mm apart, on the LV free wall to form a triangle on the epicardium of canine hearts. The motion of these markers was recorded using biplane video imaging during quasi-static LV volume filling, obtained by pumping saline through a mitral cannula connected to a saline-filled loading column at pressures up to 20 mmHg. Mean ranges of maximum and minimum principal strains were reported as 0-13.9 and 0-7.2%, while the accuracy of the method reported as the mean of the absolute reconstruction errors of each marker was 0.25 mm. More recently, Gaudette et al. (2004) used an optical technique based on 2D computer-aided speckle interferometry (CASI) to track the motion of silicon and retro-reflective beads dispersed randomly onto the epicardial surface of isolated rabbit hearts. Although this technique provided measurements at a good spatial resolution of 50 μm /pixels, as a 2D technique, it did not take into the account the curvature and out-of-plane motion of the heart.

In the last decade, more advanced optical techniques have been developed to combine mapping of membrane potential and deformation of the epicardium to study the electromechanical coupling of the heart. Seo et al. (2010) recorded simultaneously strain distribution and transmembrane potential while applying controlled

uni-axial stretches to perfused rabbit right ventricular tissue preparations. From the tracking of bead markers attached to the ventricular wall, they quantified the uni-axial strain (1D) strain on the ventricular wall. In particular, they used a cross-correlation technique to estimate marker displacement and affine transformation to optimise marker positions. In an analogous work, Bourgeois et al. (2011) monitored electrical waves and mechanical contractions in Langendorff-perfused hearts using an optical method. Motion tracking of the markers sutured to the ventricular epicardium was performed using 2D cross-correlation. Strains were calculated locally for each triangle defined by triples of epicardial markers using homogeneous finite strain theory. However, results reported in that study were limited by the use of a single camera, which could not provide an accurate estimate of the distances between points on the 3D epicardial surface, and by the reduced spatial resolution caused by the small number of markers. A further study on optical mapping of the heart was performed by Laughner et al. (2012), who captured 3D surface geometries of Langendorff-perfused rabbit hearts using *structured light* imaging. Although this technique has potential to derive strain measurements from the shape of the heart, it requires very expensive hardware (e.g., laser, projector). Another interesting study, already discussed in Chapter 3, reports measurements of epicardial deformation in the porcine heart operating in LV working mode in combination with mapping of membrane potential on the epicardium (Zhang et al., 2016). The magnitude of epicardial strains reported in that study were comparable to those reported in the current work.

As discussed previously, 3D-DIC overcomes some limitations of the above-mentioned techniques, in particular, the use of stereo cameras and marker-free procedure for image tracking allows the reconstruction of the curvature and out-of-plane motion of the heart with a very flexible temporal and spatial resolution which, unlike marker-based tracking techniques that are limited by the size and spacing of the markers, can be adjusted by simply tuning DIC parameters and

Table 5.1: Review of relevant works using optical methods to quantify epicardial strains in animal heart preparations.

| Method | Animal | Heart preparation | Experiment | Remarks | Reference |
|---------------------------------------|--------|---|--|---|---------------------------|
| Video imaging | Dog | <i>In vivo</i> with open chest | Motion tracking of 50 markers glued to the epicardium before and after inducing local ischemia of the LV wall | <ul style="list-style-type: none"> • Single camera (2D measurement) • Markers (1.5 mm diameter) made of plastified paper and painted with white correction fluid • ROI of 15-20 cm² • Spatial resolution of 5 mm | (Prinzen et al., 1986) |
| Biplane video imaging | Dog | Mitral valve cannulated to a loading fluid column controlling pressure during LV volume filling | Motion tracking of 3 markers sutured to the epicardium during quasi-static LV filling | <ul style="list-style-type: none"> • Two cameras (3D measurement) • Markers made of fine silk threads • Markers spacing of 8-27 mm • LV pressure up to 20 mmHg | (McCallloch et al., 1987) |
| Computer-aided speckle interferometry | Rabbit | Modified Langendorff-perfused heart | Motion tracking of particle and beads dispersed onto the epicardial surface for different LV pressures and with global and regional ischemia | <ul style="list-style-type: none"> • Single camera (2D measurement) • Particle made of silicon carbide (40 μm diameter) • Retroreflective beads (60 μm diameter) • Spatial resolution of 50 μm | (Gaudette et al., 2004) |
| Video imaging | Rabbit | Perfused tissue preparation | Motion tracking of beads markers on the right ventricular wall tissue during uni-axial stretched | <ul style="list-style-type: none"> • Single camera (2D measurement) | (Seo et al., 2010) |
| Video imaging | Pig | Langendorff-perfused heart | Motion tracking of 14 markers glued to the ventricular epicardium during bipolar pacing from the right ventricle at 300 and 500 ms | <ul style="list-style-type: none"> • Single camera (2D measurement) • Ring-shaped markers made of black polyethylene • Markers thickness and diameter of 0.25 and 4 mm, respectively | (Bourgeois et al., 2011) |
| Structured light | Rabbit | Langendorff-perfused heart | Fringe pattern projected onto the heart and multiframe geometric registration to estimate dense correspondence between consecutive 3D scans | <ul style="list-style-type: none"> • Single camera + fringes projector (3D measurement) • Reduced accuracy-of-motion estimates relative to speckle/marker tracking | (Laughner et al., 2012) |
| Biplane imaging | Pig | LV working mode | 3D tracking and reconstruction of 20 fiducial markers glued to the anterior LV epicardium with tissue adhesive | <ul style="list-style-type: none"> • Two cameras (3D measurement) • Markers diameter of 2 mm • Markers spacing of 8 mm | (Zhang et al., 2016) |

selecting the appropriate camera hardware.

In this chapter, optical measurements using 3D-DIC were performed in an isolated beating heart (PhysioHeartTM, LifeTec Group, Eindhoven, NL). Compared to most of the studies previously reviewed that employed small hearts (e.g., rabbit), this preparation uses a large heart model from pigs closer to human conditions. However, at the same time, measurements of 3D-DIC in this setup are more complex than the *in vitro* measurements described in previous chapters because of the reduced control of the behaviour of the heart. Moreover, as the coronary arteries are being perfused, this poses an important challenge to the application of an effective speckle pattern on the cardiac surface as arterial and myocardium tissues transude blood that deteriorate its quality for image matching.

5.2 Materials and methods

5.2.1 *Ex vivo* heart preparation

A modified version of the Langendorff mode preparation was adopted in this study (de Hart et al., 2011). In particular, the heart was perfused, in a retrograde manner, *via* the coronary arteries using an aortic cannula inserted into the ascending aorta. In particular, coronary perfusion pressure was kept at 80 mmHg. While in a typical Langendorff setup, the LV cavity is unloaded, in this study, the LV was filled with blood through a preload of 10 to 20 mmHg from a reservoir connected to the left atrium. This provided resistance to LV contraction and resembled more closely *in vivo* cardiac mechanics. After a few minutes of coronary perfusion, myocardial contractility was reestablished and sinus rhythm was restored with defibrillation. In particular, the heart was paced with a basic cycle length from 550 to 750 ms. Coronary flow, LV and perfusion pressures and the electrocardiogram (ECG) were monitored throughout the experiment.

5.2.2 3D-DIC measurement

Optical measurement of epicardial deformation in the Langendorff-perfused heart was performed using the same 3D-DIC methodology employed in the previous studies and described in detail in Chapter 2.

Upon restoring heart contraction activity, the LV epicardial surface was provided with a speckle pattern following the procedure outlined in Section 2.5.1.1 to enable image correlation.

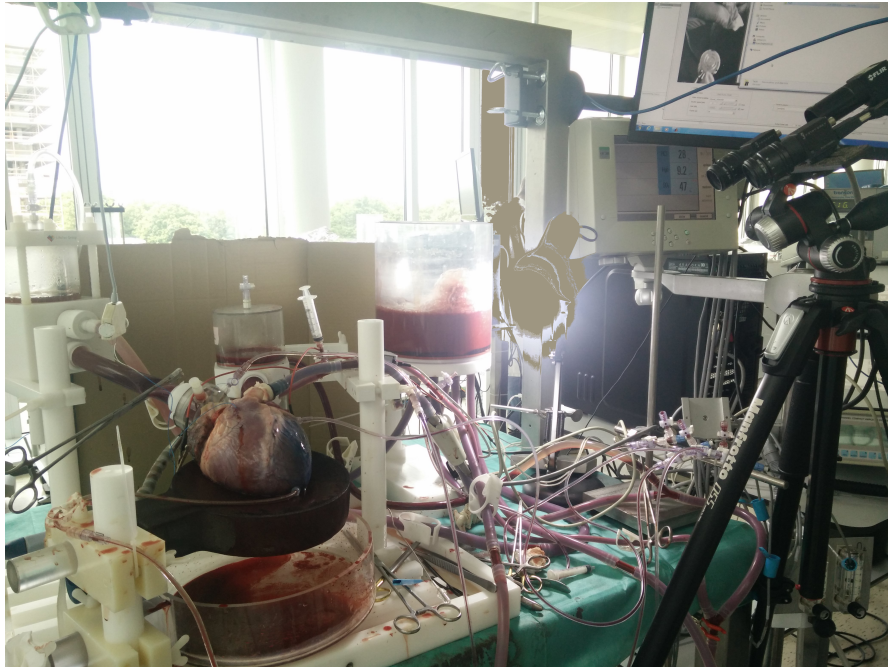


Figure 5.1: Picture of the experimental setup including the *ex vivo* model of the heart in a modified Langendorff preparation and positioning of the stereo cameras used for 3D-DIC measurement.

Stereo cameras equipped with 12 mm focal length lenses (LM12JC1MS, Kowa Company, Ltd., Nagoya, Aichi, Japan) were placed at a distance of approximately 50 cm from the heart (Fig. 5.1). This resulted in a FOV, image resolution, magnification of roughly 180 cm, $0.17 \mu\text{m}/\text{pixels}$ and 0.02, respectively. A white-light LED lamp was used to improve lighting conditions as camera sensors shutter speed was reduced to 5 ms to avoid motion blur. Image acquisition was carried out at 30 fps. As reported in Section 2.2, the stereo cameras were calibrated by imaging a chequerboard pattern with internal squares of 2 mm and using the Matlab Stereo

Camera Calibrator application. Stereo image correlation and calculation of local epicardial deformations were performed as described in Sections 2.4 and 2.4.2, respectively. Specifically, the subset and step size chosen for the DIC analysis were 33×33 and 9×9 pixels, respectively.

Stereo optical images of the heart were acquired at several stages and under different states of the heart. Unfortunately, as the experiment proceeded the surface of the heart became extremely wet because of the continuous sweating of the tissues. This made the application of the speckle pattern very challenging as its quality quickly degraded and, more importantly, compromised the error metrics of the method estimated in the previous experiments. Fig. 5.2a shows an image of the heart in which tissues *sweating* created reflective regions on the epicardial surface preventing 3D-DIC measurement.

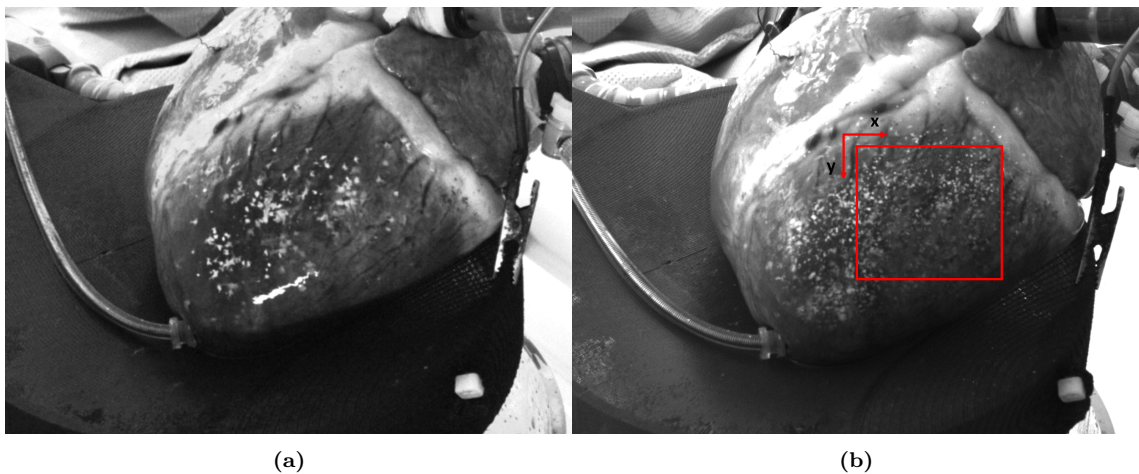


Figure 5.2: (a) Example of an experimental image in which the wet surface of the heart caused the degradation of the speckle pattern quality. (b) Image of the heart captured in the reference state (end diastole) with overlaid the rectangular ROI investigated in the 3D-DIC analysis.

Notwithstanding this limitation, 3D-DIC was performed successfully over about ten cardiac cycles corresponding to 192 frames. The analysis reported in this study focused on the assessment of deformations within a region of interest (ROI), identified on the LV shown in Fig. 5.2b, with a width and height of approximately 46 and 42 mm, respectively. In particular, the ROI was selected in the image of the heart corresponding to end diastole, thus, deformation was calculated with respect to this

configuration with negative values indicating shortening of the LV. Displacement and strain reconstructed in the ROI were evaluated over multiple cardiac cycles during which the heart behaved differently in terms of LV pressure and coronary flow. Moreover, full-field surface map of maximum and minimum principal strains with their directions were calculated.

5.3 Results

A representation of the cardiac tissue displacement vector field in two frames captured during diastole and systole is shown in Fig. 5.3a and 5.3b, respectively. In particular, these were obtained from the displacement field extracted from the temporal matching and tracking of the left images captured during heart deformation with respect to the un-deformed reference state (i.e. end-diastole). As the data resolution of the displacement field is determined by the step size, displacement vectors were obtained every 9 pixels in the ROI, although in this figure have been reported every 18 pixels for visual clarity. Overall, orientation of displacement vector followed a specific pattern during the cardiac cycle, starting more aligned to the longitudinal direction of the heart and, then, moving anticlockwise towards the circumferential direction during systole.

Fig. 5.4a shows the relevant parameters recorded in the platform such as coronary flow, perfusion and LV pressures (Fig. 5.4a) together with the 3D-DIC measurement of displacement (Fig. 5.4b) and strain (Fig. 5.4c) over the same cardiac cycles. Fig. 5.4b illustrates the displacement along the x, y and z directions as a function of time obtained as average of surface displacement values from the rectangular ROI depicted in Fig. 5.2b. In particular, negative values of the displacement along the y-axis during contractions of the heart corresponded to an upward motion of the heart relative to Fig. 5.2b, while during negative values of the displacement along the x- and z-axis the heart moved leftward and towards to the stereo cam-

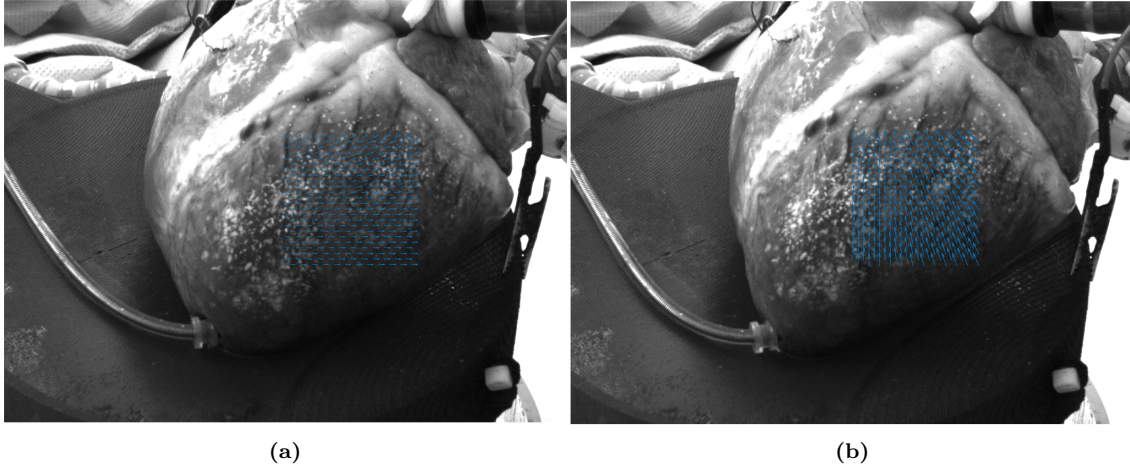


Figure 5.3: Representation of the displacement vector field extracted from frames captured during diastole (a) and systole (b). For visual clarity, vectors have been plots every other 18 pixels (two times the step size).

eras, respectively. Fig. 5.4c shows in the same plot maximum (E_1) and minimum (E_2) principal strains as a function of time obtained as average of surface strain values from the ROI. As previously mentioned, negative values corresponded to shortening of the cardiac tissues while positive values to lengthening. Moreover, this figure shows the three contiguous cardiac cycles (cycle A, B and C) that have been considered for a further analysis of displacement and strain measurement in the Langendorff-perfused heart. The three cycles represent two different states of the heart: i) a state in which pressures are more similar to physiological human conditions (see Fig. 1.3 for a comparison with human cardiac cycle) that is denoted by cycle A and ii) a state in which lower but similar pressures are recorded in the heart between two cardiac cycles (cycle B and C).

Accordingly, Fig. 5.5 and 5.6 report the evaluation of displacement and strain for these consecutive cardiac cycles. Specifically, Fig. 5.5 shows the 3D dynamic displacement of the reconstructed LV surface for the three contiguous cardiac cycles. These curves were obtained as the average of the displacement values throughout the cardiac cycles for each components (x, y and z). While, Fig. 5.6 shows in a single plot (upper pane) the distribution of the average of E_1 and values of the LV pressure (blue line) and perfusion pressure (red line), and the coronary flow behaviour (bottom

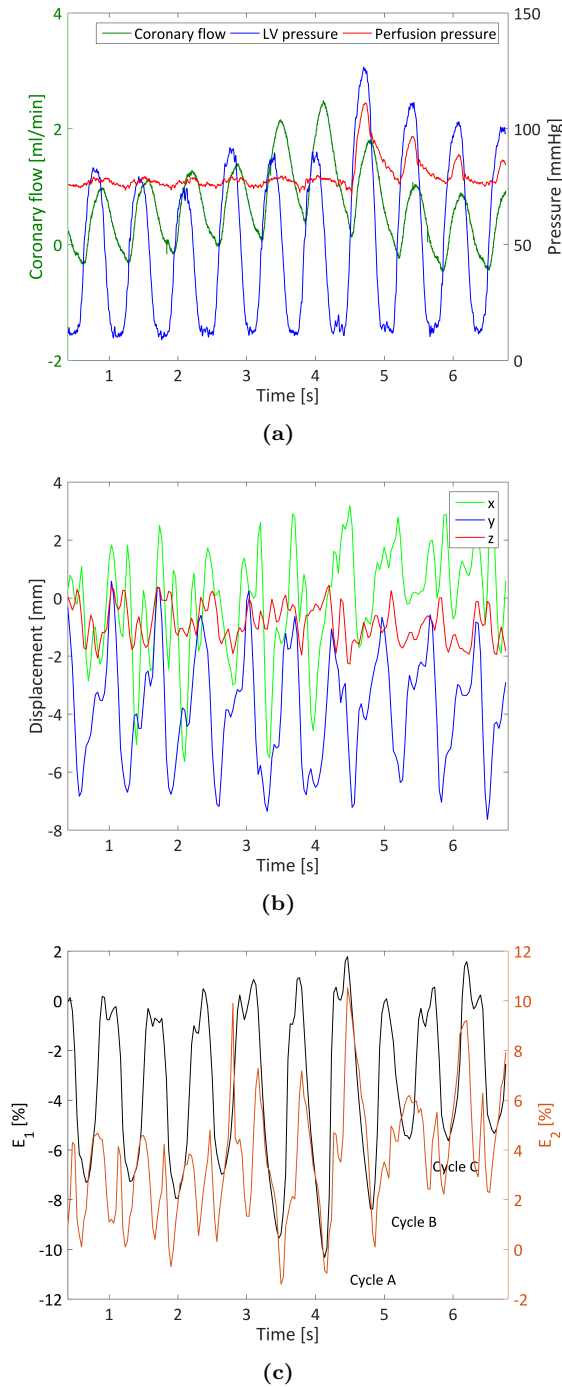


Figure 5.4: Recorded data in the heart and 3D-DIC measurements over the same cardiac cycles. (a) Coronary flow (green line), LV pressure (blue line) and perfusion pressure (red line) behaviour. (b) Plot of the average of each displacement components within the reconstructed ROI along the cardiac cycles. Referring to Fig. 5.2b, negative values of the displacement along x and y direction denoted a motion of the heart leftwards and upwards, while negative values of the displacement along z a motion of the heart towards the stereo cameras. (c) Combined representation of the average maximum (E_1 , black line) and minimum (E_2 , orange line) principal strains obtained in the reconstructed ROI on the LV surface along the cardiac cycles. In this plot, three consecutive cardiac cycles have been identified for a further analysis of displacement and strain using 3D-DIC since during these time points LV pressure values were within the human physiological range.

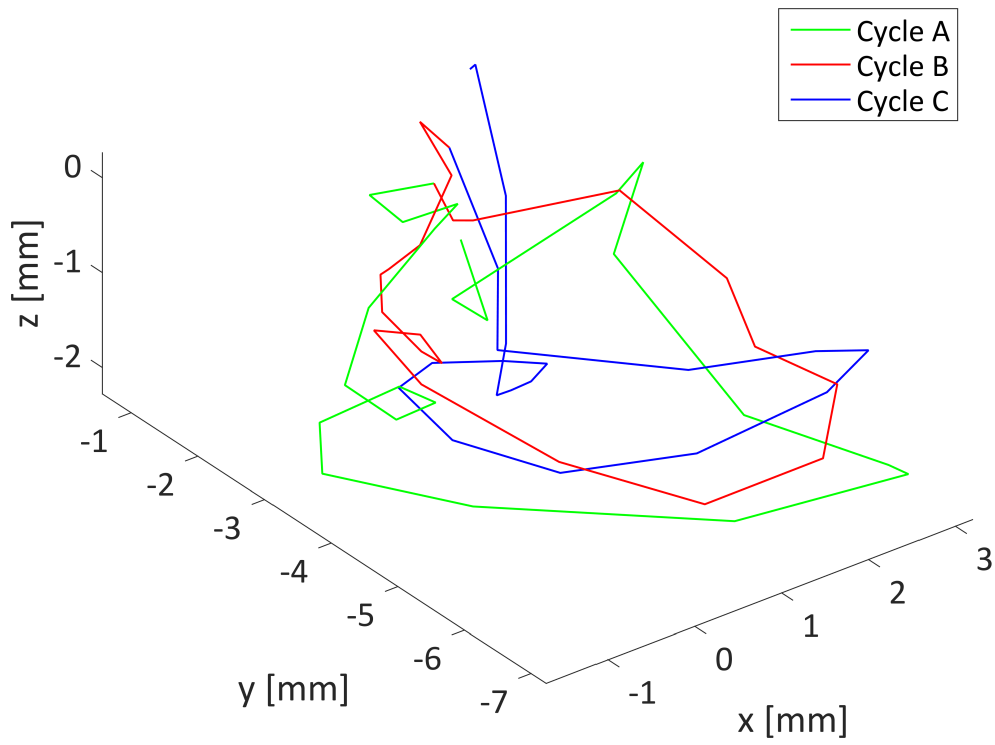


Figure 5.5: Representation of the dynamic displacement of the Langendorff-perfused heart in 3D along the three consecutive cardiac cycles measured by 3D-DIC. The lines were obtained as the average of the displacement components (x , y and z) at each state of the heart deformations.

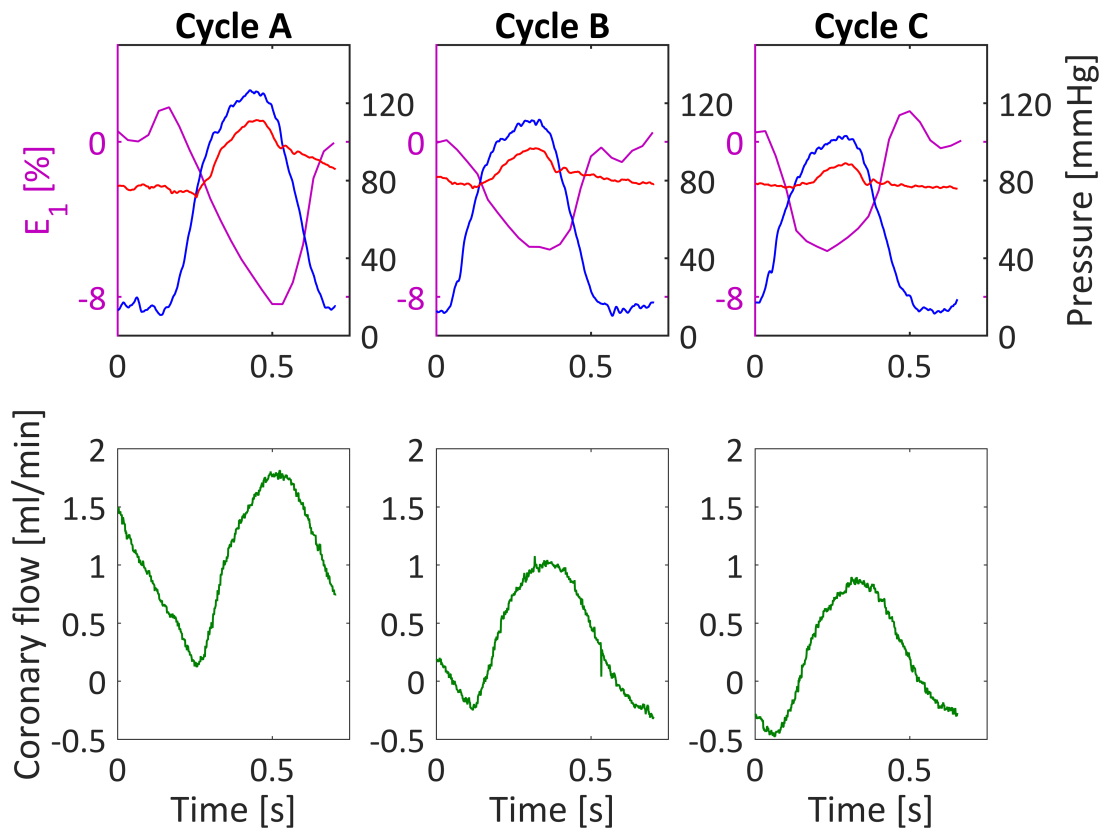


Figure 5.6: Combined representation of the average maximum principal strain distribution (purple line) within the reconstructed ROI on the LV surface obtained from 3D-DIC with the perfusion pressure (red line) and LV pressure (blue line) for the three cardiac cycles investigated (**upper pane**). The start of the cardiac cycle corresponds to end-diastole in which strain is close to zero, while when the coronary flow (**bottom pane**) is maximum, strain magnitude reaches its peak value.

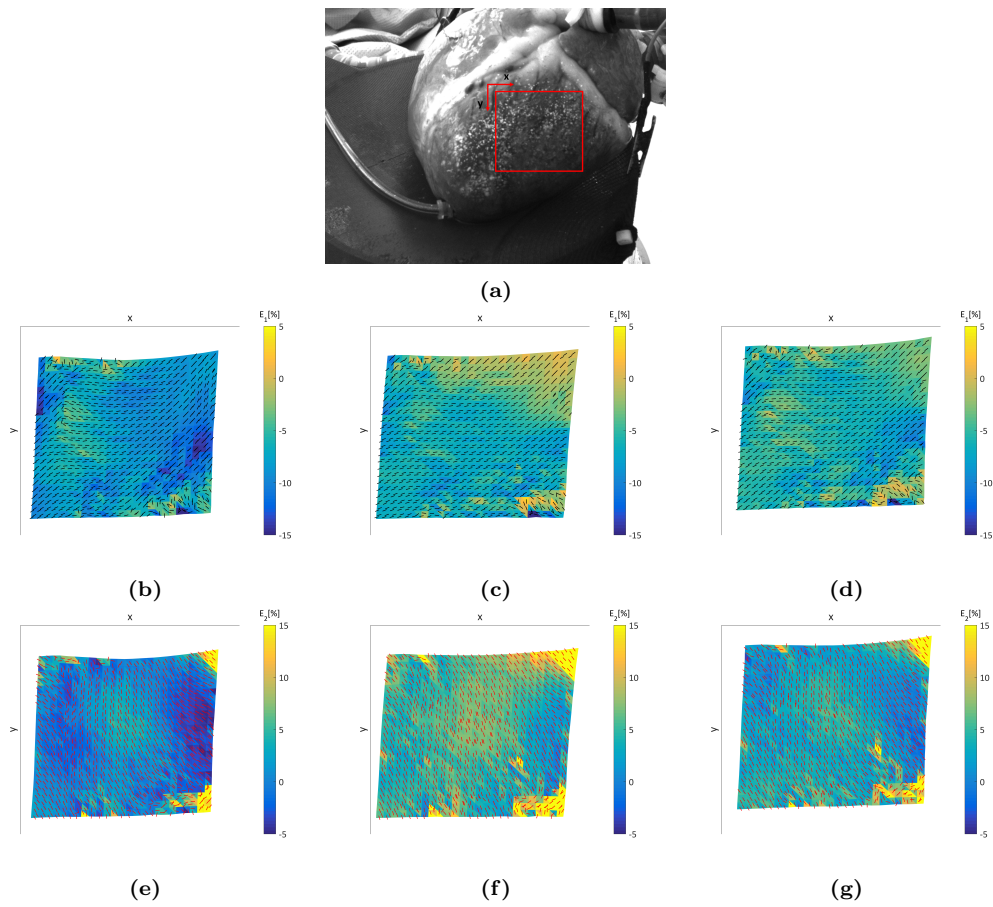


Figure 5.7: Full-field surface map of the maximum (b-d) and minimum (e-f) principal strain from the reconstructed ROI (red box) on the LV depicted in (a) at peak strain for the three cardiac cycles. Maximum (black segments) and minimum (red segments) principal directions are also shown on the map. Width and height of the ROI ranged approximately between 46-50 and 42-46 mm, respectively.

pane) for the three cycles. The beginning of the curves represents end diastole with values of LV pressure, perfusion pressure and E_1 close to 20 mmHg, 80 mmHg, and 0%, respectively. As pressures and coronary flow rose, strain magnitude increased reaching a peak when the coronary flow was maximum.

Finally, in Fig. 5.7, the full-field map of the principal strains, in the reconstructed ROI on the LV surface depicted in Fig. 5.7a, has been reported. In particular, this figure shows the maps of the maximum (Fig. 5.7b, 5.7c and 5.7d) and minimum (Fig. 5.7e, 5.7f and 5.7g) principal strains with their directions for the three cardiac cycles at peak strain. The strain maps were reconstructed using the same spatial resolution of the 3D-DIC measurement resulting in 1150 triangular elements with an area of approximately 1.25 mm².

5.4 Discussion

This chapter presents a preliminary study to analyse epicardial deformation in a Langendorff-perfused heart using 3D-DIC. In particular, this is the first attempt to use this optical technique to quantify *ex vivo* full-field displacement and strain in a porcine heart reproducing realistic cardiac mechanics conditions. In fact, the heart preparation used in this work differed from the previous experimental model of the heart employed in the studies described in Chapters 3 and 4, in which the heart was passively actuated by an external pump which imposed specific loadings to the LV. In the Langendorff preparation, myocardial contraction activity is restored by applying a constant pressure to the aorta, which closes the aortic valve and drives the perfusion solution through the coronary arteries. Although in this configuration there is no ejection of blood from the LV to aorta, in the current study, as the LV was filled with blood to provide a resistance to the ventricular wall contraction, mimicking *in vivo* human conditions, during some cardiac cycles, LV pressure exceeded the perfusion pressure causing blood to flow through the aorta.

Measurements of displacement and strain were successfully achieved on the LV surface over multiple cardiac cycles and conditions of the heart. As shown in Fig. 5.4, the number of pulses detected by the sensors placed in the heart, to record coronary flow, LV and perfusion pressures, were consistent with those obtained from the measurement of 3D-DIC of displacement and strain. The analysis of the displacement components, reported in Fig. 5.5, shows that the motion of the LV surface was different in three consecutive cardiac cycles. Moreover, this figure highlights the complex behaviour of the *ex vivo* beating heart if compared to the *in vitro* heart model of previous experiments, in which the displacement of the heart measured with 3D-DIC was very repeatable along several cardiac cycles (Fig. 4.2). The detailed representation of the strain obtained in each cardiac cycle, shown in Fig. 5.6, confirmed the ability of 3D-DIC to differentiate strain under different states of the heart (i.e. pressure values closer to human condition vs. reduced). Specifically, peak strain differences between the cycle A and the other two cycles were greater than the 1% strain threshold that the developed 3D-DIC methodology can accurately detect, as seen in Chapter 2. The full-field surface maps on the surface of the LV in Fig. 5.7 show a non-uniform distribution of the strain at peak deformations. However, although magnitude of the values differed, the same localised strain features on the maps were observed in the different cardiac cycles. Specifically, excluding outliers close to the edges of the reconstructed ROI (e.g. top and bottom right corners), which are often obtained from 3D-DIC, principal strain directions were consistent across cycles. Compared to the previous experiments in the CBS platform, in which the minimum principal strain components measured were negligible, in this heart preparation, the minimum principal strain components observed were much larger with average peak strains up to 10% (Fig. 5.4c). Principal strains directions varied across the ROI without showing a preferred orientation along the heart. This further demonstrates the complex behaviour of the strain in the Langendorff-perfused heart if compared with the strain fields extracted from the CBS platform (e.g. Fig.

4.4e).

Although, 3D-DIC provided localised and full-field strains on the LV surface with a spatial resolution of approximately 1.5 mm, which is one order of magnitude lower than those obtained from previous optical measurement of epicardial deformation (Table 5.1), this study was not exempted by some limitations. For instance, the generation of the speckle pattern on the cardiac surface was very challenging to accomplish as operations on the heart (e.g. defibrillation) required multiple applications and, most importantly, once generated the quality of the speckle pattern quickly deteriorated as blood transuded on the epicardium from the myocardium and coronary arteries. Therefore, 3D-DIC measurements were limited to a reduced ROI on the LV surface which precluded to perform a detailed analysis over the whole LV. Moreover, although this heart preparation resembled closer the *in vivo* cardiac mechanics of the human heart if compared to the CBS platform, deformations that occurs in a Langendorff setup are smaller than those of a working mode heart (Petterson et al., 2017).

5.5 Summary

In this chapter, full-field optical measurements of displacement and strain on the epicardial surface of a porcine heart prepared in a Langendorff-mode configuration are reported. This study extends the application of 3D-DIC of previous chapters in an *ex vivo* heart which mimicked more closely *in vivo* human cardiac mechanics. Results displayed the complex deformation behaviour of the epicardium under different conditions of the heart, which 3D-DIC was able to differentiate within the baseline error of the method. In particular, localised and detailed measurements from 3D-DIC, reported with a spatial resolution one order of magnitude lower than those obtained in previous works using optical methods to measure deformations on the epicardium, showed the non-uniform strain distribution over the reconstructed

region on LV surface. As a first attempt to use 3D-DIC for *ex vivo* quantification of epicardial strain in a porcine heart, this chapter highlights the challenges and limitations associated with the application of this technique (i.e. speckle pattern application and reduced control of the experimental conditions).

Chapter 6

Conclusions

The aim of this project was to develop an experimental optical method to perform a full-field and dynamic characterisation of the deformations on the left ventricle (LV) surface of *in vitro* and *ex vivo* model of the heart. This aim was achieved to provide detailed and localised measurements of strain on the heart, which can serve as a reference to clinical imaging modalities (i.e. US-2D-STE). The main contribution of this thesis is the novel application of 3D-DIC for cardiac strain imaging after a thorough validation and optimisation of this technique. In particular, tuning of the optical system and DIC parameters through benchmarking tests (Chapter 2) allowed to obtain 1% error from the reconstruction of the strain field on the cardiac surface, resulting an acceptable metrics for an accurate quantification of epicardial strains, which are larger than 10%.

From benchmark tests, this project then passed to the full-field analysis of an *in vitro* model of the heart (Cardiac BioSimulator), which allowed to impose realistic and controlled loading conditions to the LV. In this study, the high repeatability of 3D-DIC measurement was demonstrated as well as the ability to reconstruct with a high spatial resolution (≈ 1.5 mm) full-field principal strain directions on the LV, useful to show the non-uniform behaviour of the cardiac tissues (Chapter 3). Furthermore, this study highlighted the potential of combining multiple imaging technique to evaluate the performance of 3D-DIC and US-2D-STE under the

same experimental conditions. Therefore, in Chapter 4, these two techniques were employed in the Cardiac BioSimulator to measure displacement and strain in the porcine heart. Although an exact comparison was not possible to achieve being two very distinct methods, displacement and strain were quantified with the 3D-DIC and US-2D-STE showing the superiority of the optical method for dynamic measurement, as the ultrasound-based technique suffered from accumulated errors over the analysis of multiple cardiac cycles. Finally, this thesis concludes with the use of 3D-DIC in an *ex vivo* beating heart to explore the potential and limitations of this method in studying deformations of a heart model, which resemble more closely *in vivo* human cardiac mechanics (Chapter 5). The complexity of this experiment largely increases compared to the previous *in vitro* applications of 3D-DIC, especially because of the lower image quality obtained of the speckle pattern image of the heart as the cardiac surface resulted very wet during operations of the platform. However, in selected frames captured during contractions of the heart, in which 3D-DIC successfully reconstructed full-field displacement and strain on the LV surface, the detailed and localised behaviour of the heart was shown. In particular, this work demonstrated the potential of 3D-DIC, compared to existing optical methods used for mapping of epicardial deformation, to quantify strain with a spatial resolution improved by one order of magnitude, useful when studying anisotropic and inhomogeneous materials such as cardiac tissues.

6.1 Key findings

The thesis aim and objective were fulfilled by the results reported in the various chapters, and summarised in the previous section. The main contributions of this project to the biomechanics communities is outlined here:

The 3D-DIC methodology including procedures for speckle pattern application over the surface of a porcine heart and workflow for localised and high-resolution full-field

deformations is described in detail in this thesis.

The assessment of geometrical deviations in the 3D reconstruction of the porcine heart surface published in (Ferraiuoli et al., 2017) provides an estimate of the errors obtained with 3D-DIC.

The *in vitro* applications of 3D-DIC showed the high repeatability of this method and the potential to obtain a detailed full-field strain map with a resolution of approximately 1 mm (Ferraiuoli et al., 2019b). Moreover, unlike US-2D-STE, the ability to perform dynamic measurement of displacement and strain in the heart is reported (Ferraiuoli et al., 2019a).

Finally, this project shows the benefits of employing 3D-DIC for full-field analysis of *ex vivo* beating hearts, especially, in terms of spatial resolution that this method can achieved compared to current optical method.

6.2 Limitations

Although this study describes the development and application of a very powerful method for full-field shape and deformation analysis in the heart, there are several limitations that affect the outcome of this study. The most important are herein listed:

- Measurement of 3D-DIC was limited to a reduced rectangular region (usually 50 by 45 mm) on the LV surface because of the use of only two cameras for the 3D reconstruction and lighting reflection issues over the curvature of the heart surface.
- Although, this study estimated the influence of different DIC parameters (i.e. subset size, step size and stereo angle), 3D-DIC results can be affected by multiple parameters, which have not been investigated in this work such as the order of the shape function. In particular, the use of a second-order shape function may have reduced the errors obtained close to the edges of the region

of interest and improved accuracy of strain results. This is a limitation related to open source software (Ncorr) employed in this study, which adopts a first-order shape function.

- The experimental models of the heart described in this work, although they attempted to replicate *in vivo* human conditions, they did not fully represent the complex behaviour of the cardiac muscle contractions. Nevertheless, the magnitude of the strain quantified in this work was similar to that measured in previous studies.
- Being an optical method, 3D-DIC can perform only surface measurements. Although, as shown in this study, these provided a very detailed map of the strain on the epicardium and differentiate different states of the heart, it could not infer on the transmural myocardial deformation.
- Speckle pattern application of utmost importance to ensure accurate image matching still remains a challenging task to accomplish in *ex vivo* cardiac tissues as the surface of the heart becomes very wet during the operation of the platform, thus, damaging the quality of the applied speckle pattern.

6.3 Future work

Opportunities for future works concern both the technical development of the experimental method and the applications of this to quantify strain in *ex vivo* beating heart in LV working mode.

The implementation of multi-camera system (e.g. Solav et al. (2018)) for panoramic imaging of the heart may increase the region of interest analysed on the heart surface and provide a more comprehensive investigation of the behaviour of the LV contraction and twisting.

The development of real-time system for 3D-DIC (e.g. Wu et al. (2016)), a trend that is growing within the DIC community, may provide rapid visualisation of the deformation on the heart surface when conditions of the heart vary.

The highly dense set of data that DIC can generate may be used to inform mathematical model and be integrated in a finite element model of the heart deformation, providing a complementary analysis and validation to the experimental measurement.

Finally, with recent advance in techniques including digital volume correlation (DVC), which extends the capability of DIC from surface to volumetric full-field measurement, it is possible to characterise internal tissue mechanics. Therefore, although DVC has been employed mainly for applications at a micro-scale requiring particular levels of spatial resolution, accuracy and precision (e.g. Dall'Ara et al. (2014); Acosta Santamaría et al. (2018)), future research in the heart mechanics may benefit from the use of such technique with DVC applications providing reference measurements of cardiac strain to be used for the ongoing clinical validation of US-3D-STE as both techniques allow volumetric reconstruction of tissue structures deformations.

Bibliography

- V. A. Acosta Santamaría, M. Flechas García, J. Molimard, and S. Avril. Three-Dimensional Full-Field Strain Measurements across a Whole Porcine Aorta Subjected to Tensile Loading Using Optical Coherence Tomography–Digital Volume Correlation. *Frontiers in Mechanical Engineering*, 4(March):1–14, 2018. ISSN 2297-3079. doi: 10.3389/fmech.2018.00003.
- B. H. Amundsen, T. Helle-Valle, T. Edvardsen, H. Torp, J. Crosby, E. Lyseggen, A. Støylen, H. Ihlen, J. A. Lima, O. A. Smiseth, and S. A. Slørdahl. Noninvasive Myocardial Strain Measurement by Speckle Tracking Echocardiography. *Journal of the American College of Cardiology*, 47(4):789–793, feb 2006. ISSN 07351097. doi: 10.1016/j.jacc.2005.10.040.
- M. S. Amzulescu, M. De Craene, H. Langet, A. Pasquet, D. Vancraeynest, A. C. Pouleur, J. L. Vanoverschelde, and B. L. Gerber. Myocardial strain imaging: review of general principles, validation, and sources of discrepancies. *European heart journal cardiovascular Imaging*, 20(6):605–619, 2019. ISSN 20472412. doi: 10.1093/ehjci/jez041.
- S. Baker and I. Matthews. Equivalence and efficiency of image alignment algorithms. In *Proceedings of the 2001 IEEE Computer Society Conference on Computer Vision and Pattern Recognition. CVPR 2001*, volume 1, pages I–1090–I–1097. IEEE Comput. Soc, 2005. ISBN 0-7695-1272-0. doi: 10.1109/CVPR.2001.990652.

- R. Balcaen, P. Reu, P. Lava, and D. Debruyne. Stereo-DIC Uncertainty Quantification based on Simulated Images. *Experimental Mechanics*, 2017a. ISSN 0014-4851. doi: 10.1007/s11340-017-0288-9.
- R. Balcaen, L. Wittevrongel, P. L. Reu, P. Lava, and D. Debruyne. Stereo-DIC Calibration and Speckle Image Generator Based on FE Formulations. *Experimental Mechanics*, 57(5):703–718, jun 2017b. ISSN 0014-4851. doi: 10.1007/s11340-017-0259-1.
- T. A. Berfield, J. K. Patel, R. G. Shimmin, P. V. Braun, J. Lambros, and N. R. Sottos. Micro- and Nanoscale Deformation Measurement of Surface and Internal Planes via Digital Image Correlation. pages 51–62, 2007. doi: 10.1007/s11340-006-0531-2.
- R. M. Berne and M. N. Levy. *Cardiovascular physiology*. Mosby, 1967.
- M. R. Bersi, C. Bellini, P. Di Achille, J. D. Humphrey, K. Genovese, and S. Avril. Novel Methodology for Characterizing Regional Variations in the Material Properties of Murine Aortas. *Journal of Biomechanical Engineering*, 138(7):071005, jun 2016. ISSN 0148-0731. doi: 10.1115/1.4033674.
- P. Bing, X. Hui-min, X. Bo-qin, and D. Fu-long. Performance of sub-pixel registration algorithms in digital image correlation. *Measurement Science and Technology*, 17(6):1615–1621, jun 2006. ISSN 0957-0233. doi: 10.1088/0957-0233/17/6/045.
- J. Blaber, B. Adair, and A. Antoniou. Ncorr: Open-Source 2D Digital Image Correlation Matlab Software. *Experimental Mechanics*, 55(6):1105–1122, jul 2015. ISSN 0014-4851. doi: 10.1007/s11340-015-0009-1.
- M. Bornert, F. Brémand, P. Doumalin, J.-C. Dupré, M. Fazzini, M. Grédiac, F. Hild, S. Mistou, J. Molimard, J.-J. Orteu, L. Robert, Y. Surrel, P. Vacher, and B. Watrisse. Assessment of Digital Image Correlation Measurement Errors: Methodol-

- ogy and Results. *Experimental Mechanics*, 49(3):353–370, jun 2009. ISSN 0014-4851. doi: 10.1007/s11340-008-9204-7.
- E. B. Bourgeois, A. D. Bachtel, J. Huang, G. P. Walcott, and J. M. Rogers. Simultaneous optical mapping of transmembrane potential and wall motion in isolated, perfused whole hearts. *Journal of Biomedical Optics*, 16(9):096020, 2011. ISSN 10833668. doi: 10.1117/1.3630115.
- A. Campo, J. Soons, H. Heuten, G. Ennekens, I. Goovaerts, C. Vrints, P. Lava, and J. Dirckx. Digital image correlation for full-field time-resolved assessment of arterial stiffness. *Journal of Biomedical Optics*, 19(1):016008, jan 2014. ISSN 1083-3668. doi: 10.1117/1.JBO.19.1.016008.
- J. F. Cardenas-Garcia, H. G. Yao, and S. Zheng. 3D Reconstruction of Objects Using Stereo Imaging. *Optics and Lasers in Engineering*, 22:193–213, 1995.
- L. Chernak Slane and D. G. Thelen. The use of 2D ultrasound elastography for measuring tendon motion and strain. *Journal of Biomechanics*, 47(3):750–754, feb 2014. ISSN 00219290. doi: 10.1016/j.jbiomech.2013.11.023.
- M. Cikes and S. D. Solomon. Beyond ejection fraction: an integrative approach for assessment of cardiac structure and function in heart failure. *European Heart Journal*, 37(21):1642–1650, jun 2016. ISSN 0195-668X. doi: 10.1093/eurheartj/ehv510.
- D. Cosentino, I. Zwierzak, S. Schievano, V. Díaz-zuccharini, J. W. Fenner, and A. J. Narracott. Uncertainty assessment of imaging techniques for the 3D reconstruction of stent geometry. *Medical Engineering and Physics*, 36(8):1062–1068, 2014. ISSN 1350-4533. doi: 10.1016/j.medengphy.2014.04.008.
- E. Dall’Ara, D. Barber, and M. Viceconti. About the inevitable compromise between spatial resolution and accuracy of strain measurement for bone tissue: A 3D zero-

- strain study. *Journal of Biomechanics*, 47(12):2956–2963, 2014. ISSN 18732380. doi: 10.1016/j.jbiomech.2014.07.019.
- M. Dandel, H. Lehmkuhl, C. Knosalla, N. Suramelashvili, and R. Hetzer. Strain and strain rate imaging by echocardiography - basic concepts and clinical applicability. *Curr Cardiol Rev*, 5(2):133–148, 2009. ISSN 1875-6557. doi: 10.2174/157340309788166642.
- J. de Hart, A. Weger, S. van Tuijl, J. M. A. Stijnen, C. N. van den Broek, M. C. M. Rutten, and B. A. de Mol. An ex vivo platform to simulate cardiac physiology: A new dimension for therapy development and assessment. *International Journal of Artificial Organs*, 34(6):495–505, 2011. ISSN 03913988. doi: 10.5301/IJAO.2011.8456.
- J. D’Hooge, A. Heimdal, F. Jamal, T. Kukulski, B. Bijmens, F. Rademakers, L. Hatle, P. Suetens, and G. R. Sutherland. Regional Strain and Strain Rate Measurements by Cardiac Ultrasound: Principles, Implementation and Limitations. *European Journal of Echocardiography*, 1(3):154–170, 2000. ISSN 15252167. doi: 10.1053/euje.2000.0031.
- Y. Dong and B. Pan. A Review of Speckle Pattern Fabrication and Assessment for Digital Image Correlation. *Experimental Mechanics*, 2017. ISSN 0014-4851. doi: 10.1007/s11340-017-0283-1.
- L. Fassina, G. Rozzi, S. Rossi, S. Scacchi, M. Galetti, F. P. Lo Muzio, F. Del Bianco, P. Colli Franzone, G. Petrilli, G. Faggian, and M. Miragoli. Cardiac kinematic parameters computed from video of in situ beating heart. *Scientific Reports*, 7 (April):46143, 2017. ISSN 2045-2322. doi: 10.1038/srep46143.
- P. Ferraiuoli, J. Taylor, E. Martin, J. Fenner, and A. Narracott. The Accuracy of 3D Optical Reconstruction and Additive Manufacturing Processes in Reproducing

- Detailed Subject-Specific Anatomy. *Journal of Imaging*, 3(4):45, oct 2017. ISSN 2313-433X. doi: 10.3390/jimaging3040045.
- P. Ferraiuoli, L. S. Fixsen, B. Kappler, R. G. Lopata, J. W. Fenner, and A. J. Narracott. Measurement of in vitro cardiac deformation by means of 3D digital image correlation and ultrasound 2D speckle-tracking echocardiography. *Medical Engineering & Physics*, 74:146–152, dec 2019a. ISSN 13504533. doi: 10.1016/j.medengphy.2019.09.021.
- P. Ferraiuoli, B. Kappler, S. van Tuijl, M. Stijnen, B. A. de Mol, J. W. Fenner, and A. J. Narracott. Full-field analysis of epicardial strain in an in vitro porcine heart platform. *Journal of the Mechanical Behavior of Biomedical Materials*, 91 (November 2018):294–300, mar 2019b. ISSN 17516161. doi: 10.1016/j.jmbbm.2018.11.025.
- G. R. Gaudette, I. B. Krukenkamp, E. U. Azeloglu, A. E. Saltman, M. Lense, J. Todaro, and F. P. Chiang. Effects of ischemia on epicardial deformation in the passive rabbit heart. *Journal of Biomechanical Engineering*, 126(1):70–75, 2004. ISSN 01480731. doi: 10.1115/1.1645524.
- K. Genovese, Y. Lee, and J. Humphrey. Novel optical system for in vitro quantification of full surface strain fields in small arteries: I. Theory and design. *Computer Methods in Biomechanics and Biomedical Engineering*, 14(3):213–225, mar 2011a. ISSN 1025-5842. doi: 10.1080/10255842.2010.545823.
- K. Genovese, Y. U. Lee, and J. D. Humphrey. Novel optical system for in vitro quantification of full surface strain fields in small arteries : II . Correction for refraction and illustrative results. *Computer Methods in Biomechanics and Biomedical Engineering*, 14(3):227–237, 2011b. doi: 10.1080/10255842.2010.545823.
- K. Genovese, M. J. Collins, Y. U. Lee, and J. D. Humphrey. Regional Finite Strains in an Angiotensin-II Induced Mouse Model of Dissecting Abdominal Aor-

- tic Aneurysms. *Cardiovascular Engineering and Technology*, 3(2):194–202, jun 2012. ISSN 1869-408X. doi: 10.1007/s13239-012-0083-9.
- K. Genovese, Y.-U. Lee, A. Lee, and J. Humphrey. An improved panoramic digital image correlation method for vascular strain analysis and material characterization. *Journal of the Mechanical Behavior of Biomedical Materials*, 27(164): 132–142, nov 2013. ISSN 17516161. doi: 10.1016/j.jmbbm.2012.11.015.
- K. Genovese, A. Montes, A. Martínez, and S. L. Evans. Full-surface deformation measurement of anisotropic tissues under indentation. *Medical Engineering & Physics*, 37(5):484–493, may 2015. ISSN 13504533. doi: 10.1016/j.medengphy.2015.03.005.
- K. Gijsbertse, A. Sprengers, H. Naghibi Beidokhti, M. Nillesen, C. de Korte, and N. Verdonschot. Strain imaging of the lateral collateral ligament using high frequency and conventional ultrasound imaging: An ex-vivo comparison. *Journal of Biomechanics*, 73:233–237, may 2018. ISSN 00219290. doi: 10.1016/j.jbiomech.2018.03.035.
- O. Gültekin, G. Sommer, and G. A. Holzapfel. An orthotropic viscoelastic model for the passive myocardium: continuum basis and numerical treatment. *Computer Methods in Biomechanics and Biomedical Engineering*, 19(15):1647–1664, 2016. ISSN 14768259. doi: 10.1080/10255842.2016.1176155.
- H. Haddadi and S. Belhabib. Use of rigid-body motion for the investigation and estimation of the measurement errors related to digital image correlation technique. *Optics and Lasers in Engineering*, 46(2):185–196, 2008. ISSN 01438166. doi: 10.1016/j.optlaseng.2007.05.008.
- R. Hartley and A. Zisserman. *Multiple View Geometry in Computer Vision*. Cambridge University Press, Cambridge, second edition, 2004. ISBN 9780511811685. doi: 10.1017/CBO9780511811685.

- J. Heikkila and O. Silven. A four-step camera calibration procedure with implicit image correction. In *Proceedings of IEEE Computer Society Conference on Computer Vision and Pattern Recognition*, pages 1106–1112. IEEE Comput. Soc, 1997. ISBN 0-8186-7822-4. doi: 10.1109/CVPR.1997.609468.
- M. Hokka, N. Mirow, H. Nagel, M. Irsusi, S. Vogt, and V.-t. Kuokkala. In-vivo deformation measurements of the human heart by 3D Digital Image Correlation. *Journal of Biomechanics*, 48(10):2217–2220, 2015. ISSN 0021-9290. doi: 10.1016/j.jbiomech.2015.03.015.
- L. Horny, H. Chlup, R. Zitny, T. Vonavkova, J. Vesely, and P. Lanzer. Ex vivo coronary stent implantation evaluated with digital image correlation. *Experimental Mechanics*, 52:1555–1558, 2012. ISSN 1467-9280. doi: 10.1007/s13398-014-0173-7. 2.
- Z. Hu, H. Xie, J. Lu, H. Wang, and J. Zhu. Error evaluation technique for three-dimensional digital image correlation. *Applied Optics*, 50(33):6239, 2011. ISSN 0003-6935. doi: 10.1364/AO.50.006239.
- J. D. Humphrey. *Cardiovascular Solid Mechanics*. Springer New York, New York, NY, 2002. ISBN 978-1-4419-2897-9. doi: 10.1007/978-0-387-21576-1.
- R. E. Jacobson, F. R. Sidney, G. G. Attridge, and N. R. Axford. *The manual of photography: photographic and digital imaging*. 9th editio edition, 2000. ISBN 0240515749.
- M. F. Jan and A. J. Tajik. Modern Imaging Techniques in Cardiomyopathies. *Circulation Research*, 121(7):874–891, sep 2017. ISSN 0009-7330. doi: 10.1161/CIRCRESAHA.117.309600.
- K. Kalam, P. Otahal, and T. H. Marwick. Prognostic implications of global LV dysfunction: a systematic review and meta-analysis of global longitudinal strain

- and ejection fraction. *Heart*, 100(21):1673–1680, nov 2014. ISSN 1355-6037. doi: 10.1136/heartjnl-2014-305538.
- A. Karimi, M. Navidbakhsh, A. Shojaei, and S. Faghihi. Measurement of the uniaxial mechanical properties of healthy and atherosclerotic human coronary arteries. *Materials Science and Engineering: C*, 33(5):2550–2554, 2013. ISSN 09284931. doi: 10.1016/j.msec.2013.02.016.
- A. Karimi, T. Sera, and S. Kudo. Experimental verification of the healthy and atherosclerotic coronary arteries incompressibility via Digital Image Correlation. *Artery Research*, 16:1–7, 2016. ISSN 1872-9312. doi: <http://dx.doi.org/10.1016/j.artres.2016.08.002>.
- M. Kashfuddoja, R. Prasath, and M. Ramji. Study on experimental characterization of carbon fiber reinforced polymer panel using digital image correlation: A sensitivity analysis. *Optics and Lasers in Engineering*, 62:17–30, nov 2014. ISSN 01438166. doi: 10.1016/j.optlaseng.2014.04.019.
- X.-D. Ke, H. W. Schreier, M. A. Sutton, and Y. Q. Wang. Error Assessment in Stereo-based Deformation Measurements. *Experimental Mechanics*, 51(4):423–441, apr 2011. ISSN 0014-4851. doi: 10.1007/s11340-010-9450-3.
- J.-H. Kim, S. Avril, A. Duprey, and J.-P. Favre. Experimental characterization of rupture in human aortic aneurysms using a full-field measurement technique. *Biomechanics and Modeling in Mechanobiology*, 11(6):841–853, 2012. ISSN 1617-7959. doi: 10.1007/s10237-011-0356-5.
- T. K. Koo and M. Y. Li. A Guideline of Selecting and Reporting Intraclass Correlation Coefficients for Reliability Research. *Journal of Chiropractic Medicine*, 15(2):155–163, jun 2016. ISSN 15563707. doi: 10.1016/j.jcm.2016.02.012.
- J. I. Laughner, S. Zhang, H. Li, C. C. Shao, and I. R. Efimov. Mapping cardiac surface mechanics with structured light imaging. *AJP: Heart and Circulatory*

- Physiology*, 303(6):H712–H720, sep 2012. ISSN 0363-6135. doi: 10.1152/ajpheart.00269.2012.
- P. Lava, S. Cooreman, S. Coppieters, M. De Strycker, and D. Debruyne. Assessment of measuring errors in DIC using deformation fields generated by plastic FEA. *Optics and Lasers in Engineering*, 47(7-8):747–753, jul 2009. ISSN 01438166. doi: 10.1016/j.optlaseng.2009.03.007.
- D. Lecompte, A. Smits, S. Bossuyt, H. Sol, J. Vantomme, D. Van Hemelrijck, and A. M. Habraken. Quality assessment of speckle patterns for digital image correlation. *Optics and Lasers in Engineering*, 44(11):1132–1145, 2006. ISSN 01438166. doi: 10.1016/j.optlaseng.2005.10.004.
- A. Leopaldi, R. Vismara, S. van Tuijl, A. Redaelli, F. van de Vosse, G. Fiore, and M. Rutten. A novel passive left heart platform for device testing and research. *Medical Engineering & Physics*, 37(4):361–366, apr 2015. ISSN 13504533. doi: 10.1016/j.medengphy.2015.01.013.
- A. M. Leopaldi, K. Wrobel, G. Speziali, S. van Tuijl, A. Drasutiene, and W. R. Chitwood. The dynamic cardiac biosimulator: A method for training physicians in beating-heart mitral valve repair procedures. *The Journal of Thoracic and Cardiovascular Surgery*, 155(1):147–155, jan 2018. ISSN 00225223. doi: 10.1016/j.jtcvs.2017.09.011.
- G. Lionello, C. Sirieix, and M. Baleani. An effective procedure to create a speckle pattern on biological soft tissue for digital image correlation measurements. *Journal of the Mechanical Behavior of Biomedical Materials*, 39:1–8, nov 2014. ISSN 17516161. doi: 10.1016/j.jmbbm.2014.07.007.
- R. G. Lopata, H. H. Hansen, M. M. Nillesen, J. M. Thijssen, and C. L. De Korte. Comparison of One-Dimensional and Two-Dimensional Least-Squares Strain Es-

- timators for Phased Array Displacement Data. *Ultrasonic Imaging*, 31(1):1–16, jan 2009a. ISSN 0161-7346. doi: 10.1177/016173460903100105.
- R. G. Lopata, M. M. Nillesen, H. H. Hansen, I. H. Gerrits, J. M. Thijssen, and C. L. de Korte. Performance Evaluation of Methods for Two-Dimensional Displacement and Strain Estimation Using Ultrasound Radio Frequency Data. *Ultrasound in Medicine & Biology*, 35(5):796–812, may 2009b. ISSN 03015629. doi: 10.1016/j.ultrasmedbio.2008.11.002.
- H. Lu and P. D. Cary. Deformation measurements by digital image correlation: Implementation of a second-order displacement gradient. *Experimental Mechanics*, 40(4):393–400, dec 2000. ISSN 0014-4851. doi: 10.1007/BF02326485.
- P. F. Luo, Y. J. Chao, M. A. Sutton, and W. H. Peters. Accurate measurement of three-dimensional deformations in deformable and rigid bodies using computer vision. *Experimental Mechanics*, 33(2):123–132, jun 1993. ISSN 0014-4851. doi: 10.1007/BF02322488.
- T. Luyckx, M. Verstraete, K. De Roo, W. De Waele, J. Bellemans, and J. Victor. Digital image correlation as a tool for three-dimensional strain analysis in human tendon tissue. *Journal of Experimental Orthopaedics*, 1(1):7, 2014. ISSN 2197-1153. doi: 10.1186/s40634-014-0007-8.
- Matlab. Point Grey Camera Support from Image Acquisition Toolbox (<http://uk.mathworks.com/hardware-support/point-grey-camera.html>).
- W. Mawad and L. L. Mertens. Recent Advances and Trends in Pediatric Cardiac Imaging. *Current Treatment Options in Cardiovascular Medicine*, 20(1):9, jan 2018. ISSN 1092-8464. doi: 10.1007/s11936-018-0599-x.
- A. D. McCulloch, B. H. Smaill, and P. J. Hunter. Left ventricular epicardial deformation in isolated arrested dog heart. *American Journal of Physiology-Heart*

-
- and Circulatory Physiology*, 252(1):H233–H241, jan 1987. ISSN 0363-6135. doi: 10.1152/ajpheart.1987.252.1.H233.
- A. D. McCulloch, B. H. Smaill, and P. J. Hunter. Regional left ventricular epicardial deformation in the passive dog heart. *Circulation Research*, 64(4):721–733, apr 1989. ISSN 0009-7330. doi: 10.1161/01.RES.64.4.721.
- V. Mor-Avi, R. M. Lang, L. P. Badano, M. Belohlavek, N. M. Cardim, G. Derumeaux, M. Galderisi, T. Marwick, S. F. Nagueh, P. P. Sengupta, R. Sicari, O. A. Smiseth, B. Smulevitz, M. Takeuchi, J. D. Thomas, M. Vannan, J.-U. Voigt, and J. L. Zamorano. Current and Evolving Echocardiographic Techniques for the Quantitative Evaluation of Cardiac Mechanics: ASE/EAE Consensus Statement on Methodology and Indications Endorsed by the Japanese Society of Echocardiography. *European Journal of Echocardiography*, 12(3):167–205, mar 2011. ISSN 1525-2167. doi: 10.1093/ejechocard/jer021.
- D. Mozaffarian, E. J. Benjamin, A. S. Go, D. K. Arnett, M. J. Blaha, M. Cushman, S. R. Das, S. de Ferranti, J.-P. Després, H. J. Fullerton, V. J. Howard, M. D. Huffman, C. R. Isasi, M. C. Jiménez, S. E. Judd, B. M. Kissela, J. H. Lichtman, L. D. Lisabeth, S. Liu, R. H. Mackey, D. J. Magid, D. K. McGuire, E. R. Mohler, C. S. Moy, P. Muntner, M. E. Mussolino, K. Nasir, R. W. Neumar, G. Nichol, L. Palaniappan, D. K. Pandey, M. J. Reeves, C. J. Rodriguez, W. Rosamond, P. D. Sorlie, J. Stein, A. Towfighi, T. N. Turan, S. S. Virani, D. Woo, R. W. Yeh, and M. B. Turner. Heart Disease and Stroke Statistics—2016 Update. *Circulation*, 133(4):e38–e360, jan 2016. ISSN 0009-7322. doi: 10.1161/CIR.0000000000000350.
- Y. Nagata, V. C. C. Wu, Y. Otsuji, and M. Takeuchi. Normal range of myocardial layer-specific strain using two-dimensional speckle tracking echocardiography. *PLoS ONE*, 12(6):1–16, 2017. ISSN 19326203. doi: 10.1371/journal.pone.0180584.
- G. C. Nesbitt, S. Mankad, and J. K. Oh. Strain imaging in echocardiography:

- methods and clinical applications. *The International Journal of Cardiovascular Imaging*, 25(S1):9–22, apr 2009. ISSN 1569-5794. doi: 10.1007/s10554-008-9414-1.
- A. M. S. Omar, S. Vallabhajosyula, and P. P. Sengupta. Left Ventricular Twist and Torsion. *Circulation: Cardiovascular Imaging*, 8(6):74–82, jun 2015. ISSN 1941-9651. doi: 10.1161/CIRCIMAGING.115.003029.
- J.-J. Orteu. 3-D computer vision in experimental mechanics. *Optics and Lasers in Engineering*, 47:282–291, 2009. doi: 10.1016/j.optlaseng.2007.11.009.
- N. Otsu. A Threshold Selection Method from Gray-Level Histograms. *IEEE Transactions on Systems, Man, and Cybernetics*, 9(1):62–66, jan 1979. ISSN 0018-9472. doi: 10.1109/TSMC.1979.4310076.
- M. Palanca, G. Tozzi, and L. Cristofolini. The use of digital image correlation in the biomechanical area: a review. *International Biomechanics*, 3(1):1–21, jan 2016. ISSN 2333-5432. doi: 10.1080/23335432.2015.1117395.
- M. Palanca, M. Marco, M. L. Ruspi, and L. Cristofolini. Full-field strain distribution in multi-vertebra spine segments: An in vitro application of digital image correlation. *Medical Engineering & Physics*, 52:76–83, feb 2018. ISSN 13504533. doi: 10.1016/j.medengphy.2017.11.003.
- B. Pan. Reliability-guided digital image correlation for image deformation measurement. *Applied Optics*, 48(8):1535, mar 2009. ISSN 0003-6935. doi: 10.1364/AO.48.001535.
- B. Pan. Digital image correlation for surface deformation measurement: historical developments, recent advances and future goals. *Measurement Science and Technology*, 29(8):082001, aug 2018. ISSN 0957-0233. doi: 10.1088/1361-6501/aac55b.
- B. Pan and B. Wang. Digital Image Correlation with Enhanced Accuracy and Efficiency: A Comparison of Two Subpixel Registration Algorithms. *Exper-*

-
- imental Mechanics*, 56(8):1395–1409, 2016. ISSN 17412765. doi: 10.1007/s11340-016-0180-z.
- B. Pan, A. Asundi, H. Xie, and J. Gao. Digital image correlation using iterative least squares and pointwise least squares for displacement field and strain field measurements. *Optics and Lasers in Engineering*, 47(7-8):865–874, jul 2009a. ISSN 01438166. doi: 10.1016/j.optlaseng.2008.10.014.
- B. Pan, K. Qian, H. Xie, and A. Asundi. Two-dimensional digital image correlation for in-plane displacement and strain measurement: a review. *Measurement Science and Technology*, 20(6):062001, jun 2009b. ISSN 0957-0233. doi: 10.1088/0957-0233/20/6/062001.
- B. Pan, H. Xie, L. Yang, and Z. Wang. Accurate measurement of satellite antenna surface using 3D digital image correlation technique. *Strain*, 45(2):194–200, 2009c. ISSN 00392103. doi: 10.1111/j.1475-1305.2008.00450.x.
- B. Pan, H. Xie, and Z. Wang. Equivalence of digital image correlation criteria for pattern matching. *Applied Optics*, 49(28):5501, oct 2010. ISSN 0003-6935. doi: 10.1364/AO.49.005501.
- B. Pan, K. Li, and W. Tong. Fast, Robust and Accurate Digital Image Correlation Calculation Without Redundant Computations. *Experimental Mechanics*, 53(7):1277–1289, sep 2013. ISSN 0014-4851. doi: 10.1007/s11340-013-9717-6.
- B. Pan, L. Yu, and Q. Zhang. Review of single-camera stereo-digital image correlation techniques for full-field 3D shape and deformation measurement. *Science China Technological Sciences*, 2017. ISSN 1674-7321. doi: 10.1007/s11431-017-9090-x.
- G. Pedrizzetti, S. Sengupta, G. Caracciolo, C. S. Park, M. Amaki, G. Goliash, J. Narula, and P. P. Sengupta. Three-dimensional principal strain analysis

- for characterizing subclinical changes in left ventricular function. *Journal of the American Society of Echocardiography*, 27(10):1041–1050.e1, 2014. ISSN 10976795. doi: 10.1016/j.echo.2014.05.014.
- W. H. Peters and W. F. Ranson. Digital Imaging Techniques In Experimental Stress Analysis. *Optical Engineering*, 21(3), jun 1982. ISSN 0091-3286. doi: 10.1117/12.7972925.
- N. J. Petterson, L. S. Fixsen, M. C. M. Rutten, N. H. J. Pijls, F. N. van de Vosse, and R. G. P. Lopata. Ultrasound functional imaging in an ex vivo beating porcine heart platform. *Physics in Medicine & Biology*, 62(23):9112–9126, nov 2017. ISSN 1361-6560. doi: 10.1088/1361-6560/aa9515.
- P. Ponikowski, A. A. Voors, S. D. Anker, H. Bueno, J. G. F. Cleland, A. J. S. Coats, V. Falk, J. R. González-Juanatey, V.-p. Harjola, E. A. Jankowska, M. Jessup, C. Linde, P. Nihoyannopoulos, J. T. Parissis, B. Pieske, J. P. Riley, G. M. C. Rosano, L. M. Ruilope, F. Ruschitzka, F. H. Rutten, and P. van der Meer. 2016 ESC Guidelines for the diagnosis and treatment of acute and chronic heart failure. *European Heart Journal*, 37(27):2129–2200, jul 2016. ISSN 0195-668X. doi: 10.1093/eurheartj/ehw128.
- T. T. Prinzen, T. Arts, F. W. Prinzen, and R. S. Reneman. Mapping of epicardial deformation using a video processing technique. *Journal of Biomechanics*, 19(4): 263–273, jan 1986. ISSN 00219290. doi: 10.1016/0021-9290(86)90001-1.
- P. K. Rastogi, editor. *Photomechanics*, volume 77 of *Topics in Applied Physics*. Springer Berlin Heidelberg, Berlin, Heidelberg, 1 edition, 2000. ISBN 978-3-540-65990-7. doi: 10.1007/3-540-48800-6.
- L. Robert, F. Nazaret, T. Cutard, and J.-J. Orteu. Use of 3-D Digital Image Correlation to Characterize the Mechanical Behavior of a Fiber Reinforced Refractory

-
- Castable. *Experimental Mechanics*, 47(6):761–773, dec 2007. ISSN 0014-4851. doi: 10.1007/s11340-007-9062-8.
- D. M. Rubin. A Simple Autocorrelation Algorithm for Determining Grain Size from Digital Images of Sediment. *Journal of Sedimentary Research*, 74(1):160–165, 2004. ISSN 1527-1404. doi: 10.1306/052203740160.
- K. Seo, M. Inagaki, S. Nishimura, I. Hidaka, M. Sugimachi, T. Hisada, and S. Sugiyura. Structural heterogeneity in the ventricular wall plays a significant role in the initiation of stretch-induced arrhythmias in perfused rabbit right ventricular tissues and whole heart preparations. *Circulation Research*, 106(1):176–184, 2010. ISSN 00097330. doi: 10.1161/CIRCRESAHA.109.203828.
- O. A. Smiseth, H. Torp, A. Opdahl, K. H. Haugaa, and S. Urheim. Myocardial strain imaging: how useful is it in clinical decision making? *European heart journal*, 37(15):1196–207, 2015. ISSN 1522-9645. doi: 10.1093/eurheartj/ehv529.
- B. W. Smith, M. Li, and W. Tong. Error Assessment for strain mapping by digital image correlation. *Experimental Techniques*, 22(4):19–21, jul 1998. ISSN 0732-8818. doi: 10.1111/j.1747-1567.1998.tb02332.x.
- D. Solav, K. M. Moerman, A. M. Jaeger, K. Genovese, and H. M. Herr. MultiDIC: An Open-Source Toolbox for Multi-View 3D Digital Image Correlation. *IEEE Access*, 6:30520–30535, 2018. ISSN 2169-3536. doi: 10.1109/ACCESS.2018.2843725.
- A. Soltani, J. Lahti, K. Järvelä, S. Curtze, J. Laurikka, M. Hokka, and V.-T. Kuokkala. An Optical Method for the In-Vivo Characterization of the Biomechanical Response of the Right Ventricle. *Scientific Reports*, 8(1):6831, dec 2018. ISSN 2045-2322. doi: 10.1038/s41598-018-25223-z.
- M. Sutton, X. Ke, S. Lessner, M. Goldbach, M. Yost, F. Zhao, and H. Schreier. Strain field measurements on mouse carotid arteries using microscopic three-dimensional

- digital image correlation. *Journal of Biomedical Materials Research Part A*, 84A(1):178–190, jan 2008a. ISSN 15493296. doi: 10.1002/jbm.a.31268.
- M. A. Sutton, J. H. Yan, V. Tiwari, H. W. Schreier, and J. J. Orteu. The effect of out-of-plane motion on 2D and 3D digital image correlation measurements. *Optics and Lasers in Engineering*, 46(10):746–757, 2008b. ISSN 01438166. doi: 10.1016/j.optlaseng.2008.05.005.
- M. A. Sutton, J.-J. Orteu, and H. Schreier. *Image Correlation for Shape, Motion and Deformation Measurements*. Springer US, Boston, MA, 2009. ISBN 978-0-387-78746-6.
- M. Tee, J. A. Noble, and D. A. Bluemke. Imaging techniques for cardiac strain and deformation: Comparison of echocardiography, cardiac magnetic resonance and cardiac computed tomography. *Expert Review of Cardiovascular Therapy*, 11(2):221–231, 2013. ISSN 14779072. doi: 10.1586/erc.12.182.
- L. F. Tops, V. Delgado, N. A. Marsan, and J. J. Bax. Myocardial strain to detect subtle left ventricular systolic dysfunction. *European Journal of Heart Failure*, 19(3):307–313, mar 2017. ISSN 13889842. doi: 10.1002/ejhf.694.
- J.-U. Voigt, G. Pedrizzetti, P. Lysyansky, T. H. Marwick, H. Houle, R. Baumann, S. Pedri, Y. Ito, Y. Abe, S. Metz, J. H. Song, J. Hamilton, P. P. Sengupta, T. J. Kolias, J. D’Hooge, G. P. Aurigemma, J. D. Thomas, and L. P. Badano. Definitions for a common standard for 2D speckle tracking echocardiography: consensus document of the EACVI/ASE/Industry Task Force to standardize deformation imaging. *European Heart Journal - Cardiovascular Imaging*, 16(1):1–11, jan 2015. ISSN 2047-2404. doi: 10.1093/ehjci/jeu184.
- Y. Wang, P. Lava, S. Coppieters, M. De Strycker, P. Van Houtte, and D. Debruyne. Investigation of the uncertainty of DIC under heterogeneous strain states with

- numerical tests. *Strain*, 48(6):453–462, 2012. ISSN 00392103. doi: 10.1111/j.1475-1305.2012.00840.x.
- Y.-Q. Wang, M. A. Sutton, X.-D. Ke, H. W. Schreier, P. L. Reu, and T. J. Miller. On Error Assessment in Stereo-based Deformation Measurements. *Experimental Mechanics*, 51(4):405–422, apr 2011. ISSN 0014-4851. doi: 10.1007/s11340-010-9449-9.
- Z. Wang, H. Kieu, H. Nguyen, and M. Le. Digital image correlation in experimental mechanics and image registration in computer vision: Similarities, differences and complements. *Optics and Lasers in Engineering*, 65:18–27, feb 2015. ISSN 01438166. doi: 10.1016/j.optlaseng.2014.04.002.
- E. Wilkins, L. Wilson, K. Wickramasinghe, P. Bhatnagar, J. Leal, R. Luengo-Fernandez, R. Burns, M. Rayner, and N. Townsend. *European cardiovascular disease statistics 2017*. European Heart Network, Brussels, 2017.
- R. Wu, H. Wu, D. Arola, and D. Zhang. Real-time three-dimensional digital image correlation for biomedical applications. *Journal of Biomedical Optics*, 21(10):107003, 2016. ISSN 1083-3668. doi: 10.1117/1.JBO.21.10.107003.
- S. Yaofeng and J. H. Pang. Study of optimal subset size in digital image correlation of speckle pattern images. *Optics and Lasers in Engineering*, 45(9):967–974, sep 2007. ISSN 01438166. doi: 10.1016/j.optlaseng.2007.01.012.
- D. Zhang and D. D. Arola. Applications of digital image correlation to biological tissues. *Journal of Biomedical Optics*, 9(4):691–699, 2004. doi: 10.1117/1.1753270.
- D. Zhang, C. D. Eggleton, and D. D. Arola. Evaluating the Mechanical Behavior of Arterial Tissue using Digital Image Correlation. *Experimental Mechanics*, 42(4):409–416, 2002.

- H. Zhang, K. Iijima, J. Huang, G. P. Walcott, and J. M. Rogers. Optical Mapping of Membrane Potential and Epicardial Deformation in Beating Hearts. *Biophysical Journal*, 111(2):438–451, jul 2016. ISSN 00063495. doi: 10.1016/j.bpj.2016.03.043.
- Z. Zhang. A flexible new technique for camera calibration. *IEEE Transactions on Pattern Analysis and Machine Intelligence*, 22(11):1330–1334, 2000. ISSN 01628828. doi: 10.1109/34.888718.
- S. Zhao, L. Gu, and S. R. Froemming. Experimental investigation of the stent–artery interaction. *Journal of Medical Engineering & Technology*, 37(7):463–469, oct 2013. ISSN 0309-1902. doi: 10.3109/03091902.2013.831491.
- F. Q. Zhong, X. X. Shao, and C. Quan. A comparative study of 3D reconstruction methods in stereo digital image correlation. *Optics and Lasers in Engineering*, 122(March):142–150, 2019. ISSN 01438166. doi: 10.1016/j.optlaseng.2019.06.001.
- I. Zwierzak. *In Vitro Characterisation of Stent Deployment and Local Arterial Strain*. Phd thesis, The University of Sheffield, Sheffield, UK, 2014.
- I. Zwierzak, D. Cosentino, A. J. Narracott, P. Bonhoeffer, V. Diaz, J. W. Fenner, and S. Schievano. Measurement of in vitro and in vivo stent geometry and deformation by means of 3D imaging and stereo-photogrammetry. *The International Journal of Artificial Organs*, 37(12):918–927, 2014. ISSN 0391-3988. doi: 10.5301/ijao.5000362.